

Direct measurement of the in-medium η' mass
spectrum in a $\gamma+C$ reaction
($\gamma+C$ 反応を用いた核媒質中での η' 質量スペクトル
の直接測定)

Yuji Matsumura
Department of Physics, Tohoku University

2020

Abstract

The hadron mass is considered to be generated by the spontaneous breaking of chiral symmetry in quantum chromodynamics (QCD) vacuum. The chiral symmetry is expected to be restored under the condition such as high temperatures or high densities. Therefore, possible modification of hadron properties under the condition has been explored both theoretically and experimentally. A nucleus has often been used as a laboratory for the high-density environment. Thus, some experiments have been carried out to measure the mass or decay width of hadrons, especially for mesons, in a nucleus. However, the results are controversial. Therefore, more experimental data are mandatory to obtain reliable information about the meson properties in a nucleus.

The property of the η' meson, which is one of the ground states of pseudoscalar mesons in flavor SU(3), in a nucleus is a crucial research subject that has attracted a great deal of attention to date. The η' meson has larger mass than other pseudoscalar mesons due to the axial U(1) anomaly effect. The anomaly effect is expected to have close relation with the degree of chiral symmetry. Thus, various theoretical models have predicted significant decreasing of η' mass in nuclear medium due to partial restoration of chiral symmetry in a nucleus.

In this thesis, the mass spectrum of η' mesons in nuclear medium is studied in a γ +C reaction via the $\eta' \rightarrow \gamma\gamma$ decay mode with an electro-magnetic calorimeter. This is the first direct measurement of the in-medium η' mass spectrum.

The experiment was carried out at the SPring-8/LEPS2 beamline. Hadrons, including η' mesons, are produced in a γ +C reaction with incident photon beam energies up to 2.4 GeV. Decay products, mainly photons, from photoproduced hadrons are detected by an electro-magnetic calorimeter (BGOegg). BGOegg consists of 1320 BGO crystals covering polar angles from 24 to 144 degrees and the whole azimuthal angles. Neutral or charged particles are distinguished by using inner scintillator hodoscopes installed inside BGOegg.

Mesons decaying into photons are identified in the invariant mass spectrum reconstructed from energies and hit positions at BGOegg. The energy calibration process was carried out using π^0 mass information in the $\gamma\gamma$ invariant mass distribution. Finally, the η' mass resolution is achieved to be 20.7 MeV/c² in the $\gamma\gamma$ invariant mass spectrum, and the independence of the reconstructed mass on the total energies and the emission angles of produced mesons was confirmed.

The deviation of the $\gamma\gamma$ invariant mass distribution from the quasi-free η' mass spectrum was investigated by fitting realistic spectral functions to the measured spectra. The spectra are assumed to consist of the following three sources; the quasi-free η' peak, the background originated by ω mesons, and the multi-meson background. The quasi-free η' peak is represented by a Gaussian function with a fixed width based on the experimental mass resolution. The background distribution from ω mesons was obtained by a realistic Monte Carlo (MC) simulation. The multi-meson production, such as $\pi^0\pi^0$ and $\pi^0\eta$, is a major background for the measurement. Their relative contribution was determined by fitting the simulated spectra of these processes to the real data. It has been confirmed that a simple and smooth function with a few parameters well describes the multi-meson background spectrum around the η' mass.

The event sample was divided into two ranges of $\gamma\gamma$ momenta below and above 1 GeV/c. The high-momentum sample is used as a reference without in-medium signals because most of η' mesons are expected to decay outside a carbon nucleus due to a long decay length. η' photoproduction events from a proton target, which were collected in a different experimental period, were also analyzed as another reference. An enhancement in the low-mass region of the η' mass was obtained with the statistical significance of over 3σ in the low-momentum sample ($P_{\eta'} \leq 1$ GeV/c) of the carbon target data.

The significance of the enhancement was also evaluated by comparing the χ^2 values of fits with and without modeled in-medium signal functions. The signal distribution of the in-medium η' decay was generated by a MC simulation, where two parameters corresponding to mass reduction and width broadening in nuclear media were introduced. The significance of signals was scanned in the two-parameter space of in-medium mass and width modification. Relatively higher significance was observed for the low-momentum sample of the carbon target, while there was no significance appeared for the high-momentum sample in the carbon target data and the overall-momentum sample in the proton target data. The maximum significance reaches 3.7σ for the parameter corresponding to the mass reduction of $\Delta m = 57$ MeV/c². The favored region of mass reduction was determined as an area within 1σ from the maximum value of significance. On the other hand, there was no significant difference among width parameters of $\Delta\Gamma < 100$ MeV. The result indicates the possible modification of η' mass spectrum in the nuclear medium.

Contents

1	Introduction	1
1.1	Light pseudoscalar mesons	1
1.2	Chiral symmetry and meson masses	3
1.2.1	$SU(3)_L \times SU(3)_R$ chiral symmetry	3
1.2.2	Spontaneous breaking of chiral symmetry	4
1.2.3	Restoration of chiral symmetry in nuclear medium	5
1.2.4	η' meson and the axial U(1) anomaly	6
1.3	Theoretical models on the η' mass in nuclei	7
1.3.1	NJL model	7
1.3.2	Linear sigma model	7
1.3.3	QMC model	8
1.4	Experimental studies on the η' mass in nuclei	9
1.5	Direct measurment of in-medium meson mass spectra	10
2	Experiment	15
2.1	SPring-8/LEPS2 facility	15
2.1.1	LEPS2 beamline	15
2.1.2	Backward Compton scattering	17
2.1.3	Tagging counter	19
2.1.4	Target	20
2.2	Detectors	20
2.2.1	BGOegg calorimeter	21
2.2.2	Inner plastic scintillator hodoscopes	23

2.2.3	UpVeto counter	23
2.3	Trigger logic	24
2.4	Data collection	25
3	Calibration	27
3.1	Fundamental calibration for BGOegg	27
3.1.1	Energy reconstruction and clustering	27
3.1.2	Energy leakage of a cluster	29
3.1.3	Energy calibration of BGOegg	30
3.1.4	Timing calibration of BGOegg	34
3.2	Additional correction of cluster energy	35
3.2.1	Problems of obtained gain factors	35
3.2.2	Correction of cluster energy for the forward layers	41
4	Event selection for η' analysis	49
4.1	Fundamental event selection	49
4.2	Background reduction criteria	53
4.2.1	Cluster radius	53
4.2.2	Cluster shape	58
4.3	Final $\eta' \rightarrow \gamma\gamma$ spectrum	59
5	Line shape analysis	63
5.1	Outline of the line shape analysis	63
5.2	Simulation for background events	64
5.2.1	Energy-dependent beam shape	65
5.2.2	Mass resolution	65
5.3	Mass spectra of background processes	67
5.3.1	Quasi-free η' peak	67
5.3.2	Background from ω mesons	68
5.3.3	Multi-meson background	68
5.3.4	Unphysical background	75
5.4	Fit to the $\gamma\gamma$ invariant mass spectrum	80
5.4.1	Momentum cut of the samples for the line shape analysis . . .	83
5.4.2	Fit results of the $\gamma\gamma$ invariant mass spectra	84

5.4.3	Examination of systematic uncertainties	88
6	Discussions	95
6.1	χ^2 difference test for the $\gamma\gamma$ spectra	95
6.1.1	Simulation of in-medium η' decay signals	96
6.1.2	Fit results including in-medium modification signals	108
6.2	Systematic studies	113
6.2.1	Analysis for the proton target data	113
6.2.2	χ^2 difference test with another signal function	113
6.2.3	Other systematic studies	117
6.3	Further discussions	117
7	Conclusions	129
A	Examination of $\gamma\gamma$ spectra in other conditions	133
B	Mass resolution of π^0 and η	141

Chapter 1

Introduction

The hadron mass is considered to be generated by the spontaneous breaking of chiral symmetry in quantum chromodynamics (QCD) vacuum. Recently possible modification of hadron properties due to restoration of chiral symmetry at high temperatures or finite densities has been discussed actively. The η' meson, which is one of the ground states of pseudoscalar mesons in flavour SU(3), in nuclear medium have been a crucial research subject that has attracted a great deal of attention because of its unique properties. In this chapter, an introduction of light pseudoscalar mesons and chiral symmetry, fundamental properties of the η' meson, and examples of theoretical and experimental studies of the η' meson in nuclear medium are described.

1.1 Light pseudoscalar mesons

In the constituent quark model, mesons are composed of a quark and anti-quark pair $q\bar{q}$. It is known that the strong interaction has approximate symmetry under rotation of the triplet of the lightest three quarks (u, d, s), called the flavour SU(3) symmetry. Then the $q\bar{q}$ state can be grouped by the SU(3) multiplet representations. The nine $q\bar{q}$ states can be decomposed into the SU(3) irreducible representations:

$$\mathbf{3} \otimes \bar{\mathbf{3}} = \mathbf{1} \oplus \mathbf{8} \tag{1.1}$$

The singlet state is written by

$$|\text{singlet}\rangle = \frac{1}{\sqrt{3}}(|u\bar{u}\rangle + |d\bar{d}\rangle + |s\bar{s}\rangle), \quad (1.2)$$

and the octet states are generated by eight independent bases. The ground states of mesons are characterized by their quantum numbers; I_3 , the z component of isospin I , and the hypercharge Y . Figure 1.1 shows the ground states of mesons. Their spin-parity is $J^P = 0^-$. The three states π^0 , η_8 , and η_0 are at the origin of the I_3 - Y plane. The π^0 meson is the isovector ($I = 1$) state written as

$$|\pi^0\rangle = \frac{1}{\sqrt{2}}(|u\bar{u}\rangle - |d\bar{d}\rangle). \quad (1.3)$$

The isoscalar ($I = 0$) states η_8 and η_0 belong to the octet and singlet representation of the flavour SU(3), respectively. Their quark components are written as follows:

$$|\eta_8\rangle = \frac{1}{\sqrt{6}}(|u\bar{u}\rangle + |d\bar{d}\rangle - 2|s\bar{s}\rangle), \quad (1.4)$$

$$|\eta_0\rangle = \frac{1}{\sqrt{3}}(|u\bar{u}\rangle + |d\bar{d}\rangle + |s\bar{s}\rangle). \quad (1.5)$$

The isoscalar components $|\eta_8\rangle$ and $|\eta_0\rangle$ are mixing to form the mass eigenstates $|\eta\rangle$ and $|\eta'\rangle$:

$$|\eta\rangle = \cos\theta|\eta_8\rangle - \sin\theta|\eta_0\rangle, \quad (1.6)$$

$$|\eta'\rangle = \sin\theta|\eta_0\rangle + \cos\theta|\eta_8\rangle, \quad (1.7)$$

where θ is the mixing angle of η_8 and η_0 . The empirical value of θ is in the range -11.5° – -24.6° [1–3]. Since θ is relatively small, we can assume that $|\eta\rangle \approx |\eta_8\rangle$ and $|\eta'\rangle \approx |\eta_0\rangle$. The masses of η and η' mesons are $547.9 \text{ MeV}/c^2$ and $957.8 \text{ MeV}/c^2$, respectively [1].

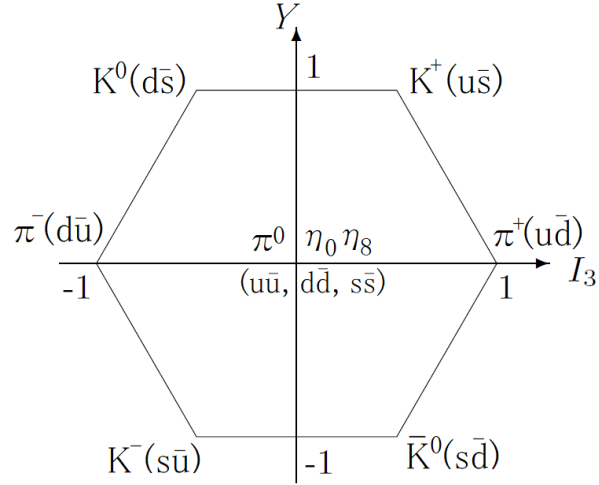


Figure 1.1: The light pseudoscalar mesons composed of u , d , s quarks.

1.2 Chiral symmetry and meson masses

1.2.1 $SU(3)_L \times SU(3)_R$ chiral symmetry

The quantum chromodynamics(QCD) Lagrangian density for three flavours (u , d , s) is written as

$$\mathcal{L}_{\text{QCD}} = \bar{\psi} (i\gamma^\mu D_\mu - M) \psi - \frac{1}{4} G_{\mu\nu}^a G^{a\mu\nu}, \quad (1.8)$$

where ψ , γ^μ , M , and $G_{\mu\nu}^a$ are the quark field, gamma matrices, quark mass matrices, and the strengths of the gluon field, respectively. The quark field ψ can be divided into the left-handed (ψ_L) and the right-handed (ψ_R) fields as follows:

$$\psi = \left(\frac{1 - \gamma_5}{2} + \frac{1 + \gamma_5}{2} \right) \psi = \psi_L + \psi_R. \quad (1.9)$$

The chiral transformation is defined as an independent rotation for the left and right-handed quark fields. That is, the $SU(3)_L \times SU(3)_R$ chiral transformation is defined by

$$\psi_L \mapsto \exp(i\theta_L^a T^a) \psi_L, \quad (1.10)$$

$$\psi_R \mapsto \exp(i\theta_R^a T^a) \psi_R, \quad (1.11)$$

where T^a ($a=1,2,\dots,8$) are the generators of the special unitary group $SU(3)$. The QCD Lagrangian (1.8) has symmetry under the $SU(3)_L \times SU(3)_R$ chiral transformation in the massless limit, $M \rightarrow 0$. Since the current quark masses are small compared with the QCD energy scale, we can assume approximate chiral symmetry for the QCD Lagrangian.

1.2.2 Spontaneous breaking of chiral symmetry

Using the equation (1.9), the chiral transformation (1.10) and (1.11) can be rewritten as the transformation for the quark field ψ :

$$\psi \mapsto \exp(i\theta_V^a T^a) \psi, \quad (1.12)$$

$$\psi \mapsto \exp(i\theta_A^a \gamma_5 T^a) \psi. \quad (1.13)$$

The transformation (1.12) and (1.13) are called the vector and axial-vector transformation, respectively. In the chiral limit ($M \rightarrow 0$), the QCD Lagrangian (1.8) is invariant under the vector and axial-vector transformation, individually. From the Noether theorem, these transformations lead to conserved currents, $j_V^{a\mu}$ and $j_A^{a\mu}$, and conserved charges, Q_V^a and Q_A^a :

$$j_V^{a\mu} = \bar{\psi} \gamma^\mu T^a \psi, \quad (1.14)$$

$$j_A^{a\mu} = \bar{\psi} \gamma^\mu \gamma_5 T^a \psi, \quad (1.15)$$

$$Q_V^a = \int d^3x j_V^{a0}, \quad (1.16)$$

$$Q_A^a = \int d^3x j_A^{a0}. \quad (1.17)$$

The operators Q_V^a and Q_A^a are also the generators of the vector and axial-vector

transformation, respectively.

Although the QCD Lagrangian is invariant under the axial-vector transformation, the ground state of the QCD, the QCD vacuum $|0\rangle$, breaks the symmetry [4]:

$$Q_A^a|0\rangle \neq 0. \quad (1.18)$$

In this case, the symmetry is called to be spontaneously broken. From the Nambu-Goldstone theorem, massless particles called Nambu-Goldstone (NG) bosons appear when a global symmetry is spontaneously broken [5]. Thus, eight pseudoscalar NG bosons should exist corresponding to the generators of $SU(3)_A$ axial-vector transformation, Q_A^a ($a=1,2,\dots,8$). These NG bosons are physically identified with the octet mesons, π , K , and η . Note that the octet mesons are not strictly massless because the quarks actually have masses.

When the chiral symmetry is spontaneously broken, the expectation value of the field operator $\bar{\psi}\psi$ for the vacuum, $\langle 0|\bar{\psi}\psi|0\rangle$, has a non-zero value. The $\langle 0|\bar{\psi}\psi|0\rangle$ value, called the quark condensate, is used as an order parameter of the chiral symmetry breaking [6]. The quark condensate leads to a dynamical quark mass of the order of $300 \text{ MeV}/c^2$, and explains the nucleon masses of the order of $1 \text{ GeV}/c^2$ in the constituent quark model [7].

1.2.3 Restoration of chiral symmetry in nuclear medium

Theoretical studies suggested that quark condensate decreases at high temperatures or high baryon densities, and thus the chiral symmetry is expected to restore in such environment [8, 9]. Therefore, possible changes of hadron masses under such environment have been studied both theoretically and experimentally. The nuclear medium has often been used as a high-density environment [6]. The quark condensate is estimated to decrease by 37% at normal nuclear density $\rho_0 = 0.17 \text{ fm}^{-3}$ [10]. Some experiments have been performed to investigate mass modification of hadrons, such as mesons, in nuclear medium by generating them inside a nucleus [11–18].

In this thesis, mass modification of a light pseudoscalar meson, η' , in nuclear medium is studied. The properties and characteristics of an η' meson are described in the following section.

1.2.4 η' meson and the axial U(1) anomaly

The singlet meson, $\eta' (\approx \eta_0)$, has particularly larger mass compared to the octet mesons as shown in Table. 1.1. The η' meson is associated with the axial U(1) symmetry. Unlike the octet mesons, it is not a NG boson. It is known that the axial-vector current corresponding to the axial U(1) transformation, $j_A^{0\mu}$, is not conserved [19]:

$$j_A^{0\mu} = \bar{\psi} \gamma^\mu \gamma_5 \psi, \quad (1.19)$$

$$\partial_\mu j_A^{0\mu} = 2i\bar{\psi} \gamma_5 M \psi + \frac{1}{16\pi^2} \epsilon^{\mu\nu\lambda\sigma} G_{\mu\nu}^a G_{\lambda\sigma}^a. \quad (1.20)$$

Due to the second term of (1.20), the divergence of the axial-vector current does not vanish in the massless limit ($M \rightarrow 0$). This is called the axial U(1) anomaly. This means that the axial U(1) symmetry is explicitly broken, and thus the η' meson is not as light as NG bosons.

The anomaly effect to the η' mass can appear only if the chiral symmetry is broken [20]. It is predicted by various models that η' mass significantly decreases in nuclear medium along with the partial restoration of chiral symmetry. In this regard, the η' meson can be a good probe to investigate the role that chiral symmetry and the axial U(1) anomaly play in the mass generation. In the next section, examples of theoretical models and experimental studies associated with the η' mass modification in nuclear medium are introduced.

Table 1.1: Mass of psuedoscalar mesons [1].

meson	mass(MeV/c ²)
π^0	134.98
π^\pm	139.57
K^0	497.61
K^\pm	493.66
η	547.86
η'	957.78

1.3 Theoretical models on the η' mass in nuclei

In this section, theoretical models which suggest the mass modification of the η' meson at finite density are described.

1.3.1 NJL model

Nagahiro *et al.* calculated η' mass modification based on the Nambu-Jona-Lasinio (NJL) model [7, 21, 22]. They used the following Lagrangian density:

$$\mathcal{L} = \mathcal{L}_0 + \mathcal{L}_4 + \mathcal{L}_6, \quad (1.21)$$

$$\mathcal{L}_0 = \bar{\psi}(i\partial_\mu\gamma^\mu - M)\psi, \quad (1.22)$$

$$\mathcal{L}_4 = \frac{g_S}{2} \sum_a [(\bar{\psi}\lambda^a\psi)^2 + (\bar{\psi}\lambda^a i\gamma_5\psi)^2], \quad (1.23)$$

$$\mathcal{L}_6 = g_D \{ \det [\bar{\psi}_i(1 - \gamma_5)\psi_j] + h.c. \}. \quad (1.24)$$

The interaction term including 4-fermion interaction, \mathcal{L}_4 , is invariant under chiral $U(3)_L \times U(3)_R$ transformation. This term causes spontaneous breaking of chiral symmetry, and then the quark condensate and the constituent quark mass are self-consistently determined from the gap equation. Since the quark condensate has a relation with the baryon density as described in Sec. 1.2.3, the density dependence of η' mass is obtained by this calculation. The Kobayashi-Maskawa-'t Hooft interaction term [23, 24] \mathcal{L}_6 breaks the axial $U(1)$ symmetry, namely, represents the axial $U(1)$ anomaly. The coupling constant g_D represents the strength of the anomaly effect. They calculated meson mass spectra at finite density in three cases of the density dependence of g_D : (a) $g_D(\rho) = g_D$, (b) $g_D(\rho) = 0$, (c) $g_D(\rho) = g_D \exp[-(\rho/\rho_0)^2]$. Note that the case (b) corresponds to the calculation with no anomaly effect. Figure 1.2 shows their results. They predicted a large reduction of η' mass, $\Delta m_{\eta'} \sim -150 \text{ MeV}/c^2$, at the normal nuclear density ρ_0 in the case that g_D was assumed to be constant.

1.3.2 Linear sigma model

Sakai *et al.* reported a prediction based on the linear sigma model [25]. The Lagrangian of the linear sigma model is written by the hadron fields as the fundamental

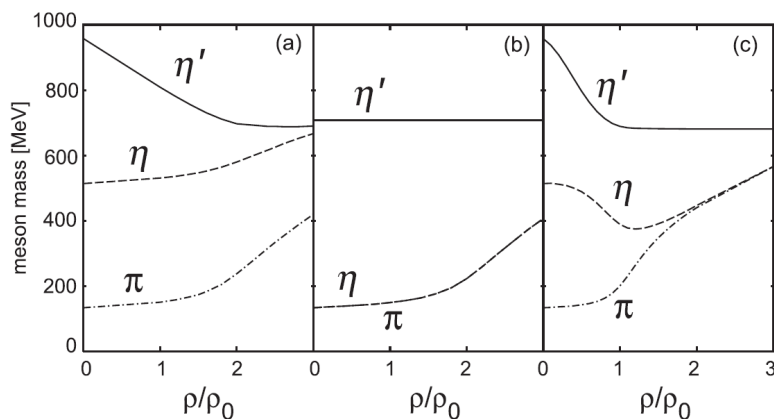


Figure 1.2: The density dependence of meson mass spectra calculated with the NJL model [22]. The density dependences of the anomaly parameter g_D are assumed as follows: (a) $g_D(\rho) = g_D$, (b) $g_D(\rho) = 0$, (c) $g_D(\rho) = g_D \exp[-(\rho/\rho_0)^2]$

degree of freedom and constructed to possess the same global symmetry as QCD [26]. The spontaneous breaking of chiral symmetry is described with the σ condensate as an order parameter instead of the quark condensate. They also used the term corresponding to the Kobayashi-Maskawa-'t Hooft interaction, which breaks the axial U(1) symmetry. They did not include the density dependence of the strength of the anomaly effect. Figure 1.3 shows their results. They evaluated the η' mass reduction at the normal nuclear density $\Delta m_{\eta'} \sim -80 \text{ MeV}/c^2$.

1.3.3 QMC model

An evaluation using the quark-meson-coupling (QMC) model was given by Bass *et. al.* [27]. The QMC model is described explicitly based on quark degrees of freedom [28]. They evaluated the mass of η and η' mesons in nuclear matter for a given η - η' mixing angle. They suggested an η' mass reduction of $\Delta m_{\eta'} \sim 40\text{--}80 \text{ MeV}/c^2$ in the ranges of η - η' mixing angles $\theta = -20\text{--}0^\circ$.

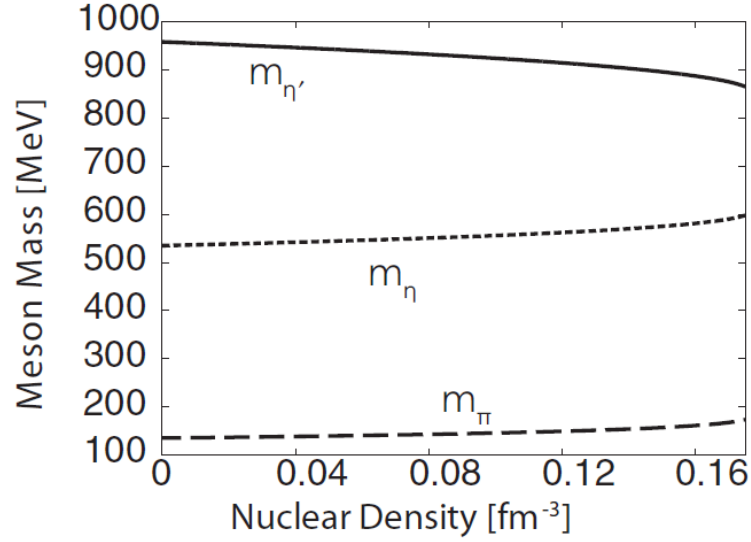


Figure 1.3: The density dependence of meson mass spectra calculated with the linear sigma model [25]. The normal nuclear density is $\rho_0 = 0.17 \text{ fm}^{-3}$.

1.4 Experimental studies on the η' mass in nuclei

One of the experimental approaches to investigate the η' mass modification in nuclear medium is to measure the η' -nucleus optical potential, which can be written as

$$U_{\eta'}(r) = V(r) + iW(r), \quad (1.25)$$

where V and W are real and imaginary part of the optical potential, respectively, and r is the distance between the meson and the center of the nucleus. The η' mass reduction at the normal nuclear density ρ_0 , $\Delta m_{\eta'}(\rho_0)$ is associated with the real part of the optical potential [22, 29] as

$$V(r) = \Delta m_{\eta'}(\rho_0) \frac{\rho(r)}{\rho_0}. \quad (1.26)$$

Also, the imaginary part of the optical potential is related to the meson absorption in nuclear medium, and related to the im-medium η' width $\Gamma_{\eta'}$ as

$$W(r) = -\frac{1}{2} \Gamma_{\eta'} \frac{\rho(r)}{\rho_0}. \quad (1.27)$$

The CBELSA/TAPS collaboration evaluated the depth of the η' -nucleus optical potential in photon induced reactions on ^{12}C nucleus [30]. They measured the excitation function and momentum distribution of η' mesons, and compared the data with theoretical model calculations in different $V(\rho_0)$ cases. Their analysis indicated an attractive potential of $-(37 \pm 10(\text{stat.}) \pm 10(\text{syst.}))$ MeV depth at the normal nuclear density. This value corresponds to the mass reduction at the normal nuclear density, as can be seen from Eq. (1.26).

Another experimental approach is to search for η' -nucleus bound states. If the absorption is small compared with the depth of the η' -nucleus potential, η' -nucleus bound states could be formed [29, 31, 32]. The η -PRiME/Super-FRS collaboration measured the missing mass spectrum near the η' emission threshold in $^{12}\text{C}(p, d)$ reactions aiming to search for narrow peaks of η' -nucleus bound states on the spectrum [33]. No distinct structure was observed indicating the formation of η' -nucleus bound states in their analysis. They claimed that a large mass reduction of $\Delta m_{\eta'} \sim -150$ MeV/ c^2 as predicted by the NJL model was disfavored although the determined upper limit of the optical potential has large ambiguity depending on the theoretical calculation of formation cross sections for the bound states. Furthermore, the LEPS2/BGOegg collaboration recently reported the analysis results of search for η' -nucleus bound states in the missing mass spectroscopy of $^{12}\text{C}(\gamma, p)$ reaction [34]. They tagged the $\eta'N \rightarrow \eta N$ process as a possible decay process from η' -nucleus bound states in order to reduce background events coming from multi-meson productions. No signal events indicating the formation of η' -nucleus bound states were observed after kinematical selections. They obtained the experimental upper limit of the signal cross section, and compared with the theoretical calculation as shown in Fig. 1.4. From their results, the deep η' -nucleus optical potential corresponding to a large mass reduction of $\Delta m_{\eta'} \sim -100$ MeV/ c^2 is unfavored under the large branching ratio of the $\eta'N \rightarrow \eta N$ decay process.

1.5 Direct measurement of in-medium meson mass spectra

Although there have been some experimental studies investigating the η' -nucleus optical potential as described in the previous section, they are indirect measurement

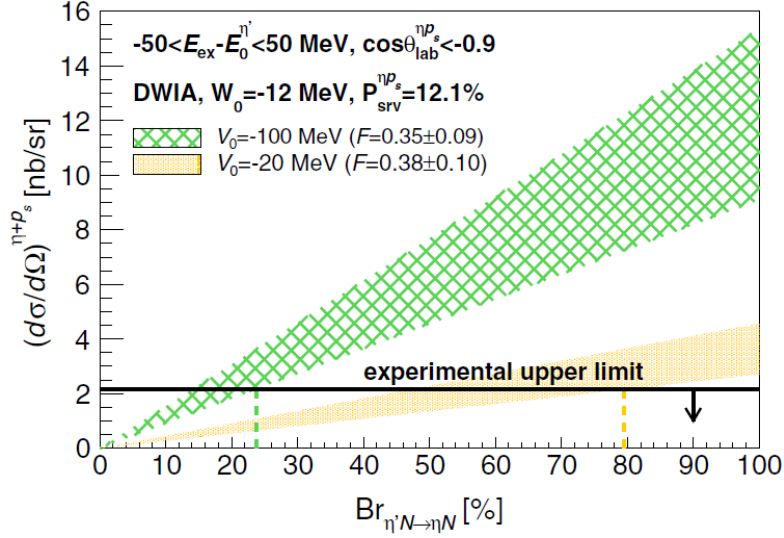


Figure 1.4: The experimental upper limit of the signal cross section compared with theoretical calculations [34].

of in-medium η' mass modification. The most straightforward way to measure the meson mass is to reconstruct the invariant mass of its decay products. However, there have been no experiments measuring directly the mass spectrum of η' mesons decaying in nuclei. In this thesis, the mass spectra of η' mesons in nuclear medium are investigated in a $\gamma+C$ reaction via the $\eta' \rightarrow \gamma\gamma$ decay mode with an electro-magnetic calorimeter. This is the first direct measurement of in-medium η' mass spectra.

We performed a line shape analysis, in which the spectral shape of the invariant mass reconstructed from the decay products of η' mesons is examined. The fundamental method of line shape analysis is based on the analysis of $\phi \rightarrow e^+e^-$ spectra reported by KEK-PS E325 collaboration [15]. They measured invariant mass spectra of e^+e^- pairs in $p + A$ reactions aiming to detect possible in-medium modifications of the ϕ meson, which had also been predicted by theoretical models [9, 35]. They observed a significant excess on the low-mass side of the ϕ meson peak in the slow ($\beta\gamma < 1.25$) region, as shown in Fig. 1.5. They claimed that the observation was consistent with the picture of possible in-medium modifications of the ϕ meson by

$$m_\phi(\rho) = m_\phi(0) \left(1 - k_1 \frac{\rho}{\rho_0} \right), \quad (1.28)$$

$$\Gamma_\phi^{\text{tot}}(\rho) = \Gamma_\phi^{\text{tot}}(0) \left(1 + k_2 \frac{\rho}{\rho_0} \right), \quad (1.29)$$

$$\Gamma_\phi^{ee}(\rho) = \Gamma_\phi^{ee}(0) \left(1 + k_3 \frac{\rho}{\rho_0} \right), \quad (1.30)$$

where $m_\phi(\rho)$, $\Gamma_\phi^{\text{tot}}(\rho)$, and $\Gamma_\phi^{ee}(\rho)$ are the mass, total and partial decay width of ϕ mesons at the density ρ . We adopt the same parametrization as Eq. (1.28)–(1.30) to discuss in-medium modification of meson mass spectra in Chapter 6.

The η' mass spectrum is studied via the $\eta' \rightarrow \gamma\gamma$ decay mode. Since only photons are emitted by the decay, there is no final state interaction of the decay products and no energy loss by bremsstrahlung. These features simplify the measurement and the analysis.

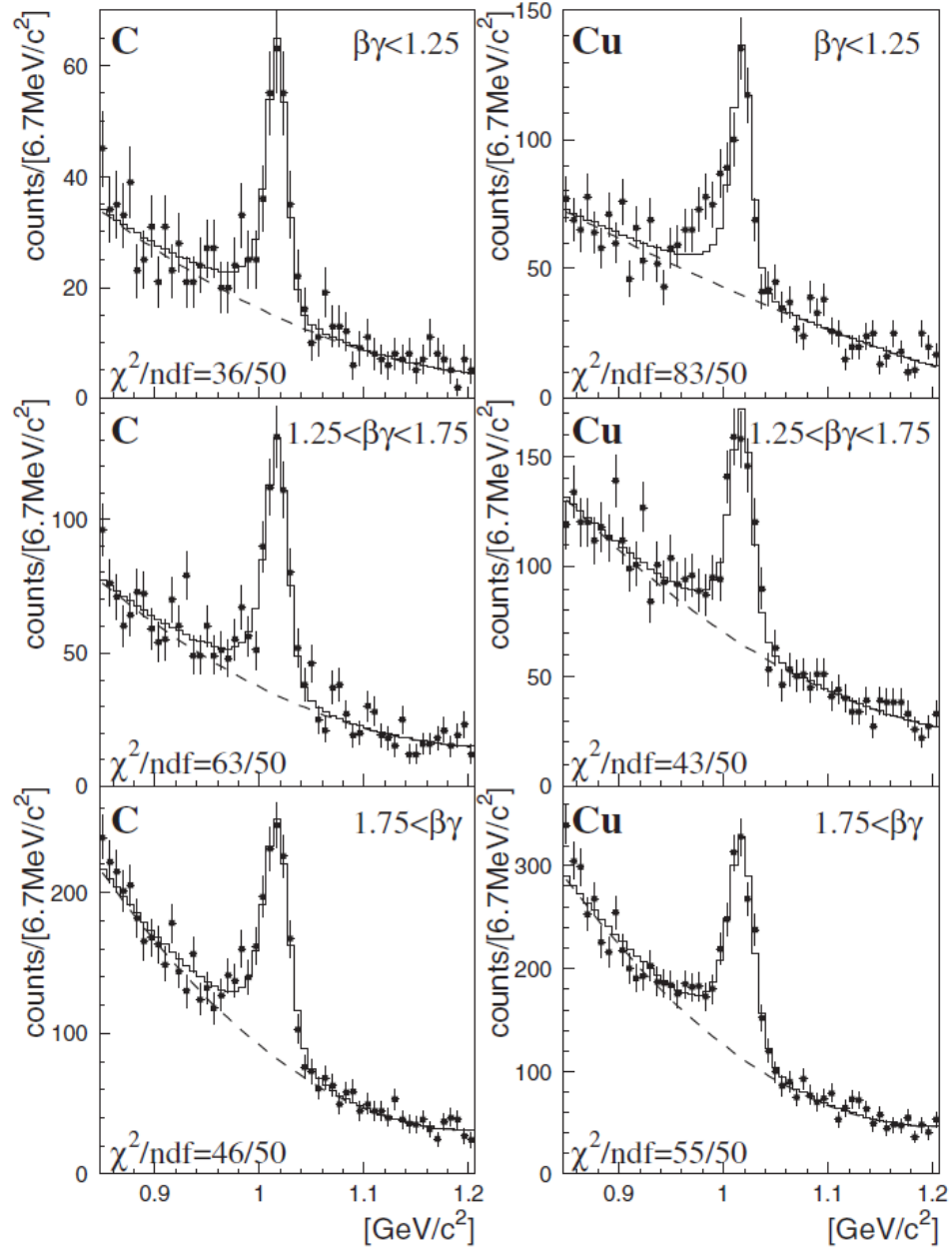


Figure 1.5: The obtained e^+e^- invariant mass spectra by the KEK-PS E325 collaboration with the fit results [15].

Chapter 2

Experiment

The meson-photoproduction experiment was carried out at the SPring-8/LEPS2 beamline using a tagged photon beam with energies up to 2.4 GeV. The experimental setup and the detectors used for this analysis are described in this chapter.

2.1 SPring-8/LEPS2 facility

2.1.1 LEPS2 beamline

SPring-8 is a synchrotron radiation (SR) facility located in Hyogo Prefecture in Japan. There are 62 beamlines shown in Fig. 2.1 [36]. The LEPS2 beamline is located at BL31LEP, which is one of the 30 m long straight sections in the storage ring. Figure 2.2 shows a schematic view of the LEPS2 beamline. The photon beam is produced by backward Compton scattering with ultraviolet laser photons injected onto the 8 GeV electrons circulating in the storage ring [37]. The photon beam is introduced to the experimental building located outside of the storage ring building. The recoil electrons are detected by the tagging counter to measure the energies of produced photons.

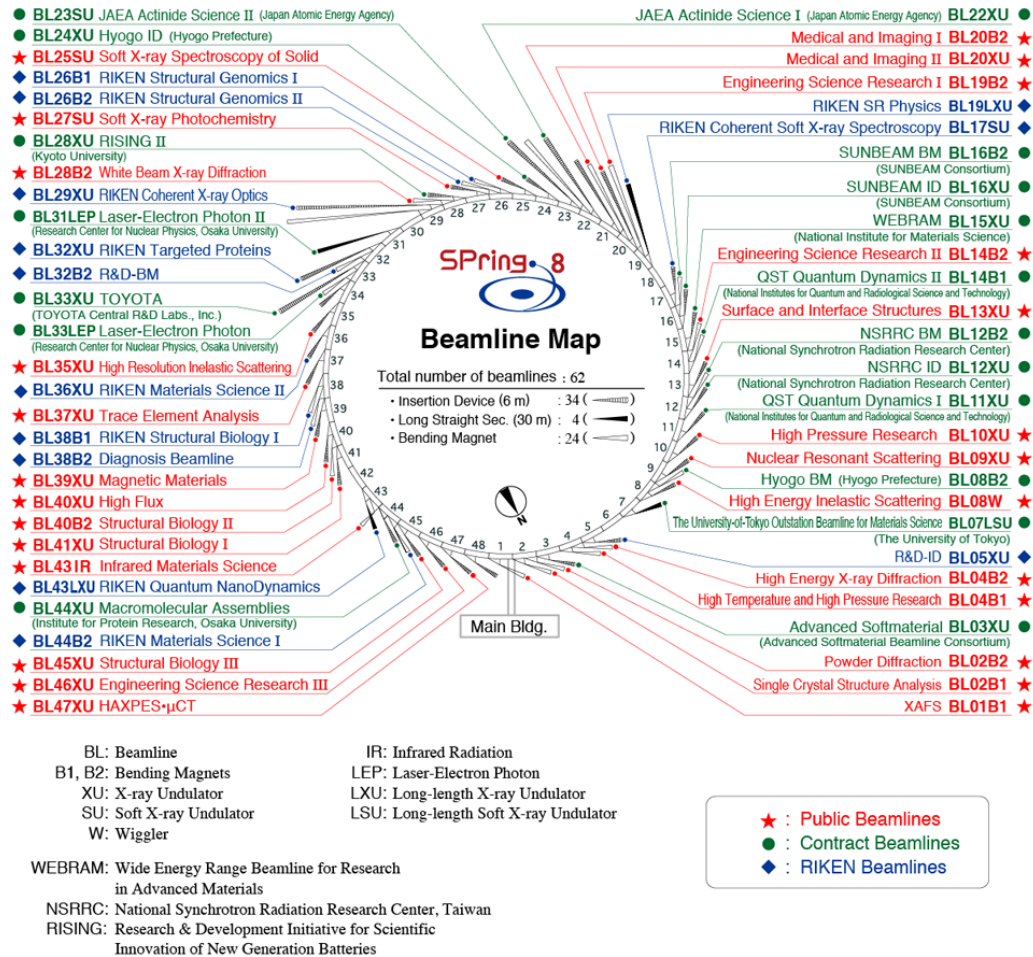


Figure 2.1: The beamline map of the SPring-8 facility [36]. The LEPS2 beamline is located at BL31LEP.

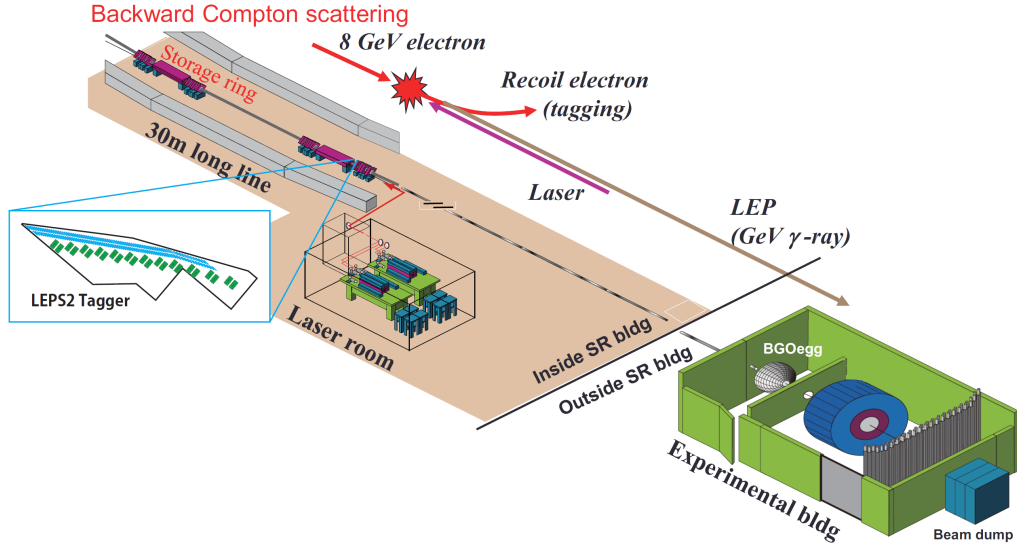


Figure 2.2: The schematic view of the LEPS2 beamline..

2.1.2 Backward Compton scattering

The principle of generating a photon beam by backward Compton scattering (BCS) is described in this section. When a laser photon with momentum \vec{P}_i and an electron with momentum \vec{P}_e collides head-on, the four-momentum conservation gives

$$|\vec{P}_i| + \sqrt{|\vec{P}_e|^2 + m_e^2} = |\vec{P}_f| + \sqrt{|\vec{P}'_e|^2 + m_e^2}, \quad (2.1)$$

$$\vec{P}_i + \vec{P}_e = \vec{P}_f + \vec{P}'_e, \quad (2.2)$$

where \vec{P}_f and \vec{P}'_e are the momenta of the emitted photon and electron after Compton scattering, respectively. $m_e = 0.511 \text{ MeV}/c^2$ is the electron mass. We can solve the equation to obtain the energy of the final photon $E_\gamma = |\vec{P}_f|$ as follows:

$$E_\gamma = \frac{|\vec{P}_i||\vec{P}_e| + |\vec{P}_i|\sqrt{|\vec{P}_e|^2 + m_e^2}}{|\vec{P}_i| + \sqrt{|\vec{P}_e|^2 + m_e^2} + (|\vec{P}_i| - |\vec{P}_e|) \cos \theta_\gamma}, \quad (2.3)$$

where θ_γ is the emission angle of the final photon. If $|\vec{P}_e| \gg |\vec{P}_i|$, the final photon is directed in the backward direction ($\theta_\gamma \approx 0$) due to the Lorentz boost. Then Eq. (2.3)

can be rewritten as

$$E_\gamma = \frac{4|\vec{P}_i||\vec{P}_e|^2}{m_e^2 + 4|\vec{P}_i||\vec{P}_e| + |\vec{P}_e|^2\theta_\gamma^2}, \quad (2.4)$$

by using an approximation with $|\vec{P}_e| \gg m_e$ and $\theta_\gamma \approx 0$. The maximum energy of an emitted photon, the Compton edge E_γ^{\max} , is obtained at $\theta_\gamma = 0$:

$$E_\gamma^{\max} = \frac{4|\vec{P}_i||\vec{P}_e|^2}{m_e^2 + 4|\vec{P}_i||\vec{P}_e|}. \quad (2.5)$$

We used $|\vec{P}_e| = 7.975$ GeV for incoming electrons and $|\vec{P}_i| = 3.49$ eV for laser photons with a wave length of 355 nm [37], and then E_γ^{\max} is calculated to be 2.385 GeV.

The differential cross section of Compton scattering in the laboratory frame is written as follows [38]:

$$\frac{d\sigma}{dE_\gamma} = \frac{2\pi r_e^2 a}{E_\gamma^{\max}} (\chi + 1 + \cos^2 \alpha), \quad (2.6)$$

where

$$a = \frac{m_e^2}{m_e^2 + 4|\vec{P}_i||\vec{P}_e|}, \quad (2.7)$$

$$\chi = \frac{\rho^2(1-a)^2}{1-\rho(1-a)}, \quad (2.8)$$

$$\cos \alpha = \frac{1-\rho(1+a)}{1-\rho(1-a)}, \quad (2.9)$$

$$\rho = \frac{E_\gamma}{E_\gamma^{\max}}. \quad (2.10)$$

Here, $r_e = 2.818$ fm is the classical electron radius. Fig. 2.3 shows the E_γ dependence of the differential cross section of backward Compton scattering. The BCS spectrum is enhanced around the maximum energy E_γ^{\max} . Therefore, BCS photons will dominate in high energy photons compared to bremsstrahlung photons generated via residual gas in the electron storage ring.

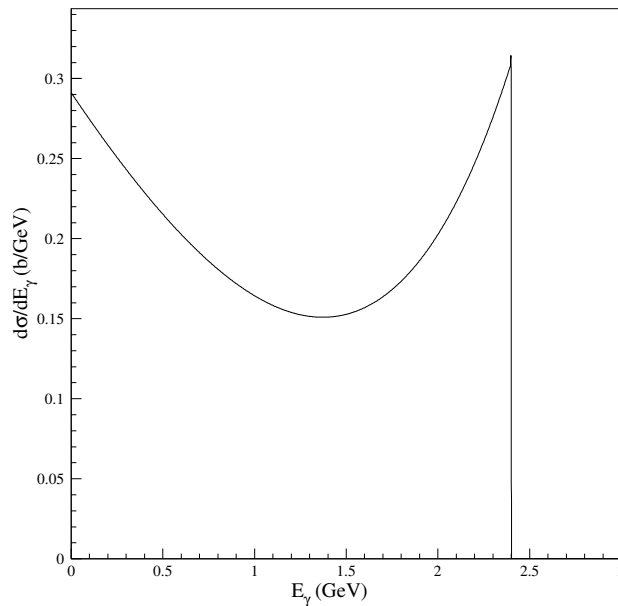


Figure 2.3: The differential cross section of backward Compton scattering.

2.1.3 Tagging counter

The energy of a BCS photon is tagged by detecting the recoil electron with the LEPS2 tagging counter. The recoil electrons are bent by the magnet located downstream of the collision point. These electrons hit different positions of the tagging counter depending on their momenta. Then the energy of a recoil electron E_e is determined by analyzing the tracks, and the energy of the BCS photon E_γ is obtained by

$$E_\gamma = E_e - E'_e, \quad (2.11)$$

where $E_e = 7.975$ GeV is the energy of electrons circulating in the storage ring. Fig. 2.4 shows a schematic drawing of the LEPS2 tagging counter. The tagging counter consists of two layers of 1 mm square scintillating fiber (SciFi) hodoscopes and two layers of plastic scintillator (PS) hodoscopes. The SciFi hodoscopes are placed upstream of the PS hodoscopes. The SciFi layers are arranged so that the center of fibers are 0.5 mm shifted from each other. They cover a region corresponding to

BCS-photon energies above 1.3 GeV.

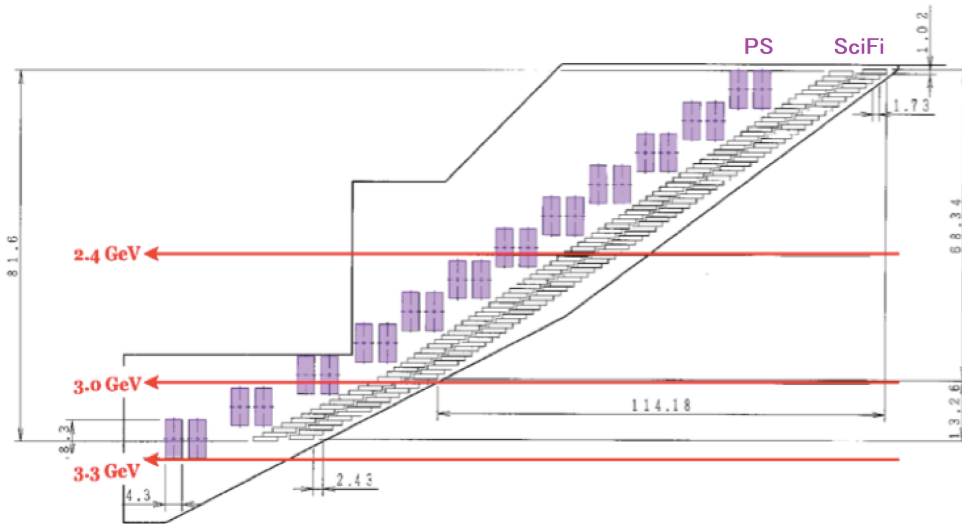


Figure 2.4: A schematic drawing of the LEPS2 tagging counter.

2.1.4 Target

A carbon target was used in this experiment. The thickness is 20.0 mm and the density is measured to be 1.73 g/cm^3 . The target holder is made of a 10 mm thick polystyrene foam and a 0.125 mm thick kapton foil. Pictures of the carbon target and the holder are shown in Fig. 2.5.

2.2 Detectors

The photon beam is transported to the target placed approximately 125 m downstream from the BCS collision point, and reactions are induced on the target nuclei. Photoproduced particles and their decay products are detected by the detectors installed in the LEPS2 experimental building. Figure 2.6 shows a schematic drawing of the detector setup in the LEPS2 building. An electro-magnetic calorimeter BGOegg covers a large solid angle around the target. Inner plastic scintillator (IPS) hodoscopes and a cylindrical drift chamber (CDC) are installed inside BGOegg to detect charged

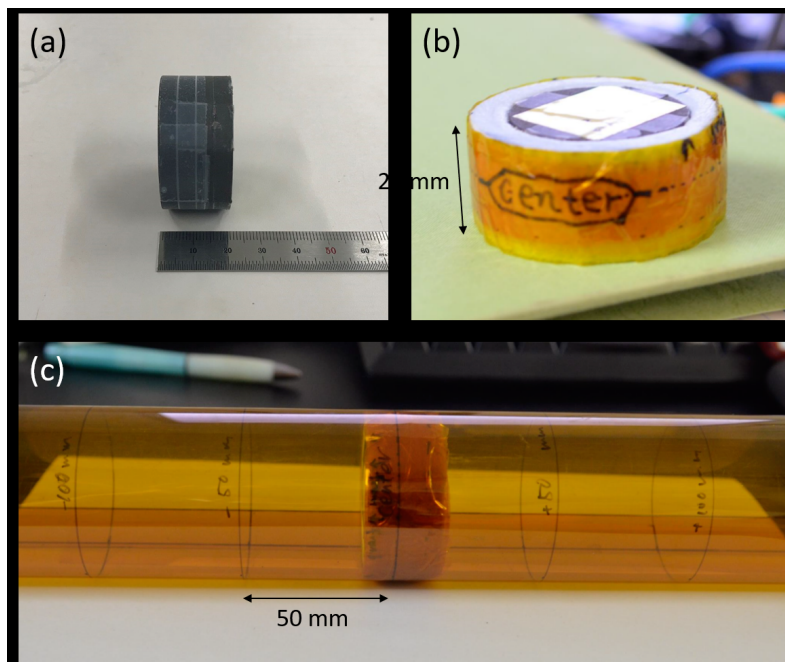


Figure 2.5: (a)The carbon target. (b)(c)The target holder.

particles. A drift chamber (DC) and a resistive plate chamber (RPC) wall are installed downstream of BGOegg to detect particles emitted in forward direction. A plastic scintillator named UpVeto is installed upstream of BGOegg to exclude events in which an incident photon is converted to an e^+e^- pair before reaching the target. In this work, CDC and forward detectors (DC, RPC) were not used in the data analysis. Details of each detector strongly related to this analysis are described in the following subsections.

2.2.1 BGOegg calorimeter

BGOegg is an egg-shaped electro-magnetic calorimeter consisting of 1320 $\text{Bi}_4\text{Ge}_3\text{O}_{12}$ (BGO) crystals, which cover a polar angle of from 24 to 144 degrees and the whole azimuthal angles surrounding the target. Figure 2.7 shows a schematic view of BGOegg. The forward and backward parts of BGOegg are divided into 13 and 9 layers in the polar direction, respectively, and each layer is divided into 60 pieces in the azimuthal direction. We define the layer numbers $i = 1, 2, \dots, 22$ from the downstream side, and

incident positron (or photon) energy E is described as follows [39]:

$$\left(\frac{\sigma_E}{E}\right)^2 = (0.63\%) + (1.15\% \pm 0.04\%)^2/(E/\text{GeV}) + (0.42\% \pm 0.03\%)^2/(E/\text{GeV})^2, \quad (2.13)$$

i.e., $1.38\% \pm 0.05\%$ for 1-GeV photons. The position resolution is $3.07\% \pm 0.03\%$ for 1-GeV photons [39].

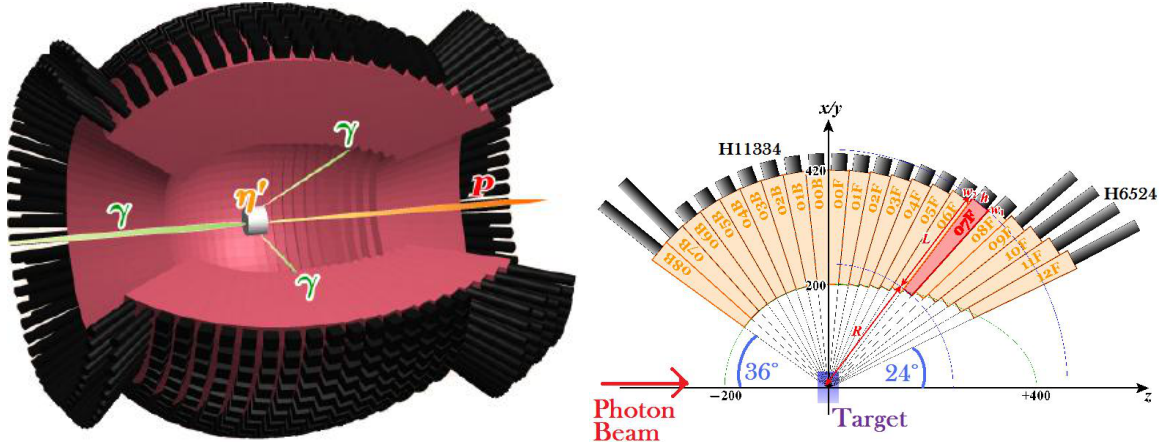


Figure 2.7: A schematic drawing view of BGOegg.

2.2.2 Inner plastic scintillator hodoscopes

The inner plastic scintillator (IPS) hodoscopes are installed inside BGOegg, as shown in Fig. 2.8, in order to identify charged particles. The inner hodoscopes consists of 30 plastic scintillators with a size of 453 mm \times 26 mm \times 5 mm. The signals are read with multi pixel photon counters (MPPCs) connected to the upstream sides of the scintillators. One or two scintillators covers each BGOegg crystal.

2.2.3 UpVeto counter

A plastic scintillator named UpVeto is installed upstream of BGOegg. BCS photons sometimes convert e^+e^- pairs before reaching the target due to the materials in the beamline. These events are removed in the data analysis by using the UpVeto counter. The UpVeto counter is made of a plastic scintillator with a size of 620 mm \times 620 mm

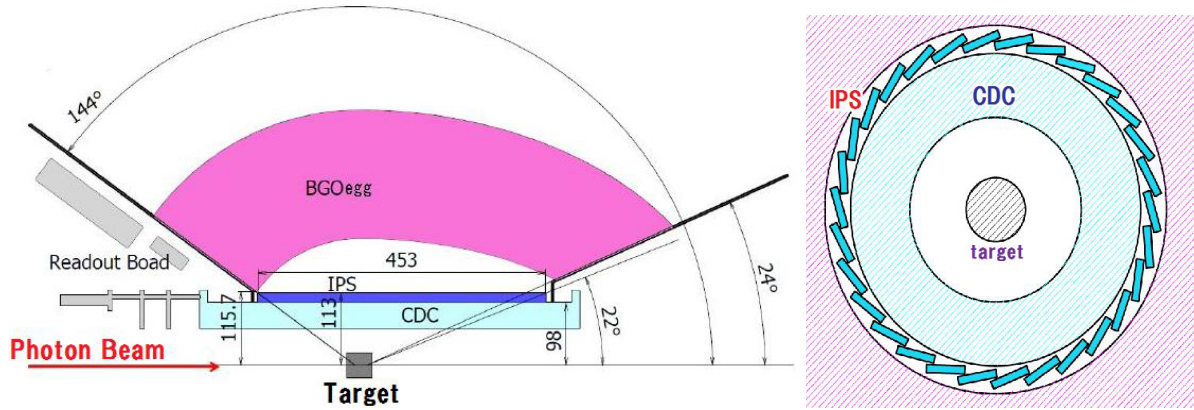


Figure 2.8: A schematic drawing of the configuration of BGOegg and inner detectors (left), and the front view of the inner hodoscopes (right).

$\times 3$ mm. A fine-mesh PMT (Hamamatsu Photonics H6614-70mod) is connected to the plastic scintillator through a light guide.

2.3 Trigger logic

The trigger signals for data acquisition are generated with a signal logic described in Fig. 2.9. Signals from BGOegg is divided into 88 blocks (4 blocks for each layer), and the sum-out signals, which are proportional to the number of fired channels in each block, are provided by using the LeCroy 4413 discriminator modules. The GeV- γ 139 module [40] gives the analog sum of these sum-out signals, and outputs a logical signal if the analog sum exceeds the set threshold. In this experiment, the threshold was set to output the trigger signal when two or more BGOegg crystals were fired. The trigger signal additionally requires a coincidence with BGOegg hits and tagger-PS hits. The trigger signal from the tagging counter is generated when two tagger-PSs in pair have hits. Then, the logical sum of the trigger signals from BGOegg and the tagging counter gives an experimental trigger signal. This is denoted as “BGO2hit \otimes Tagger trigger”.

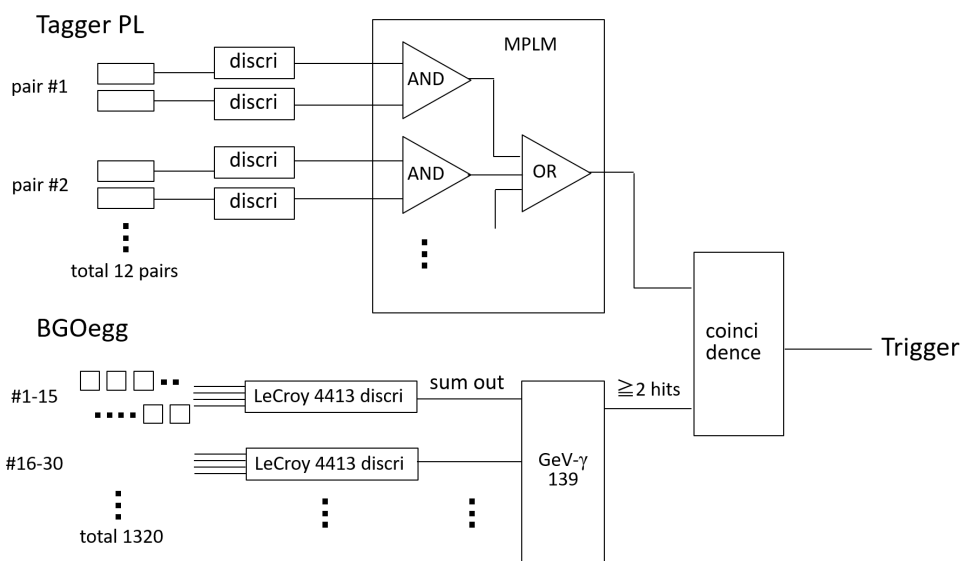


Figure 2.9: The trigger logic.

2.4 Data collection

The experiment was carried out from April to July in 2015. The total number of incident photons in the tagged energy region (1.3–2.4 GeV) is 9.8×10^{12} . The total number of recorded events is 1.3×10^9 . We also took data with a liquid hydrogen target from November in 2014 to February in 2015 [41].

Chapter 3

Calibration

This chapter describes the energy and timing calibration of the BGOegg calorimeter. The reconstruction of particle hits and the fundamental method of energy and timing calibrations are described in Sec. 3.1. Additional corrections for the energy measurement depending on the BGOegg layer are given in Sec. 3.2.

3.1 Fundamental calibration for BGOegg

Mesons in final states are reconstructed with an electro-magnetic calorimeter BGOegg via measuring the energy, timing, and hit position of their decay products, such as photons. In this section, the identification of a BGOegg hit together with the method of energy and timing calibrations, are described.

3.1.1 Energy reconstruction and clustering

An energy deposit E_i for each crystal is evaluated from recorded charge information by

$$E_i = \alpha_i(A_i - A_{0i}), \quad (3.1)$$

where α_i , A_i , A_{0i} are the gain factor, the integrated charge on Analog-To-Digital Converter (ADC), the pedestal channel of i -th crystal, respectively. Pedestal channels are determined run-by-run as mean values of ADC distributions with the condition

that i -th crystal and crystals within 30 degrees have no hit information on Time-To-Digital Converter (TDC). The gain factors should be determined individually because the gains of PMTs and their supplied voltages are different depending on crystals.

When a photon or an electron comes into a crystal, an electro-magnetic shower occurs. The energy of the shower is recorded as charge information for each crystal. Since the dimension of the front size of a BGO crystal is smaller than the transverse spread of an electro-magnetic shower, which is characterized by Moliere radius $R_M = 22.3$ mm [1], the electro-magnetic shower developed leaks into nearby crystals. Therefore, to reconstruct the total energy of incoming photons or electrons, neighboring crystals with finite ADC values should be clustered and summed up.

A cluster is defined as a set of fired crystals to be connected. In the clustering algorithm, first of all, crystals with TDC information are connected. Second, adjacent crystals only with ADC information corresponding to a small energy deposit are combined. (See Fig. 3.1.) The cluster energy E_{cls} is defined by

$$E_{\text{cls}} = \sum_i \frac{E_i}{m_i}, \quad (3.2)$$

where E_i is the energy deposit for the i -th crystal and m_i is the number of clusters sharing i -th crystal. m_i is usually set to 1. However, in the case that two clusters share i -th crystal, m_i is set to 2 and E_i is divided equally into these two clusters. The hit position of a particle is reconstructed by an energy-weighted mean of the front positions of crystals in a cluster. The hit timing for a cluster is defined by using the timing information of cluster core, which is the crystal with the largest energy deposit.

When inner plastic scintillators in front of a reconstructed cluster are fired, the cluster is called a ‘‘charged cluster’’, otherwise it is called a ‘‘neutral cluster’’. Assuming a neutral cluster corresponds to a photon, the momentum \vec{p} is reconstructed by

$$\vec{p} = E_{\text{cls}} \frac{\vec{r}}{|\vec{r}|}, \quad (3.3)$$

where E_{cls} , \vec{r} are the energy and hit position vector of a cluster, respectively. The detected particle is assumed to come from the center position of a target volume.

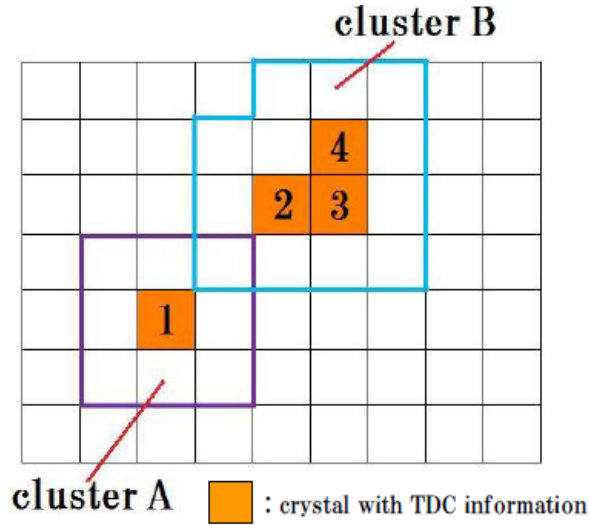


Figure 3.1: An example of the clustering method. In case of this figure, the cluster A consists of crystals inside the violet line, and the cluster B consists of crystals inside the blue line. Crystals with orange color have TDC information.

3.1.2 Energy leakage of a cluster

In general, the size of the electro-magnetic shower doesn't contain inside the reconstructed clusters, e.g., a few % of the energy respect to its total energy is expected to leak out from the cluster. Therefore, the correction of the leaked energy is mandatory to reconstruct the full energy of incident particles. Since the ratio of energy leakage is dependent on particle energy and a hit position, the cluster energy should be corrected as a function of cluster energy and a hit layer. The amount of energy leakage was evaluated by a Monte-Carlo (MC) simulation. The correction is applied before the energy calibration, described in the next subsection.

A MC simulation was developed based on GEANT4 package [42, 43]. In the simulation, photons were generated isotropically at the target position with a fixed energy, which was varied sample by sample in a wide range. The energies of photons have been reconstructed via cluster information at BGOegg as same as real data analysis and compared with the generated energy. The ratio of energy leakage $\Delta E_{\text{leak}}/E$ was determined by

$$\frac{\Delta E_{\text{leak}}}{E} = \frac{E_{\gamma} - E_{\text{cls}}}{E_{\gamma}}, \quad (3.4)$$

where E_γ , E_{cls} are the original energy of generated photons and the mean of a reconstructed cluster energy distribution, respectively. The photon energy E_γ was set every 50 MeV from 50 to 1000 MeV. The cluster energy distribution was plotted for each layer at which the cluster core was found. The correction function was determined by fitting the following function to the energy dependence of estimated leakage:

$$\frac{\Delta E_{\text{leak}}}{E} = C_{1n} \operatorname{erfc}(C_{2n} \sqrt{|\log(C_{3n} E)|})^{C_{4n}} \quad (3.5)$$

$$\equiv f_{\text{leak}}(E; n), \quad (3.6)$$

where n is the layer number of a cluster core, and C_{1n} – C_{4n} are the fitting parameters for the n -th layer. The function $\operatorname{erfc}(x)$ is a complementary error function defined as follows:

$$\operatorname{erfc}(x) = \frac{2}{\sqrt{\pi}} \int_x^\infty \exp(-t^2) dt. \quad (3.7)$$

Figure 3.2 shows the simulated energy leakage ratio as a function of the photon energy. Since a cluster size is determined by the number of fired crystals which is connected by the algorithm mentioned in the previous subsection, a cluster becomes larger as the absolute value of a photon energy increases. On the other hand, the actual spread of an electro-magnetic shower is almost constant around Moliere radius R_M . Therefore, the ratio of energy leakage decreases when photon energy increases.

A corrected cluster energy $E_{\text{cls}}^{\text{corr}}$ is obtained as a numerical solution of the equation

$$E_{\text{cls}}^{\text{corr}} = E_{\text{cls}}^0 + f_{\text{leak}}(E_{\text{cls}}^{\text{corr}}; n) E_{\text{cls}}^{\text{corr}}, \quad (3.8)$$

where E_{cls}^0 is the original cluster energy defined by (3.2). The leak correction was applied for the layers except for the outermost layers, which corresponds to the most forward and backward crystals. The energy leakage of those outermost layers was taken into account in the energy calibration process described in the following subsection.

3.1.3 Energy calibration of BGOegg

The gain factors α are determined so that the mean of a reconstructed π^0 mass peak agrees with the PDG value $m_\pi = 134.977 \text{ MeV}/c^2$ [1]. The invariant mass of a $\gamma\gamma$

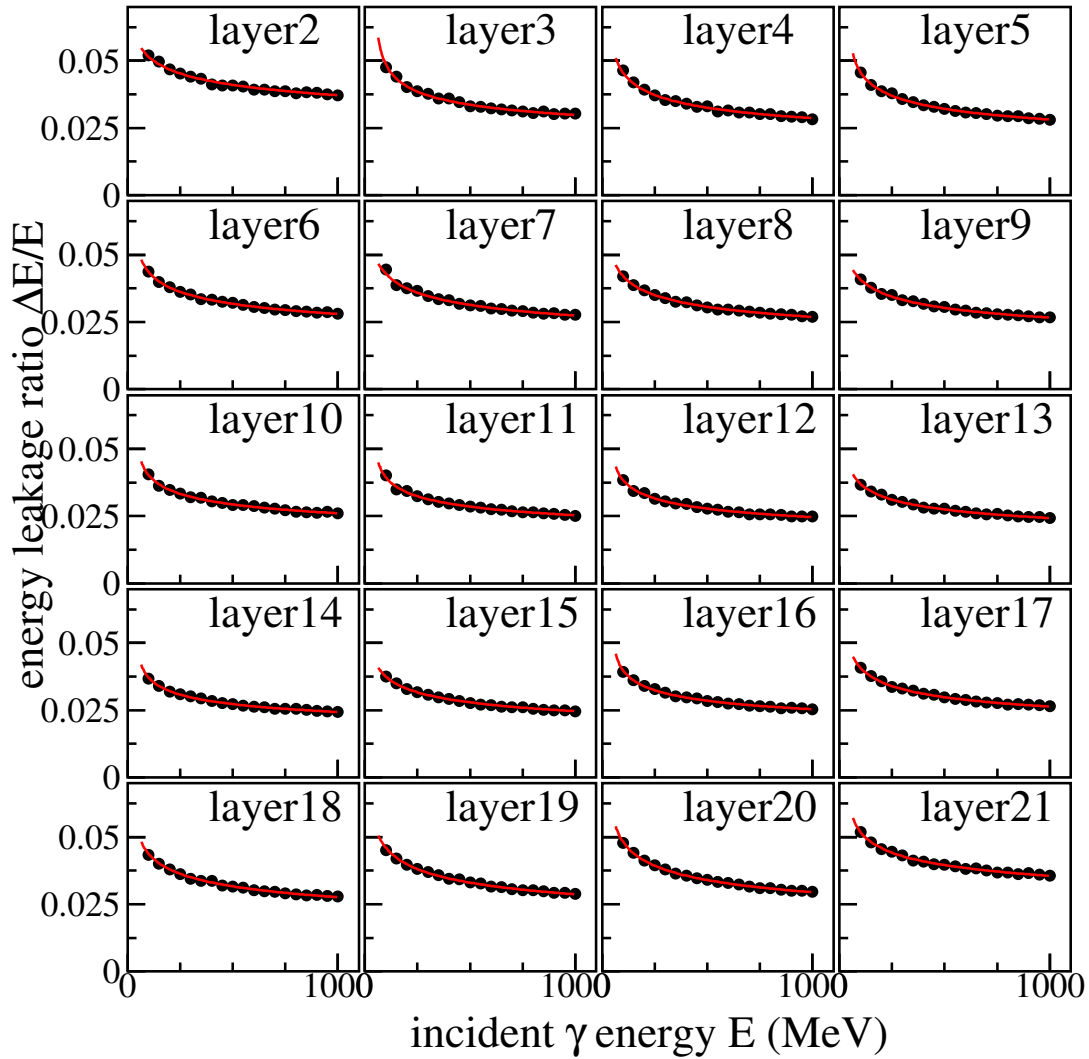


Figure 3.2: The simulated ratio of energy leakage. The fitted results of Eq.(3.5) are shown by red lines.

system is obtained from two neutral clusters by

$$M_{\gamma\gamma} = \sqrt{E_1 E_2 (1 - \cos \theta)}, \quad (3.9)$$

where E_1, E_2 are cluster energies. The cosine of opening angle θ is obtained by

$$\cos \theta = \frac{\vec{r}_1 \cdot \vec{r}_2}{|\vec{r}_1| |\vec{r}_2|}, \quad (3.10)$$

where \vec{r}_1, \vec{r}_2 are the hit position vectors of reconstructed clusters.

The 2γ invariant mass distribution was obtained for each crystal which was assigned to a core of either cluster. A peak structure of $\pi^0 \rightarrow \gamma\gamma$ was observed for every crystal channel. Typical spectra of $\gamma\gamma$ invariant mass are shown in Fig. 3.3. Clusters with energies less than 80 MeV were unused because there were a lot of noise hits and incomplete clusters in the low-energy region. The opening angle of a $\gamma\gamma$ system was also required to be greater than 50 degrees in the Lab frame, because the uncertainty of the hit position became large for nearby clusters with bias for the invariant mass. The reconstructed π^0 mass for i -th crystal, m_i , was obtained by fitting a Gaussian and a 2nd-order polynomial function to the spectrum. The gain factors α_i were adjusted so that m_i agreed with the PDG value of π^0 mass m_π for all channels:

$$\alpha_i^{\text{new}} = \frac{m_\pi}{m_i} \alpha_i^{\text{old}}, \quad (3.11)$$

where $\alpha_i^{\text{new}}, \alpha_i^{\text{old}}$ are adjusted and original gain factors for i -th crystal. For the channels at the outermost layers, the peak position to be adjusted cannot set to the π^0 mass on the PDG because of the existence of the energy leakage to the outside of BGOegg. Therefore, the value is evaluated by a MC simulation, which is found to be 127.9 MeV/ c^2 . Since the gain factors were updated simultaneously for all crystals, this adjustment was repeated until the reconstructed π^0 mass became consistent with the target values for all crystals. The consistency was judged by using χ^2 , defined by

$$\chi^2 = \frac{1}{1320} \sum_{i=1}^{1320} \left(\frac{m_i - m_\pi}{\delta m_i} \right)^2, \quad (3.12)$$

where δm_i was the fitting error of m_i . The χ^2 value finally became below 1 with

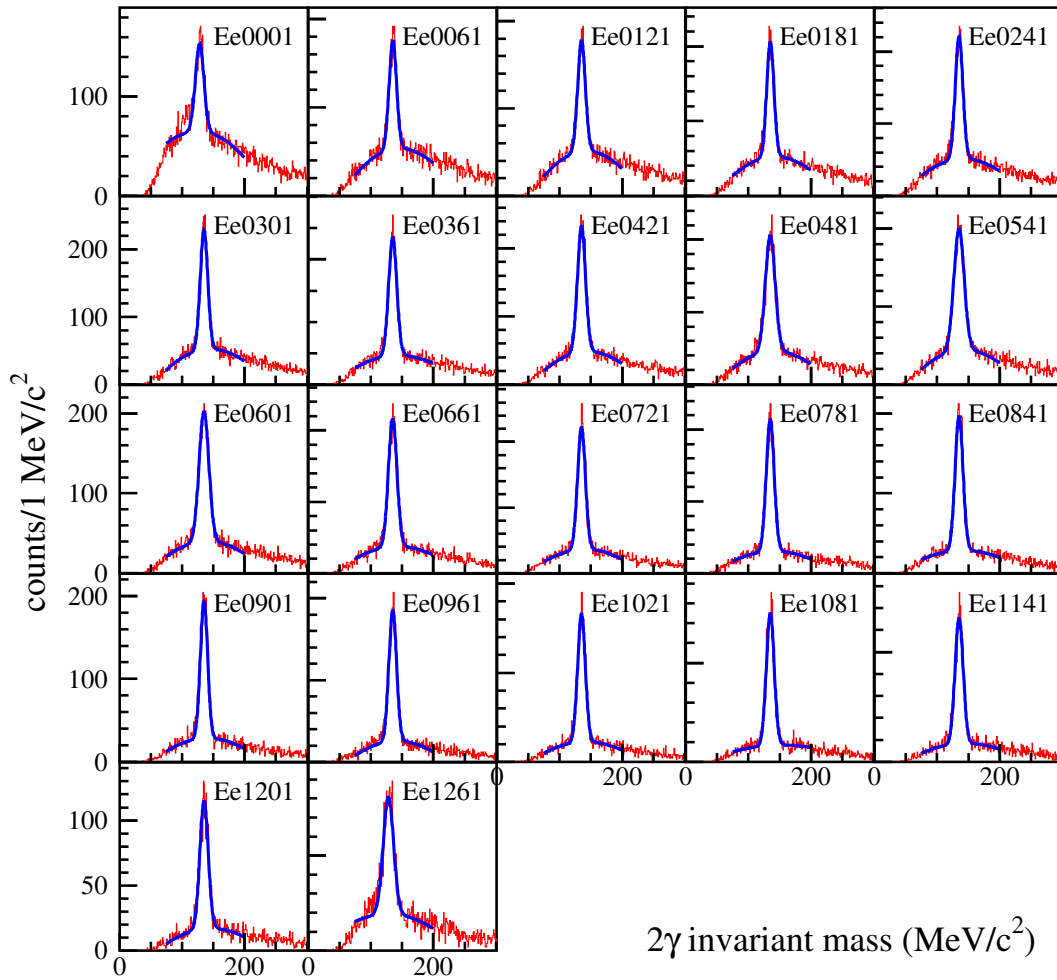


Figure 3.3: Typical $\gamma\gamma$ invariant mass spectra. π^0 peaks are clearly observed. Fitted functions are shown by blue lines. The channel numbers of BGOegg crystals to which the cluster core belong are indicated in the top-right part of individual panels.

iteration of a few times. Figure 3.4 shows the π^0 peak positions after the final iteration. The gain factors were determined roughly every 10 runs in the collected data.

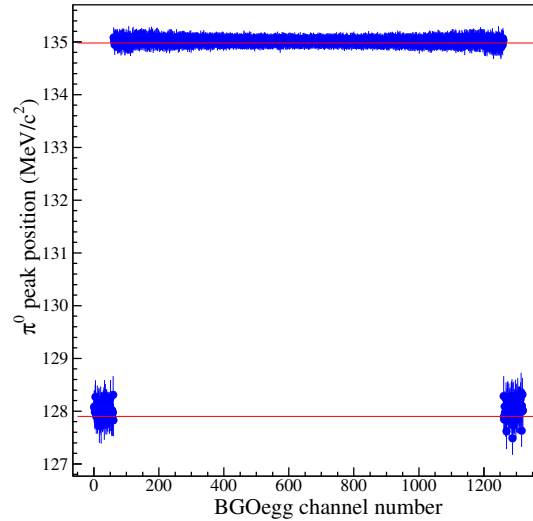


Figure 3.4: The final values of π^0 peak positions. The target values are indicated by red lines at 134.9 MeV/c² and 127.9 MeV/c² for the inner and outermost layers, respectively.

3.1.4 Timing calibration of BGOegg

The timing of i -th crystal hit, t_i , is defined as a time difference to that of the nearest RF signal, t_{RF} :

$$t_i = c_i(T_i - T_{0i}) - t_{\text{RF}}, \quad (3.13)$$

where T_i is the recorded TDC channel for the i -th crystal, and T_{0i} was determined so that the hit timings of photons should be distributed around 0 ns. The value c_i is a coefficient to convert the TDC channel to time in the unit of ns. The value was determined to be $c_i = 0.9871$ ns/channel.

In addition, a time-walk correction that originated via clear correlation between timing determined by leading-edge discriminators and pulse height information (ADC) needs to be applied. The correction is known to be as slewing correction. The slewing correction was performed by fitting the following empirical function to the

ADC-timing correlation for each crystal,

$$t_i = t_{0i} - \alpha_i \tanh(\beta_i(A_i - A_{0i})) - \gamma(A_i - A_{0i}), \quad (3.14)$$

where A_i, A_{0i} are obtained ADC and pedestal channels for i -th crystal, respectively, and $t_{0i}, \alpha_i, \beta_i$ are free parameters obtained by the fitting. The coefficient γ , representing the slope in high-ADC regions, was treated as a fixed parameter in the fit. γ was determined every run set in the collected data by fitting a linear function to the ADC-timing correlation in the high-ADC region. In the slewing-correction process, photons from the $\pi^0 \rightarrow \gamma\gamma$ decay were selected in order to eliminate accidental noise hits. In this analysis, the requirement of the reconstructed invariant mass of $\gamma\gamma$ to be in the range from 114 to 156 MeV/ c^2 is taken. Figure 3.5 shows the ADC-timing correlation with fitting results.

3.2 Additional correction of cluster energy

Even after the fundamental energy calibration described in the previous section, some problems with obtained cluster energies have remained. This section describes details of these problems and an additional correction to fix them.

3.2.1 Problems of obtained gain factors

As described in the previous section, the gain factors defined by the equation (3.1) were determined based on the π^0 mass. They should be applicable to any energy region of photon hits as long as the linearity of a PMT output to the energy deposit is guaranteed. Therefore, a $\gamma\gamma$ invariant mass distribution for the η meson must be correctly peaked at the PDG value, too. However, as shown in Fig. 3.6, the gain factors obtained independently based on the η mass, α^η , were different from those based on the π^0 mass, α^π . Here, the gain factors α^η were determined in the same way described in the previous section except for using a $\eta \rightarrow \gamma\gamma$ peak. The target values to be adjusted was 547.8 MeV/ c^2 and 519.9 MeV/ c^2 for the inner and outermost layers, respectively (see Figure 3.7). To understand the inconsistency of gain factors α^π and α^η , the following comparisons were performed.

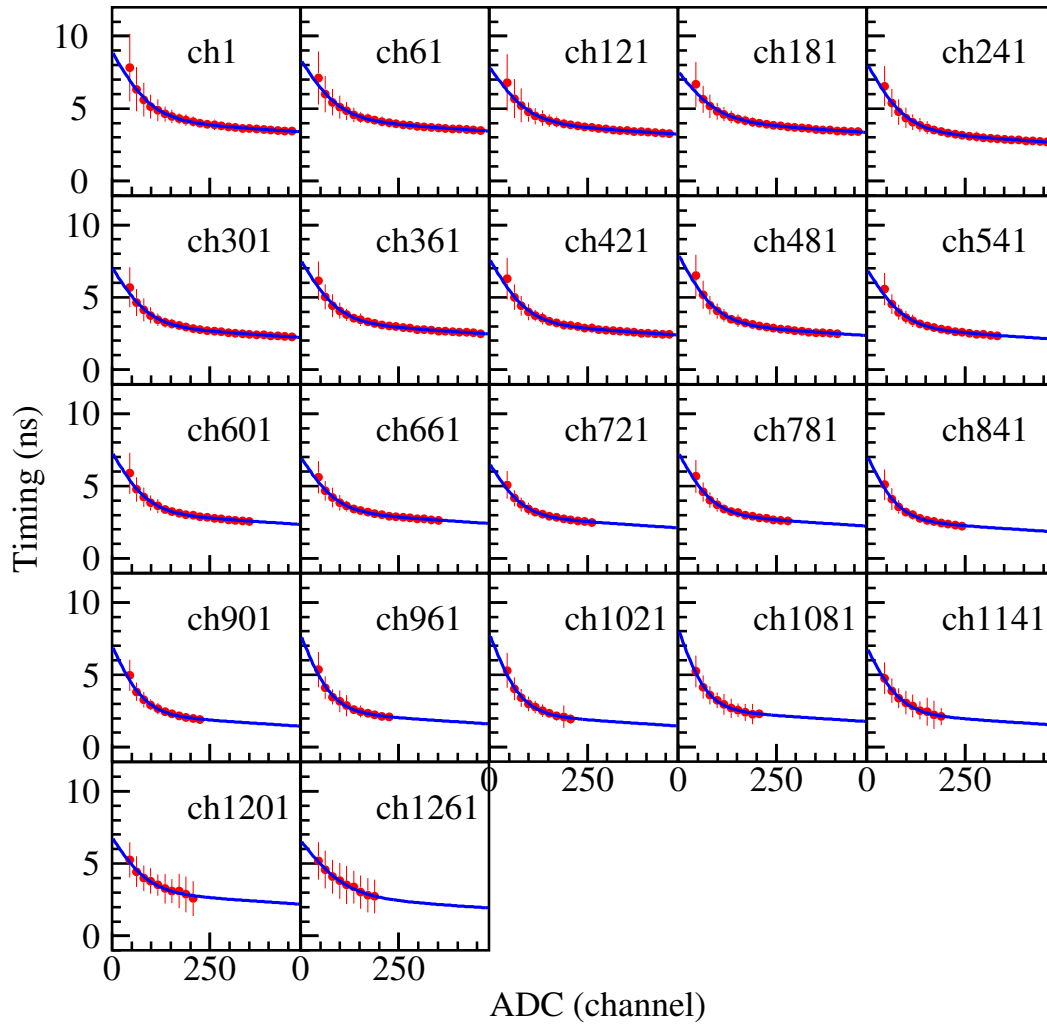


Figure 3.5: The ADC-timing correlation BGOegg hits. The fitted functions are shown by blue lines.

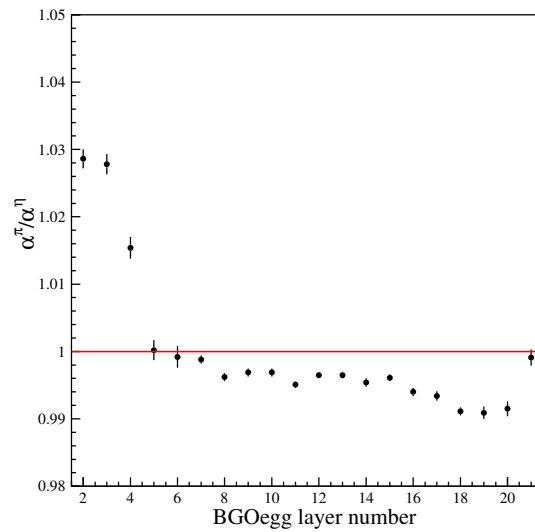


Figure 3.6: The ratio of gain factors based on the π^0 mass and those based on the η mass (α^π/α^η).

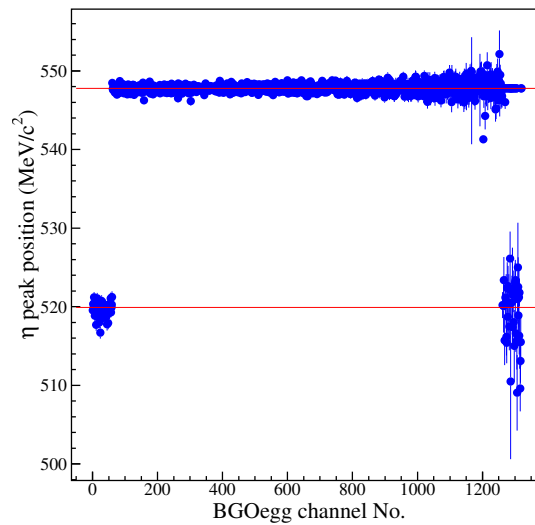


Figure 3.7: The final values of η peak positions in an independent gain calibration. The target values are indicated by red lines at $547.8 \text{ MeV}/c^2$ and $519.9 \text{ MeV}/c^2$ for the inner and outermost layers, respectively.

Layer dependence of π^0 mass

To check the gain factors depending on the BGOegg layer number, the π^0 mass was reconstructed for each layer where the core crystal of either photon cluster was found. Figure 3.8 shows the reconstructed π^0 mass for some of the forward layers. In this figure, one of the two neutral clusters corresponds to the layer number described in the upper side of each panel, while the other cluster belongs to the layer number represented in the horizontal axis. The gain factors α^η were used to plot this figure. The reconstructed π^0 mass obviously becomes lower when using a cluster whose core belongs to forward layers up to the 4th layer. Furthermore, the reconstructed π^0 mass decreases more significantly when both two photons hit in the forward layers. This behavior suggests that α^η 's are too low in the layers 2–4 for lower photon energies corresponding to the $\pi^0 \rightarrow \gamma\gamma$ decay when they are adjusted based on the η mass.

Layer dependence of η mass

Figure 3.9 shows the reconstructed η mass for each combination of γ hit layers in the same way as the analysis for π^0 mass. Here α^η 's are used again as gain factors. Unlike the case of π^0 mass, there is no layer dependence in the reconstructed η mass, and the observed dependence is consistent with a MC simulation result for any combination of hit layers. This result confirms that α^η 's give low gains in the forward layers only when the cluster energies are relatively low, because the difference of π^0 and η leads to different energy coverages of photon clusters. In contrast, α^π 's must show high gains in the forward layers when the cluster energies are high, as recognized from Fig. 3.6.

The reason of the gain factor inconsistency

From the above studies, the deviation of α^η from α^π appears when a cluster belongs to the forward layers up to the 4th layer and has a low energy corresponding to photons coming from π^0 . Simultaneously, α^π 's are unreasonably higher than α^η 's in the same forward layers.

Considering the clear changes between the 4th and 5th layers, as seen in Figs. 3.6 and 3.8, the problem seems to come from the difference of signal-readout PMT types: that is, H6524 was used for the forward region up to the 4th layer, and H11334 was used for the other layers. Based on our observation, it is deduced that the linearity

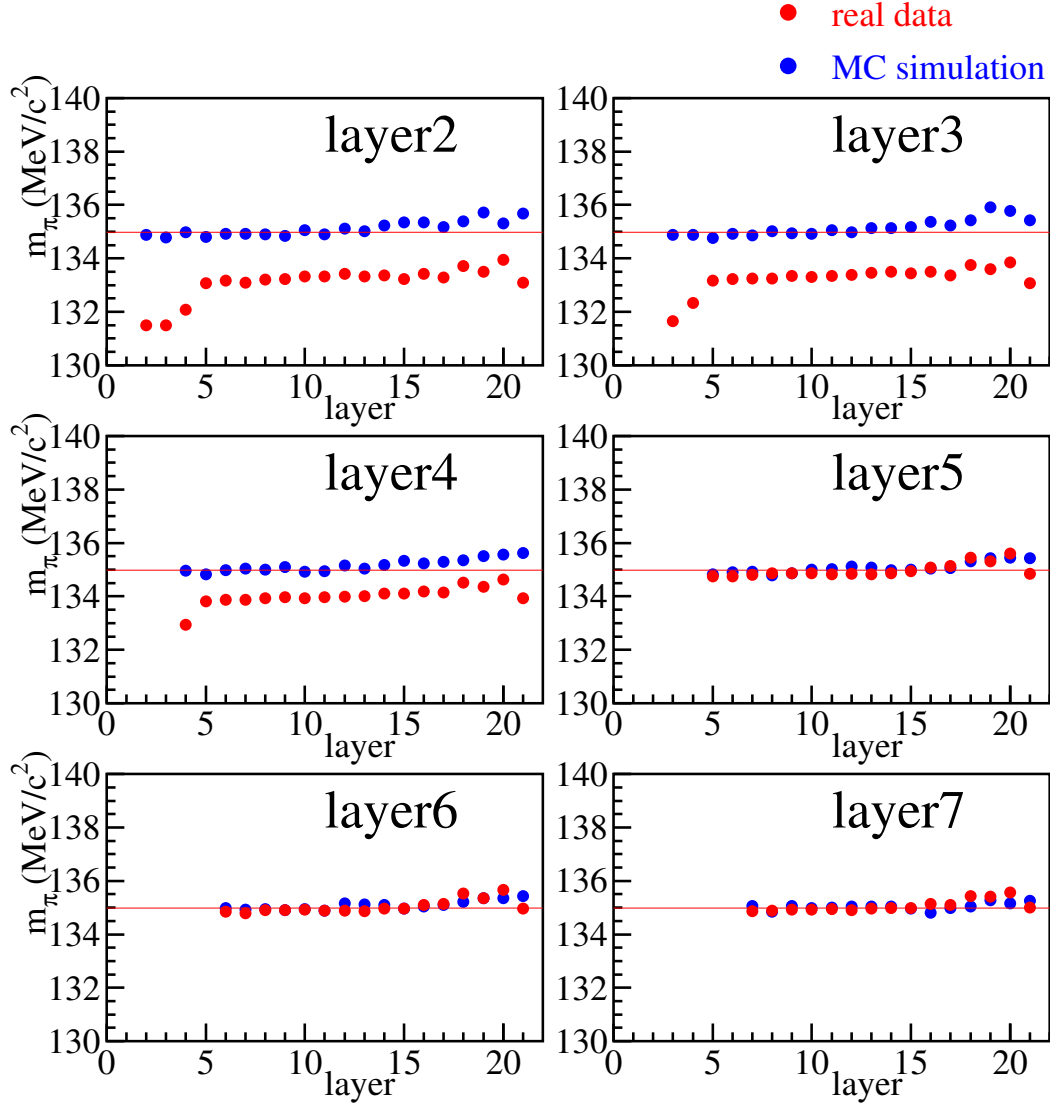


Figure 3.8: The reconstructed π^0 mass for different layer combinations of two neutral clusters in the case of using α^n . The layer number described in the upper side of each panel represents that of the forward cluster, and the horizontal axis represents the layer number of the backward cluster. The PDG value of π^0 mass is indicated by red lines. The forward layers up to the 7th layer are shown.

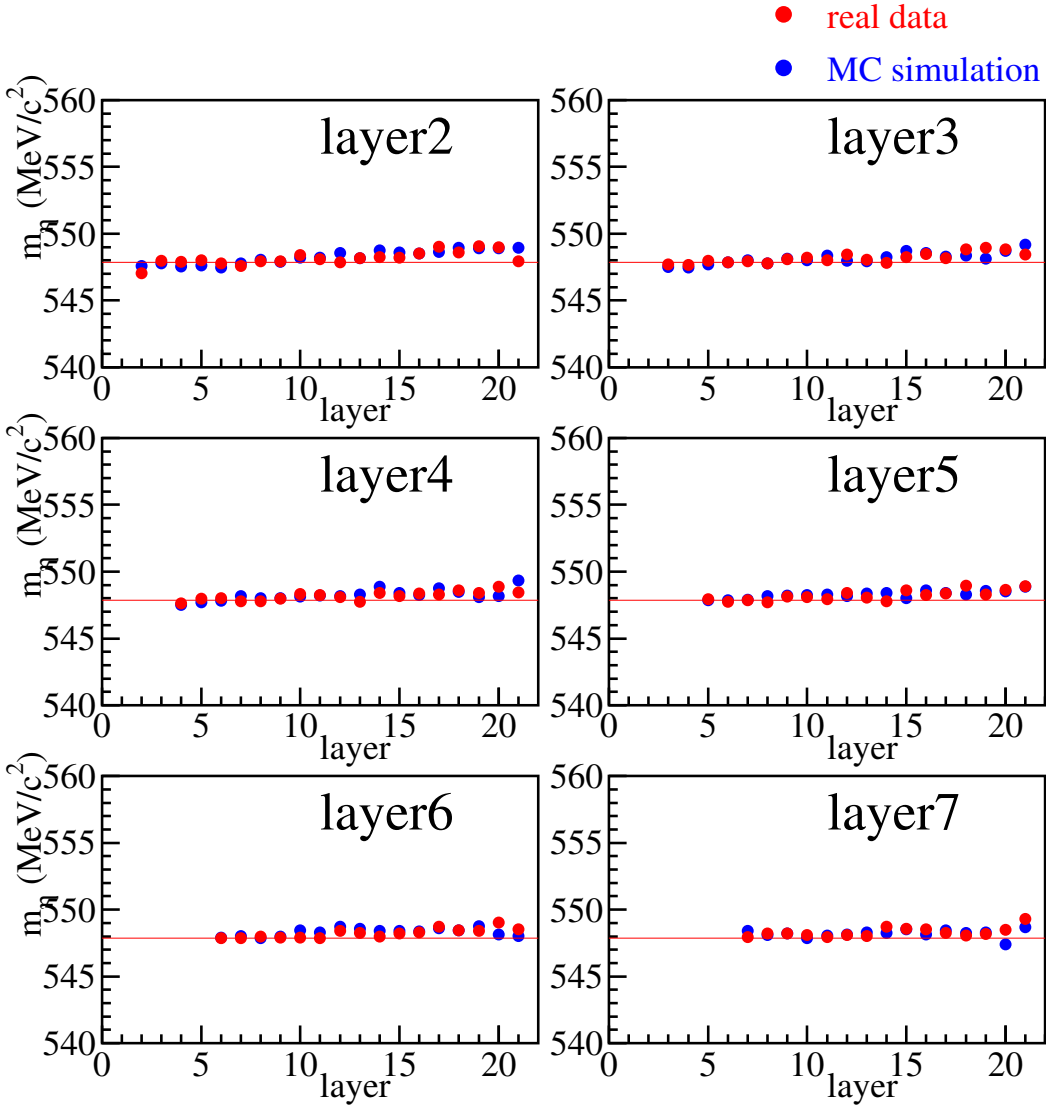


Figure 3.9: The reconstructed η mass for different layer combinations of two neutral clusters in the case of using α^η . The layer number described in the upper side of each panel represents that of the forward cluster, and the horizontal axis represents the layer number of the backward cluster. The PDG value of η mass is indicated by red lines. The forward layers up to the 7th layer are shown.

of H6524 is not perfect at low energies, affecting the gain calibration. Therefore, the cluster energies should be additionally corrected for the forward layers up to the 4th layer in order to remove the problem of gain factor inconsistency. Since H6524-type PMTs are used also for the backward two layers, the correction is applied to the 21st layer in the same way. The correction factors for the outermost layers (1st and 22nd layers) are not derived because a cluster whose core is found there is not used in the analysis described in the following chapters.

3.2.2 Correction of cluster energy for the forward layers

To correct the cluster energy with recovery of the linearity for the forward layers, the difference of the measured energy from the correct energy was estimated as a function of the true energy under the following assumptions:

1. The gain factors based on η mass, α^η , are determined incorrectly for the forward layers up to 4th when the photon energy is relatively low.
2. The cluster energies are correctly reconstructed for the inner layers from 6th to 19th with linearity.

The difference of a cluster energy from the correct energy for the forward layers, ΔE , were obtained in the following way. In the case of the correction for the i -th forward layer, π^0 mass was reconstructed in combination with another cluster detected at the j -th layer, where j varied from 6 to 19. The reconstructed π^0 mass M can be written by

$$M = 2\sqrt{E_i E_j} \sin \frac{\theta}{2}, \quad (3.15)$$

where E_i , E_j are the cluster energies with η -based gain factors α^η at the i -th and j -th layer, respectively, and θ is the opening angle of these clusters. Here, E_j must be a true energy, based on the assumption 2. The correct π^0 mass M_π is written by

$$M_\pi = 2\sqrt{E_i^{\text{true}} E_j} \sin \frac{\theta}{2}, \quad (3.16)$$

where E_i^{true} is a correct but unknown energy at the i -th layer. Then, the correction

factor $\Delta E = E_i^{\text{true}} - E_i$ can be derived to be

$$\frac{\Delta E}{E} = 1 - \left(\frac{M}{M_\pi} \right)^2. \quad (3.17)$$

In the measurement of $\Delta E/E$ by using Eq. 3.17, M was obtained from the two detected neutral clusters based on Eq. 3.15, while the PDG value of π^0 mass was assigned to M_π . The left panels of Figs. 3.10–3.12 show the obtained correction factor $\Delta E/E$ for the 2–4th layers. $\Delta E/E$ obtained by a MC simulation is also shown in the right panels of the same figures. There remains energy dependence of $\Delta E/E$ not only in the real data but also in the MC simulation. Here, photon energy distributions of individual crystals are enhanced at lower energy sides. In a certain E_i bin, event leaks due to a finite energy resolution exist more from the lower-energy neighboring bin with negative ΔE . This effect becomes stronger at higher-energy bins because higher-energy events are kinematically limited and the event leaks are more significant. Therefore, $\Delta E/E$ decreases at higher energies even in a MC simulation. The energy to be corrected is ΔE measured in the real data after removing this effect about event leakage. Thus, the true correction factor was obtained by subtracting the $\Delta E/E$ values of the MC simulation from that of the real data. Figure 3.13–15 show the $\Delta E/E$ results after the subtraction. Finally, the correction functions were determined by fitting a linear function to the subtracted data. The final cluster energy $E_{\text{cls}}^{\text{fin}}$ are obtained by adding the correction factor ΔE to the cluster energy after the leak correction, $E_{\text{cls}}^{\text{corr}}$: $E_{\text{cls}}^{\text{fin}} = E_{\text{cls}}^{\text{corr}} + \Delta E$. The corrections are applied for the energy ranges where $\Delta E > 0$.

After applying the $\Delta E/E$ correction, the gain factor calibrations to obtain α^π and α^η were redone. Then, the ratio of the gain factors α^π and α^η , the momentum dependence of η mass, and the layer dependence of π^0 mass were checked again. Figure 3.16 shows the new ratio of α^π/α^η . The inconsistency between α^π and α^η has been significantly resolved, and they agree within 1%. Figures 3.17 show the layer dependence of the π^0 mass. α^η 's were used to plot these figures. Strong dependences are removed, and the consistency with MC simulations has been achieved in both figures.

Although both types of gain factors α^π and α^η can be used consistently after applying the $\Delta E/E$ correction, α^π 's are used in the analysis described in the following

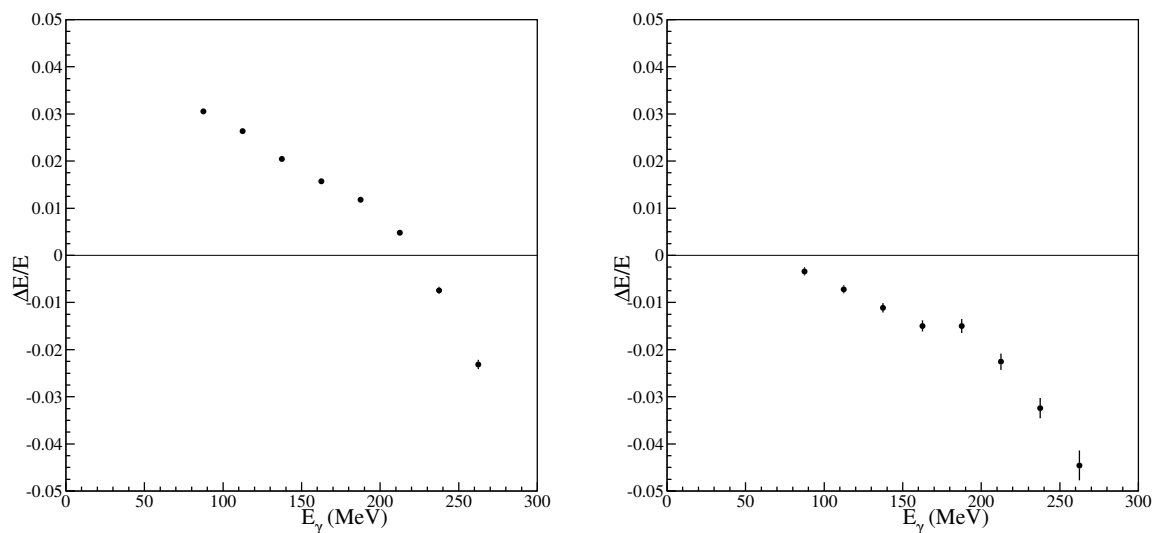


Figure 3.10: $\Delta E/E$ for the 2nd layer by using the real data (left) and a MC simulation (right).

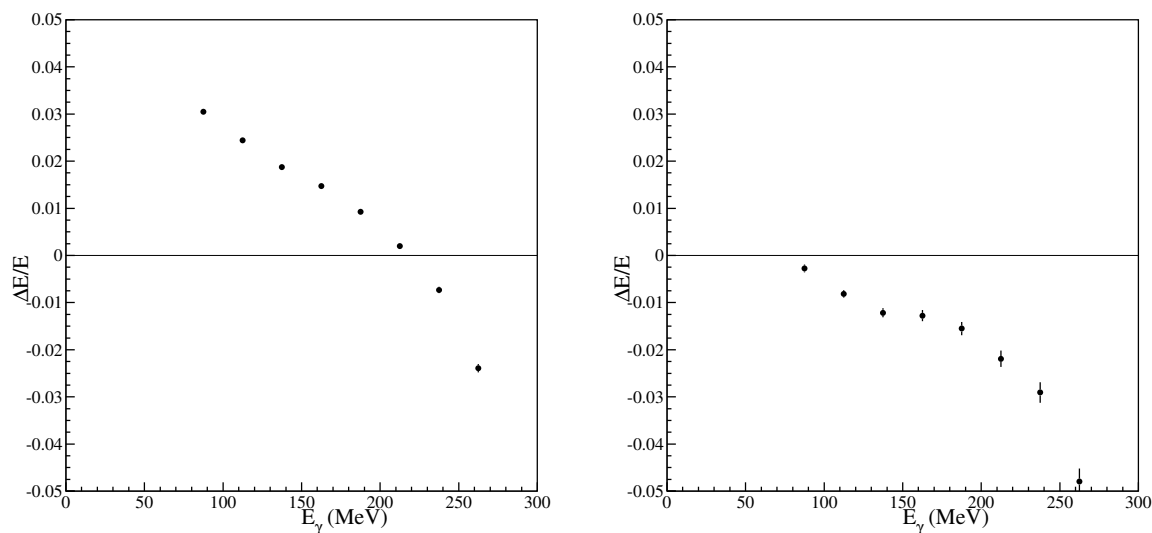


Figure 3.11: $\Delta E/E$ for the 3rd layer by using the real data (left) and a MC simulation (right).

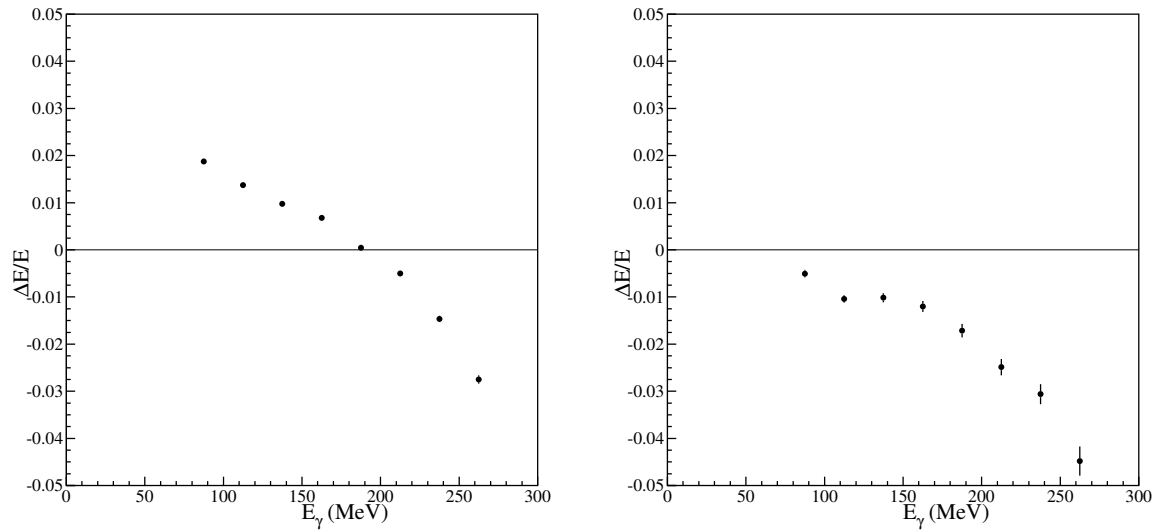


Figure 3.12: $\Delta E/E$ for the 4th layer by using the real data (left) and a MC simulation (right).

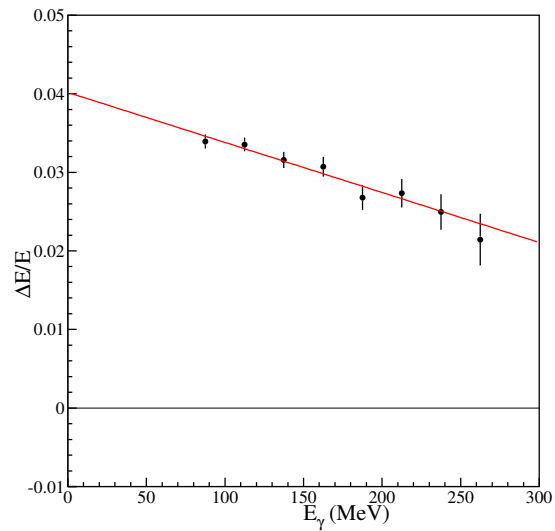


Figure 3.13: $\Delta E/E$ for the 2nd layer after subtracting the values by a MC simulation from those of the real data. A fitted function is indicated by a red line.

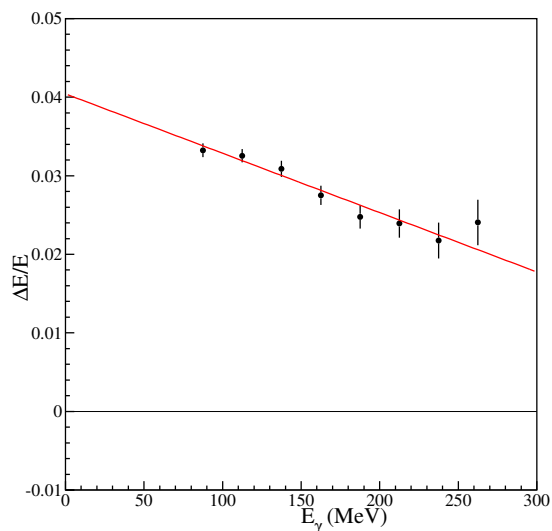


Figure 3.14: $\Delta E/E$ for the 3rd layer after subtracting the values by a MC simulation from those of the real data. A fitted function is indicated by a red line.

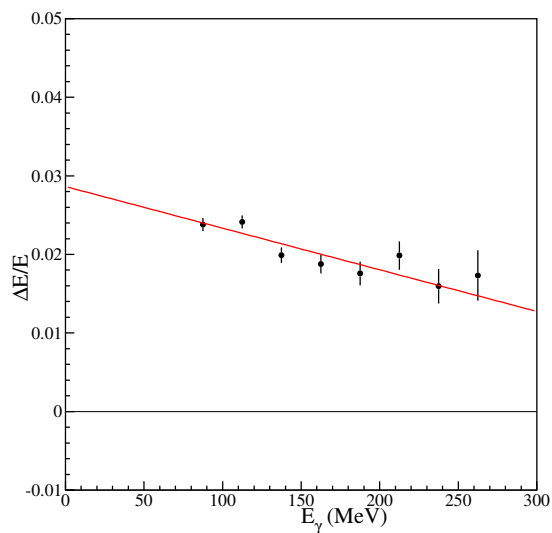


Figure 3.15: $\Delta E/E$ for the 4th layer after subtracting the values by a MC simulation from those of the real data. A fitted function is indicated by a red line.

chapters because α^π 's are stably determined with high statistics.

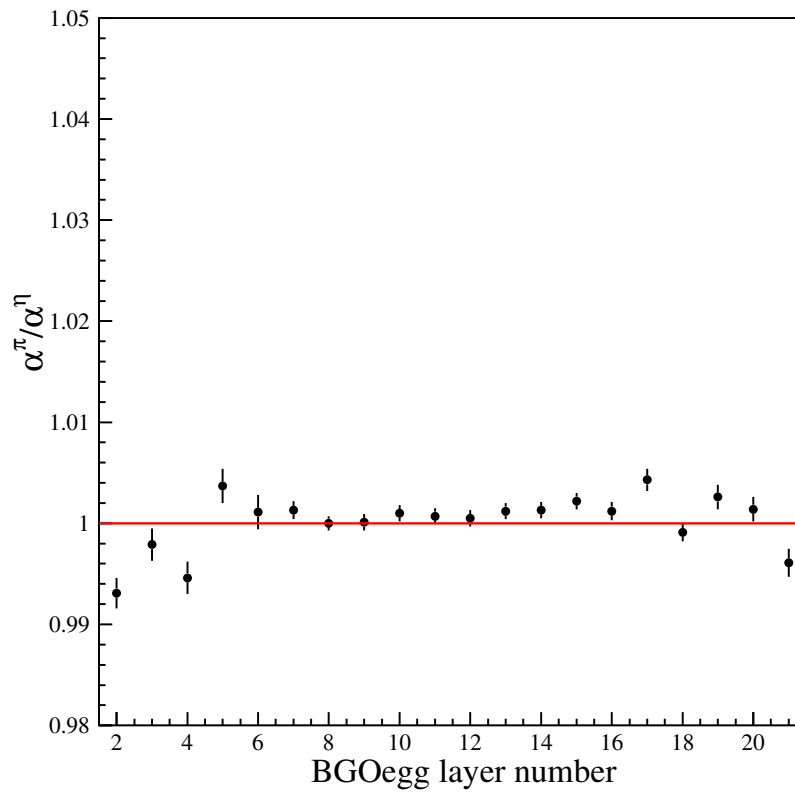


Figure 3.16: The ratio of the gain factors based on the π^0 and those based on the η mass (α^π/α^η) after applying the $\Delta E/E$ correction.

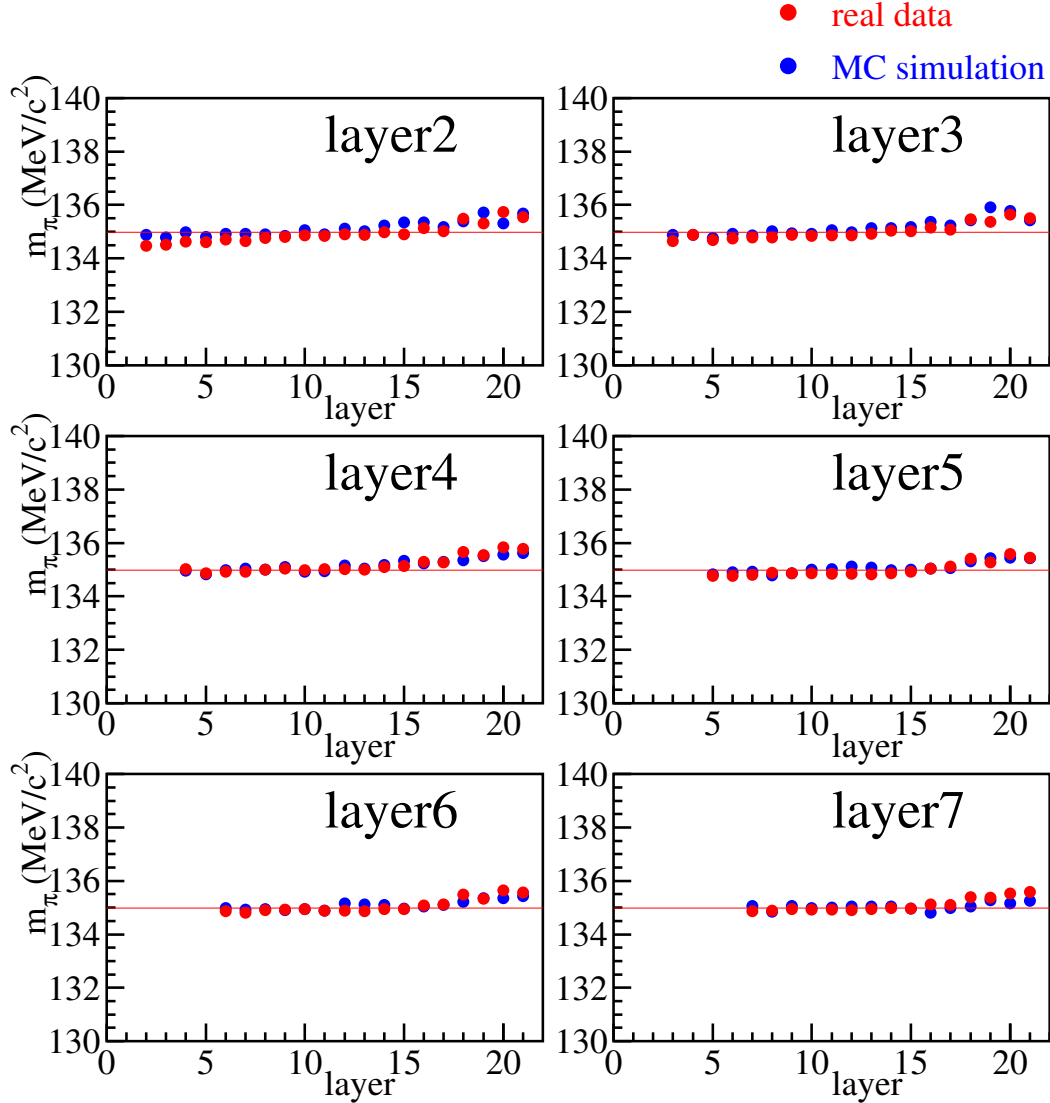


Figure 3.17: The reconstructed π^0 mass for different layer combinations of two neutral clusters after applying the $\Delta E/E$ correction. The layer number described in the upper side of each panel represents that of the forward cluster, and the horizontal axis represents the layer number of the backward cluster. The PDG value of the π^0 mass is indicated by red lines. The forward layers up to the 7th layer are shown.

Chapter 4

Event selection for η' analysis

In this chapter, event selection criteria for the $\eta' \rightarrow \gamma\gamma$ process and procedures for background reduction are described.

4.1 Fundamental event selection

The photoproduction process of η' mesons, i.e., $\gamma N \rightarrow \eta' N$ has been chosen as an elementary process to produce η' mesons in the nucleus. The mass spectrum of the η' meson was reconstructed using one of its decay channels, $\eta' \rightarrow \gamma\gamma$ mode, via detecting two photons in the final state. Therefore, the event with two photons and one nucleon in the final state will be selected for this analysis. Thus, events with just two neutral clusters and one or less charged clusters at BGOegg were selected. Note that nucleons are not necessarily detected because they can leave from the acceptance hole of BGOegg.

Fundamental cut conditions for the neutral clusters corresponding to photons are as follows:

1. The crystal energy sum of each cluster is more than 100 MeV.
2. Each cluster core does not belong to the outermost layers.
3. The angle between two neutral clusters is more than 50 degrees.

4. No crystal is shared by different clusters.
5. The occupancy ratio (the ratio of the energy deposit at the cluster core to the cluster energy) is less than 0.9.
6. The timing of each cluster with respect to the RF signal is within ± 1.5 ns.

The condition 1 was required to eliminate noise hits or incomplete clusters. The condition 2 was set because the energy resolution becomes too low at the outermost layers due to large energy leakage. The condition 3 was required because small opening angles bias the $\gamma\gamma$ invariant mass. (See Fig. 4.1.) The condition 5 was required in order to exclude a possibility of neutron hits. Since the energy deposit of photons spreads out due to an electro-magnetic shower, the occupancy ratio of clusters made by photons distributes in the range less than 0.9, as shown in Fig. 4.2. In contrast, the energy deposit of neutron clusters is concentrated at the cluster core. The condition 6 was determined so that the timing range should be set within $\pm 5\sigma$ for all layers and cluster energies. This timing condition can reduce accidental BGOegg hits from different electron bunches and clusters made by cosmic rays. Slow neutrons can be also excluded by this timing condition.

When a charged cluster is found at BGOegg, it should correspond to a proton. Thus, a condition to identify the proton was required using so-called ΔE - E correlation, where ΔE is the energy deposit measured by the inner hodoscopes, E_{IPS} , and E is the cluster energy measured by BGOegg, $E_{\text{cls}}^{\text{fin}}$. Figure 4.3 shows the ΔE - E correlation along with the selected region between red lines. Events with two neutral clusters were selected to plot the figure, where the $\gamma\gamma$ invariant mass $M_{\gamma\gamma}$ was required to be in the region of $900 \leq M_{\gamma\gamma} < 1020$ MeV. The selected region is expressed by

$$0.339 + 232.9/E_{\text{cls}}^{\text{fin}} \leq E_{\text{IPS}} < 1.326 + 353.6/E_{\text{cls}}^{\text{fin}}, \quad (4.1)$$

where $E_{\text{cls}}^{\text{fin}}$ is measured in the unit of MeV, and E_{IPS} is measured in the unit normalized by the energy deposit of minimum ionizing particles (MIP). The inner hodoscopes were calibrated so that the distribution of energy deposits by MIP should be peaked at 1.

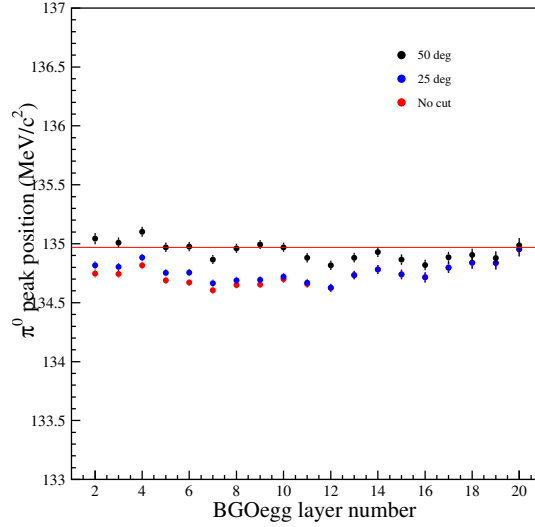


Figure 4.1: π^0 peak positions in the $\gamma\gamma$ invariant mass distribution for each layer in a MC simulation of $\gamma p \rightarrow \pi^0 \eta p$ events. Opening angle cuts were applied with the cut points of 50 degrees (black) and 25 degrees (blue). No cut was applied for the red points. The PDG value of the π^0 mass is indicated by a red line. The $\gamma\gamma$ invariant mass is biased in forward layers in the case of 25-degrees cut or no cut.

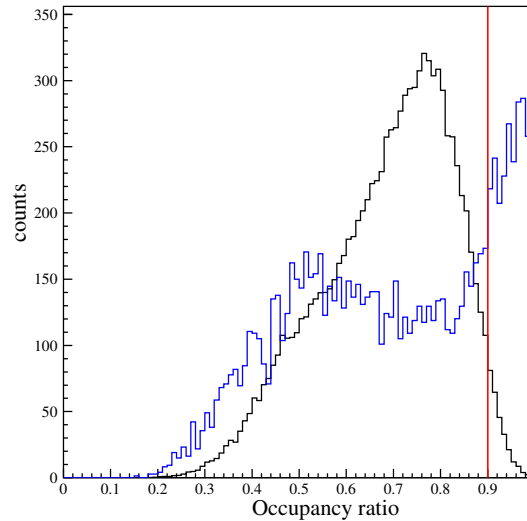


Figure 4.2: Distributions of the occupancy ratio of a cluster for photon hits (black) and neutron hits (blue). The cut point is indicated by a red line at 0.9.

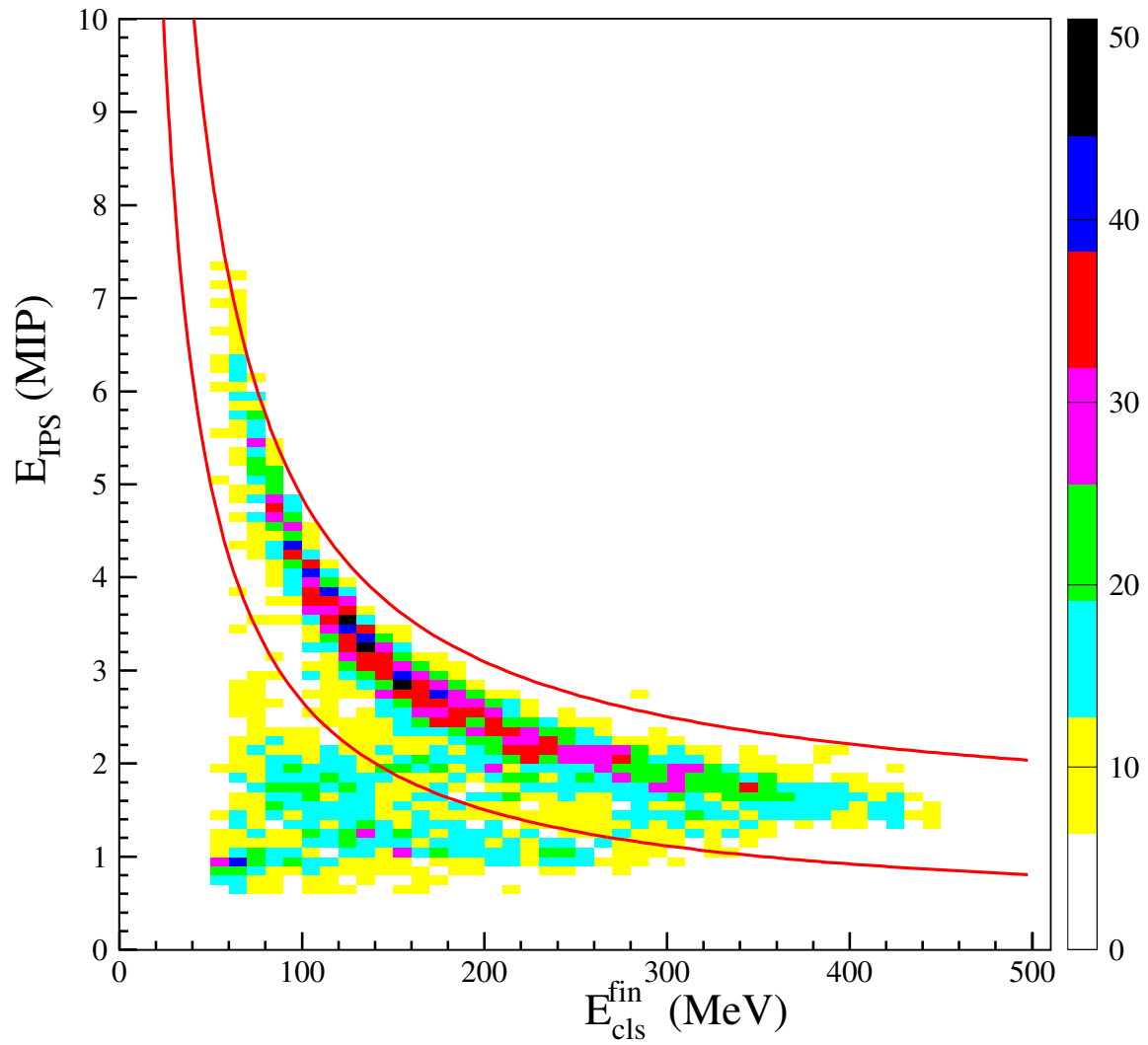


Figure 4.3: ΔE - E correlation for events with $900 \leq M_{\gamma\gamma} < 1020 \text{ MeV}/c^2$. Protons were selected in the region between the two red lines.

4.2 Background reduction criteria

Even after the fundamental event selection described in the above section, a lot of background events remain in the $\gamma\gamma$ invariant mass spectrum. Main background events come from wrong combinations of $\gamma\gamma$ pairs, which originated from the dominantly produced events with the energy region, i.e., $2\pi^0$ production events, with missing two photons. Moreover, photons emitted with small opening angles could be recognized as a large cluster, which also causes background events. In particular, π^0 mesons with large momenta may generate such combined clusters events. In addition, there are a lot of “unphysical clusters”, which are generated by particles coming from other places than the target. A significant amount of charged particles comes from the upstream of BGOegg, and some of them are identified as neutral clusters, mainly at backward layers. Note that even charged particles are recognized as “neutral” clusters because these particles may not hit inner hodoscopes. Background events caused by these processes can be distinguished by checking the cluster shape. Here techniques developed for background reduction are described.

4.2.1 Cluster radius

The combined clusters can be distinguished by the effective cluster radius R_{cls} . It is defined by

$$R_{\text{cls}} = \sum_i |\vec{r}_i - \vec{r}_{\text{cls}}| \frac{E_i}{E_{\text{cls}}^{\text{fin}}}, \quad (4.2)$$

where \vec{r}_i , E_i are the position and energy of the i -th crystal of the cluster, and \vec{r}_{cls} , $E_{\text{cls}}^{\text{fin}}$ are the position and energy of the cluster, respectively.

Figure 4.4 shows the distribution of R_{cls} for $\eta' \rightarrow \gamma\gamma$ events (left) and $\pi^0\pi^0 \rightarrow 4\gamma$ events (right) generated by a MC simulation. The R_{cls} represents the effective radius of an electro-magnetic shower developed in the calorimeter. The R_{cls} is independent of the cluster energy, which is clearly shown as the peak structure around $R_{\text{cls}} \approx 10$ mm, and extended to $R_{\text{cls}} \approx 18$ mm in Fig. 4.4 left and right. The second peak structure in the right panel of Fig. 4.4 is generated by combining two or more photons that make hits close to each other.

Figure 4.5 shows the R_{cls} distribution as a function of the BGOegg layer number in the real data. As discussed in Fig. 4.4, clear separation between the normal cluster

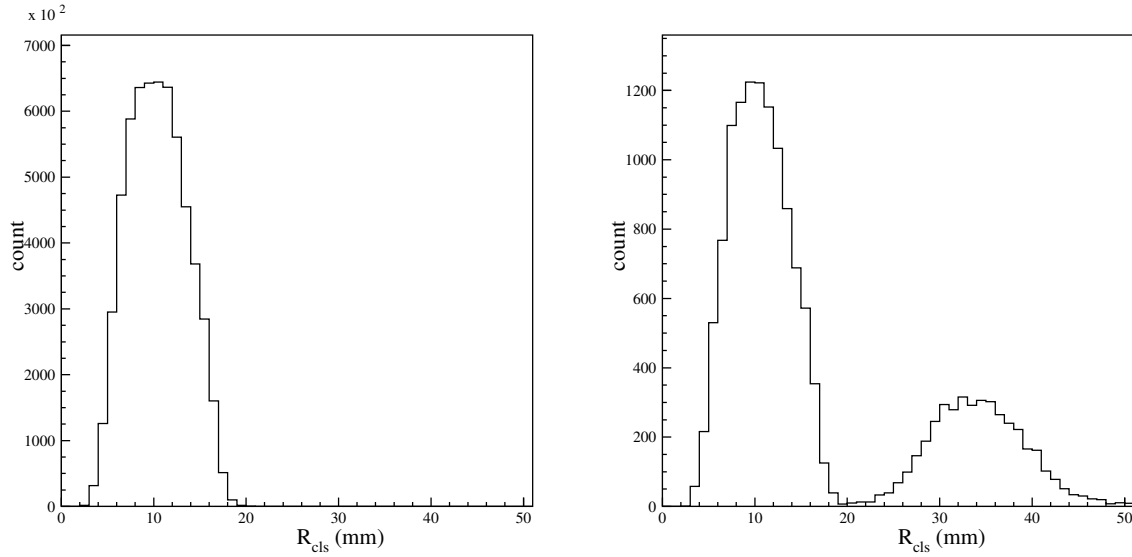


Figure 4.4: The simulated R_{cls} distributions for the processes $\eta' \rightarrow \gamma\gamma$ (left) and $\pi^0\pi^0 \rightarrow 4\gamma$ (right).

and the combined cluster is seen in the figure. In addition, another structure has been seen in the figure, which is not originated from physical events such as charged particles coming from upstream. The cut point was set to 18 mm for the layers 2-18, 15 mm for the layer 19, 12 mm for the layer 20, and 9 mm for the layer 21. Tighter conditions were applied for backward layers because a lot of large R_{cls} clusters exist. Moreover, R_{cls} of unphysical clusters becomes smaller as the layer of a cluster core is more backward. Figures 4.6 and 4.7 show the R_{cls} distributions of the real data and MC simulations for each layer, respectively. Clusters with R_{cls} larger than the cut points, indicated by red lines, were eliminated.

Figure 4.8 shows the $\gamma\gamma$ invariant mass spectrum obtained with and without this cut for the real data. The R_{cls} -cut works well especially in the high-mass region, where high momentum pions decaying to $\gamma\gamma$ with small opening angles tend to form combined clusters. No structure has been found around the η' mass region in the $\gamma\gamma$ invariant mass spectrum for the events rejected by this cut.

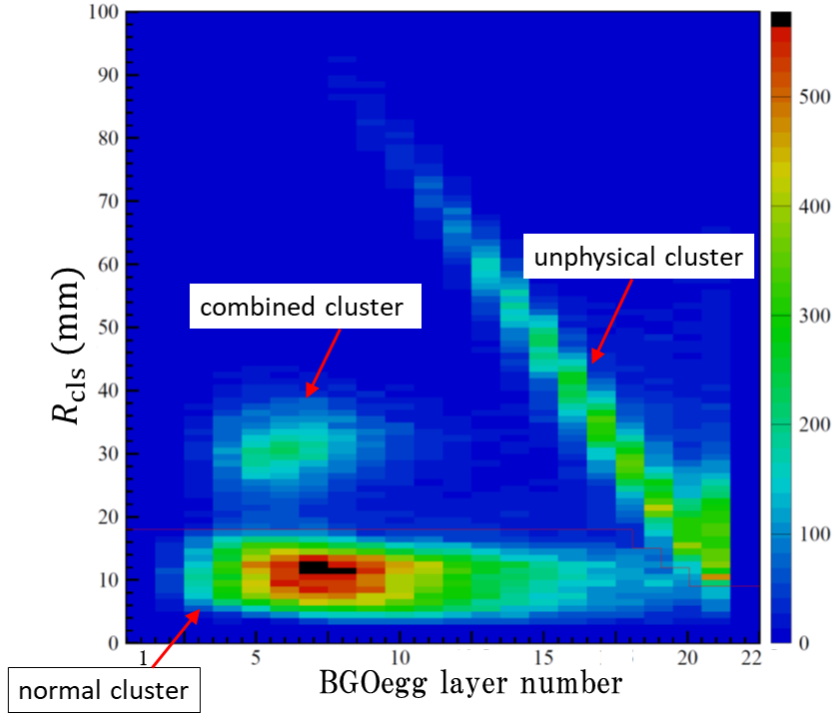


Figure 4.5: Layer number dependence of R_{cls} distribution in the real data. In horizontal axis, a larger number corresponds to a more backward layer of the BGOegg calorimeter. Normal clusters are distributed in $R_{\text{cls}} \leq 18$ mm, while combined clusters are distributed around $R_{\text{cls}} \sim 30$ mm. Unphysical clusters, distributing mainly at backward layers, have large values of R_{cls} .

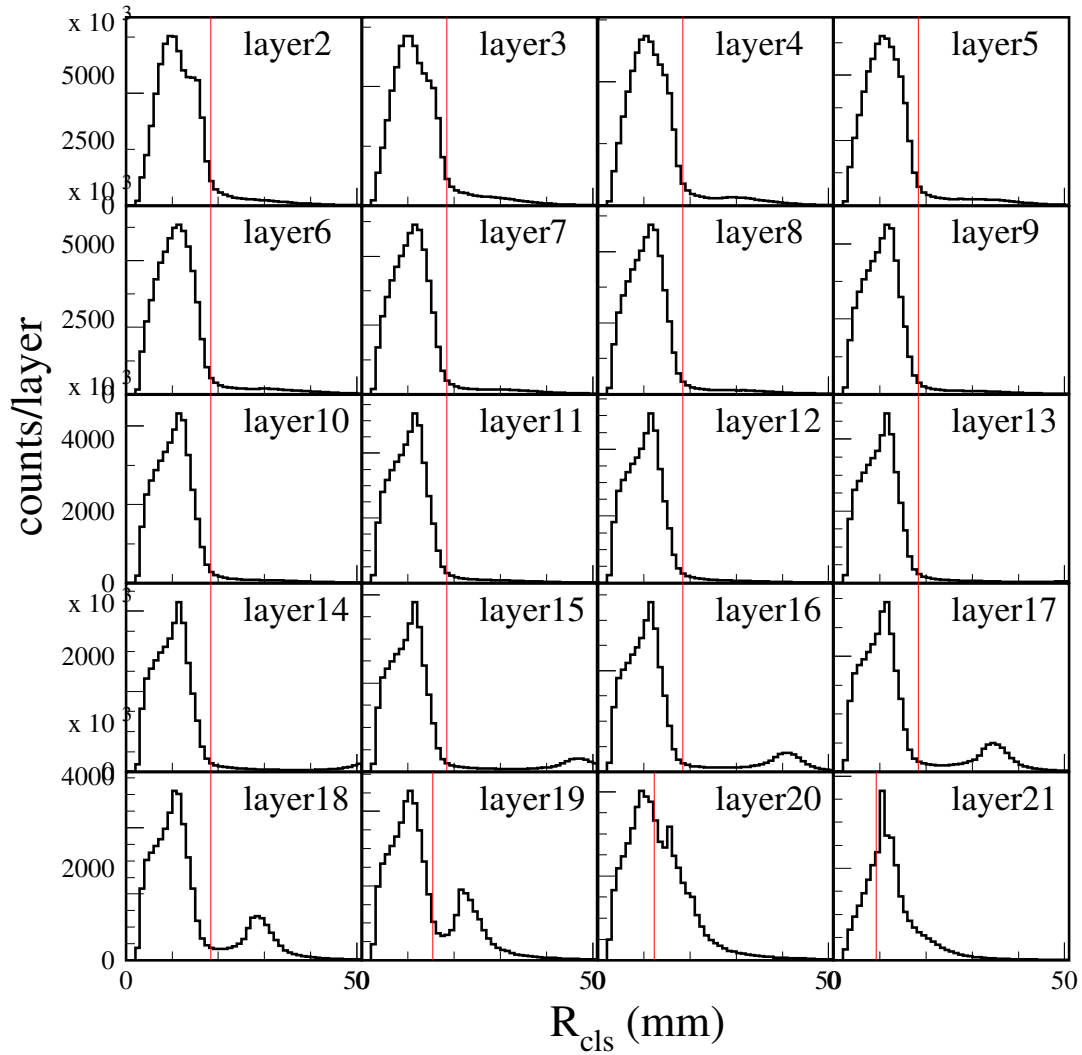


Figure 4.6: R_{cls} distributions in the real data. The cut points are shown by red lines. The events above the cut points are eliminated.

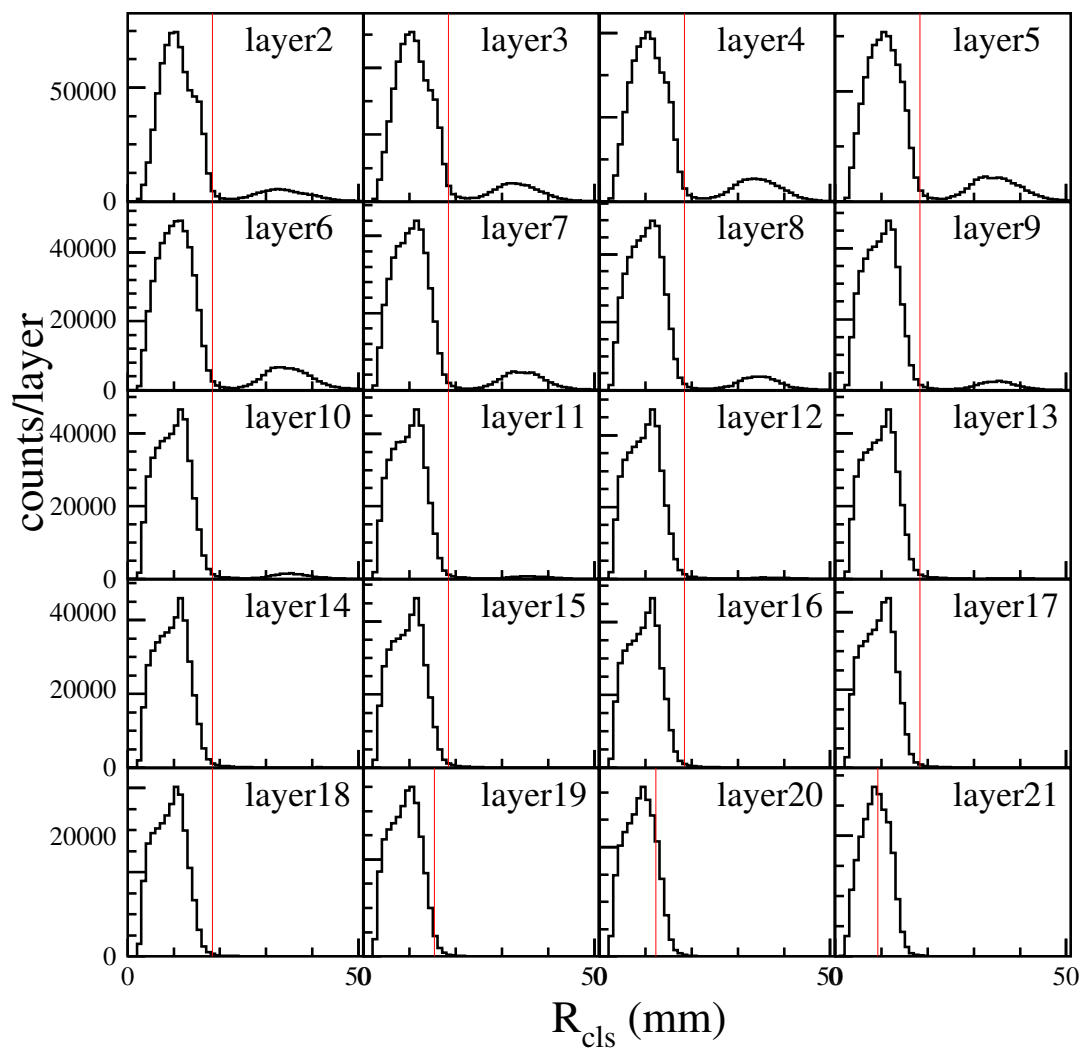


Figure 4.7: R_{cls} distributions in the MC simulation of $\pi^0\pi^0 \rightarrow 4\gamma$ events. The cut points are shown by red lines. The events above the cut points are eliminated.

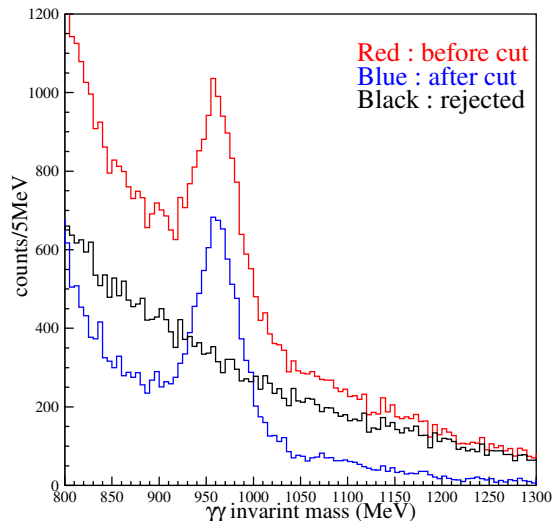


Figure 4.8: The $\gamma\gamma$ invariant mass distribution before (red) and after (blue) applying the cluster radius cut. The black histogram shows the distribution for rejected events.

4.2.2 Cluster shape

Although the cut using the effective cluster radius, described in the above subsection, is effective for unphysical clusters, some of them still remain after the cut. These events can be reduced by using an asymmetry factor of the cluster shape A_{cls} , defined by

$$A_{\text{cls}} = \frac{E_f + E_b - E_+ - E_-}{E_f + E_b + E_+ + E_-}, \quad (4.3)$$

where E_f and E_b are the energy deposits in forward and backward adjacent crystals of the cluster core, respectively. E_+ and E_- are the energy deposits of adjacent crystals of the cluster core in the azimuthal direction. (See Fig. 4.9.) Eq. 4.3 represents a cluster shape, that is, A_{cls} is close to 1 when a cluster is expanded in the polar angle direction θ , and -1 when it is expanded in the azimuthal direction ϕ . A_{cls} becomes 0 when the cluster shape is symmetric. If a cluster is generated by a particle from the target, the cluster shape must be symmetric and A_{cls} therefore distributes around 0. Figures 4.10 and 4.11 show the A_{cls} distributions in the real data and the $\eta' \rightarrow \gamma\gamma$ simulation, respectively. There are a lot of events around $A_{\text{cls}} = \pm 1$ in the real data, while fewer events exist around $A = \pm 1$ in the corresponding regions for the

simulation. The cut points were shown by red lines for each layer in the figures, and the clusters outside the lines were eliminated.

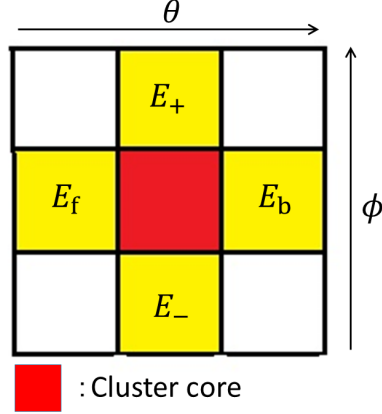


Figure 4.9: The definition of the asymmetry factor A_{cls} of a cluster. E_f and E_b are the energy deposits of adjacent crystals of the cluster core in polar (θ) direction. E_+ and E_- are the energy deposits of adjacent crystals of the cluster core in azimuthal (ϕ) direction. The cluster core is shown by the red block.

4.3 Final $\eta' \rightarrow \gamma\gamma$ spectrum

As a result of the BGOegg calibration and background reduction, the η' peak has been clearly observed in the $\gamma\gamma$ invariant mass spectrum. Figure 4.12 shows the final $\eta' \rightarrow \gamma\gamma$ spectrum. A linear combination of a Gaussian function and a 2nd-order polynomial function were fitted to the spectrum. The fitted function is also shown in Fig. 4.12 by a red line. The η' mass resolution was achieved to be $20.7 \text{ MeV}/c^2$. The η' yield was estimated to be approximately 1.6×10^4 from integration of the fitted Gaussian function.

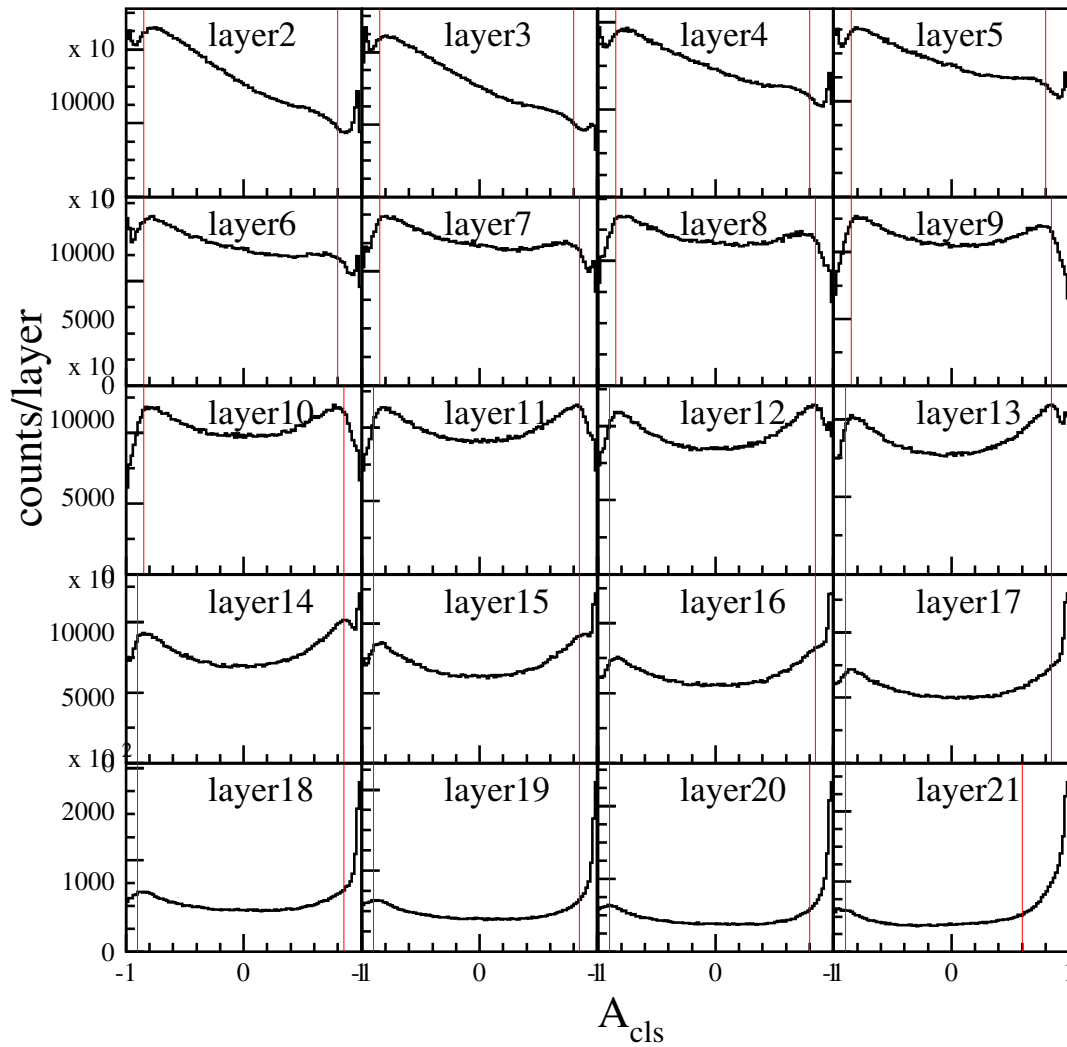


Figure 4.10: The A_{cls} distributions in the real data. The cut points are shown by red lines. Events outside the red lines are eliminated.

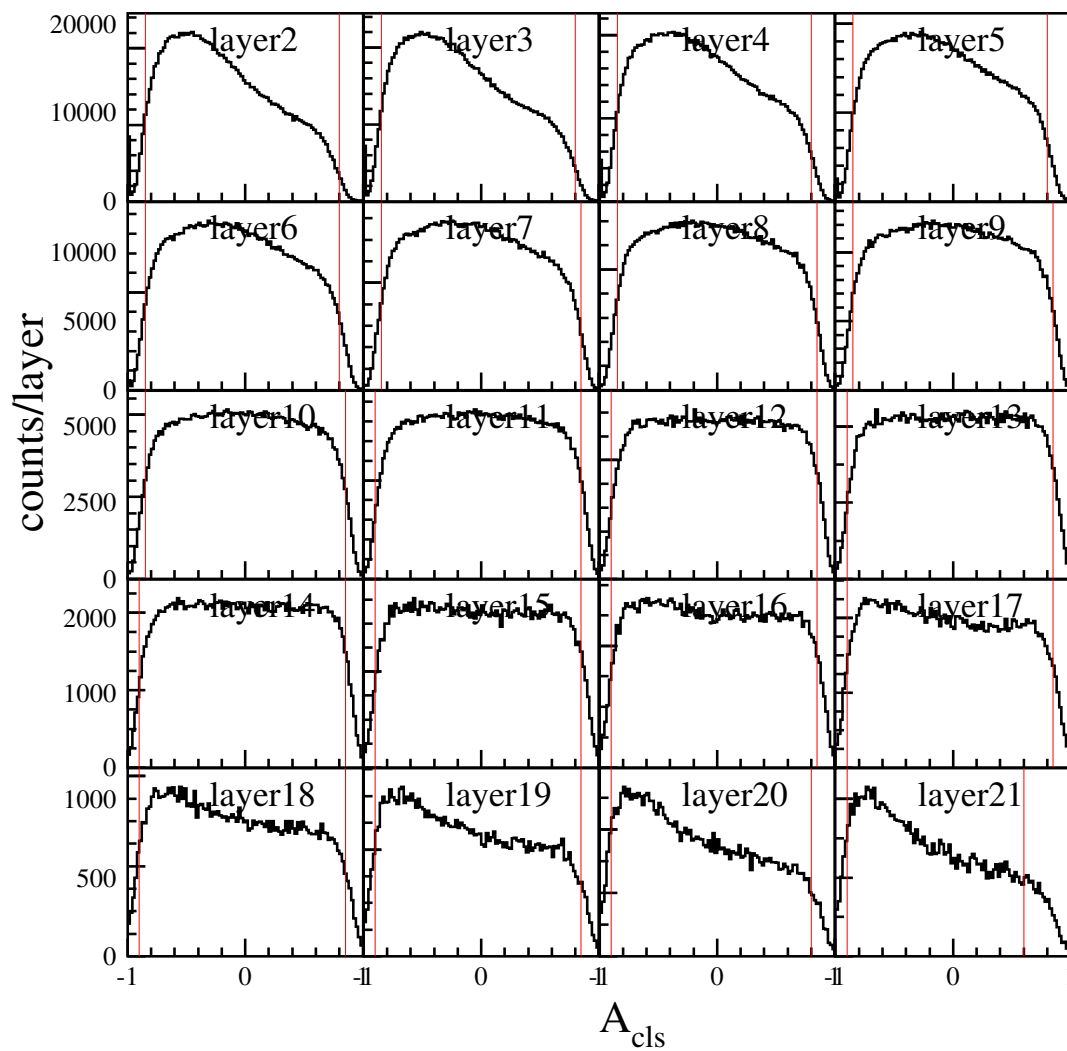


Figure 4.11: The A_{cls} distributions in the $\eta' \rightarrow \gamma\gamma$ simulation. The cut points are shown by red lines. Events outside the red lines are eliminated.

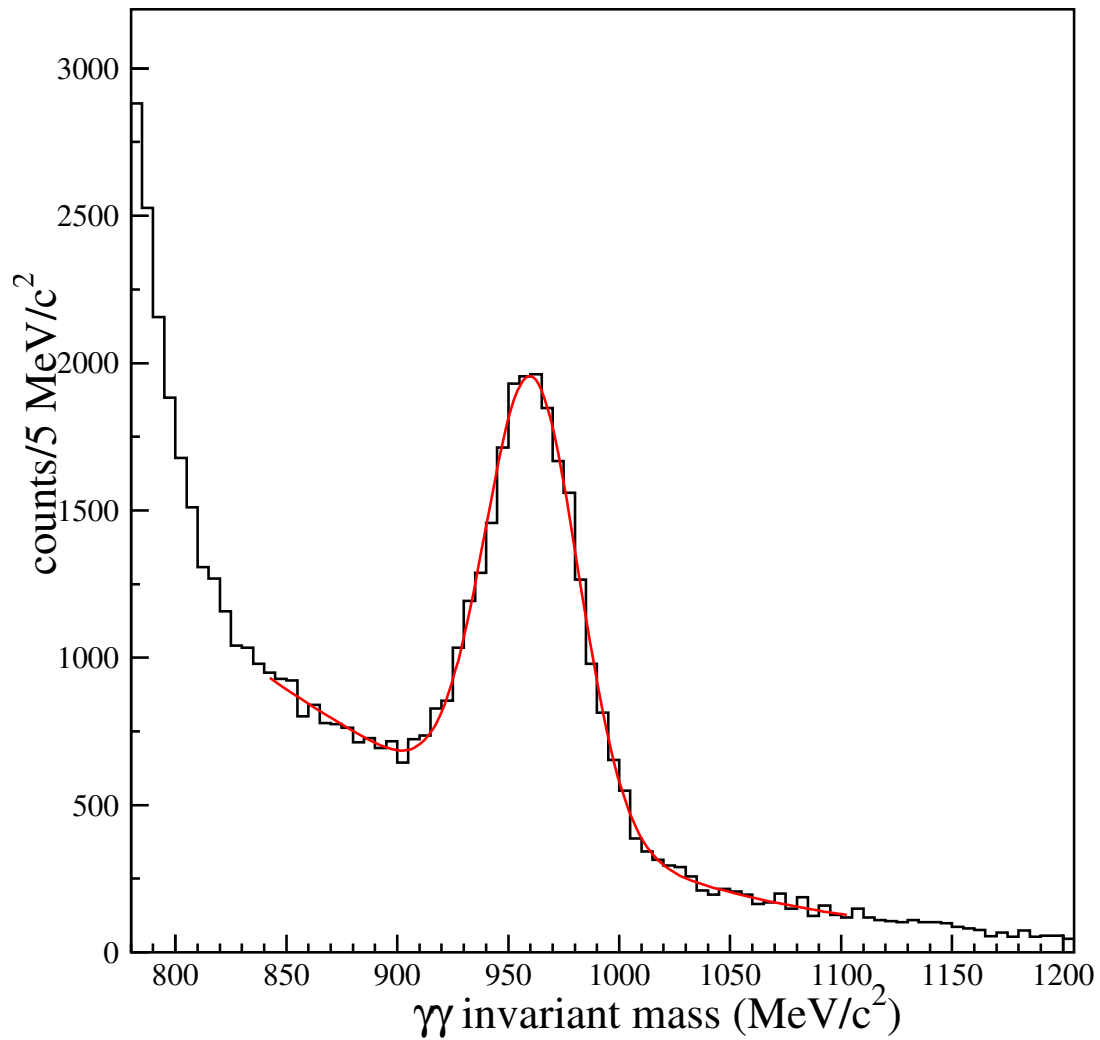


Figure 4.12: The final spectrum for $\eta' \rightarrow \gamma\gamma$ events after applying all the selection cuts. The fitted function is shown by a red line.

Chapter 5

Line shape analysis

To search for the modification of the in-medium η' mass spectrum, the deviation of the $\gamma\gamma$ invariant mass distribution from the quasi-free η' mass spectrum was investigated by fitting realistic spectral functions to the measured spectrum. In this chapter, the spectral line shape of $\gamma\gamma$ invariant mass is discussed.

5.1 Outline of the line shape analysis

As shown in Fig. 5.1, the measured $\gamma\gamma$ invariant mass spectrum around η' mass region consists of quasi-free η' photoproduction, background events originated from ω production processes, and other background processes such as multi-meson productions. If the sum of the spectral functions representing these components are well fitted to the measured mass spectrum, then the spectrum can be completely explained by these sources alone, otherwise we would recognize that there are unknown components in the spectrum. For the present analysis, it is important to reliably determine spectral functions of individual components to be fitted. In the following sections, how to fix the spectral shapes of each component in the $\gamma\gamma$ invariant mass distribution is discussed. The systematics checks for the spectral functions are intensively performed. In Sec. 5.2, a MC simulation is prepared to evaluate the $\gamma\gamma$ invariant mass distribution of each component. The spectral shapes of individual components are discussed in Sec. 5.3. Finally, results of the fitting of the prepared spectral functions to the

measured spectrum is shown in Sec. 5.4.

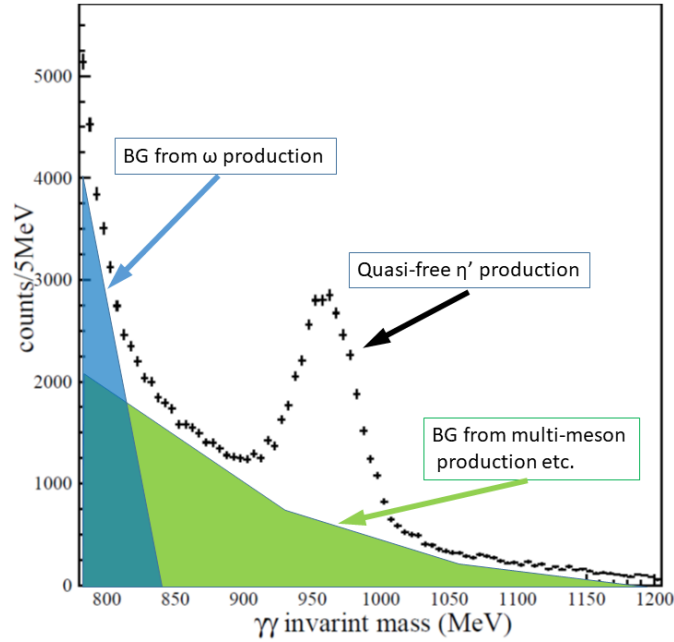


Figure 5.1: The schematic drawing of the components in the $\gamma\gamma$ invariant mass spectrum.

5.2 Simulation for background events

A MC simulation based on GEANT4 was performed to study background spectra. Simulation conditions are summarized as below.

1. The energies of incident beam photons were distributed according to a spectrum of inverse Compton scattering in a energy range of $1.4 \leq E_\gamma < 2.4$ GeV.
2. The target was set to be a proton. The momenta of target protons were generated according to Fermi motion based on the harmonic oscillator model for a carbon target.
3. For the simulations of $\gamma p \rightarrow \eta' p$, $\gamma p \rightarrow \eta p$, and $\gamma p \rightarrow \omega p$, the distributions of photoproduced particles were made to follow the differential cross section of each process based on Refs. [44, 45]. For other processes, such as multi-meson

production, reaction products were generated isotropically in the center-of-mass frame.

4. Reaction vertices were generated according to the energy-dependent beam shapes, described in Section 5.2.1, for the x and y direction. The vertices in the z direction were made uniform over the length of a target.

5.2.1 Energy-dependent beam shape

The x and y distributions of reaction vertices were determined based on the energy-dependent beam shape. The photon emission angle θ_γ in the inverse Compton scattering is given by

$$\theta_\gamma^2 = \frac{1}{P_e^2} \left(\frac{4E_0P_e^2}{E_\gamma} - 4E_0P_e - m_e^2 \right), \quad (5.1)$$

where P_e , E_0 , and m_e are the momentum of an electron in the storage ring, the energy of a laser photon injected onto the electron beam, and the electron mass, respectively. The radius from the beam center in the x - y plane is given by $\theta_\gamma L$, where L corresponds to 125 m representing the distance from the collision point of inverse Compton scattering to the target position. The direction of incident photons was smeared by the divergence of the electron beam $(\sigma_{x'}, \sigma_{y'}) = (12 \mu \text{ rad}, 1 \mu \text{ rad})$. The polarization effect on the beam shape was neglected. The beam center was set to the measured value $(-0.75 \text{ mm}, 2.33 \text{ mm})$. Figure 5.2 shows the simulated reaction vertex distributions in the x - y plane for individual beam energies.

5.2.2 Mass resolution

In the line shape analysis, the quasi-free η' distribution is represented by a Gaussian function with a fixed width based on the mass resolution. To evaluate the η' mass resolution, a MC simulation was performed after confirming that the simulation can reproduce the experimental mass resolution correctly by using the reactions other than the η' photoproduction. Two processes, $\gamma p \rightarrow \eta p$ and $\gamma p \rightarrow \omega p$, were used to check the validity of evaluated mass resolutions. Figure 5.3 shows the comparison of the mass resolutions between the real data and the MC simulation. The left panel shows the $\eta \rightarrow \gamma\gamma$ case and the right panel shows the $\omega \rightarrow 3\gamma$ case. The mass resolution in the MC simulation well reproduces the real data in both cases.

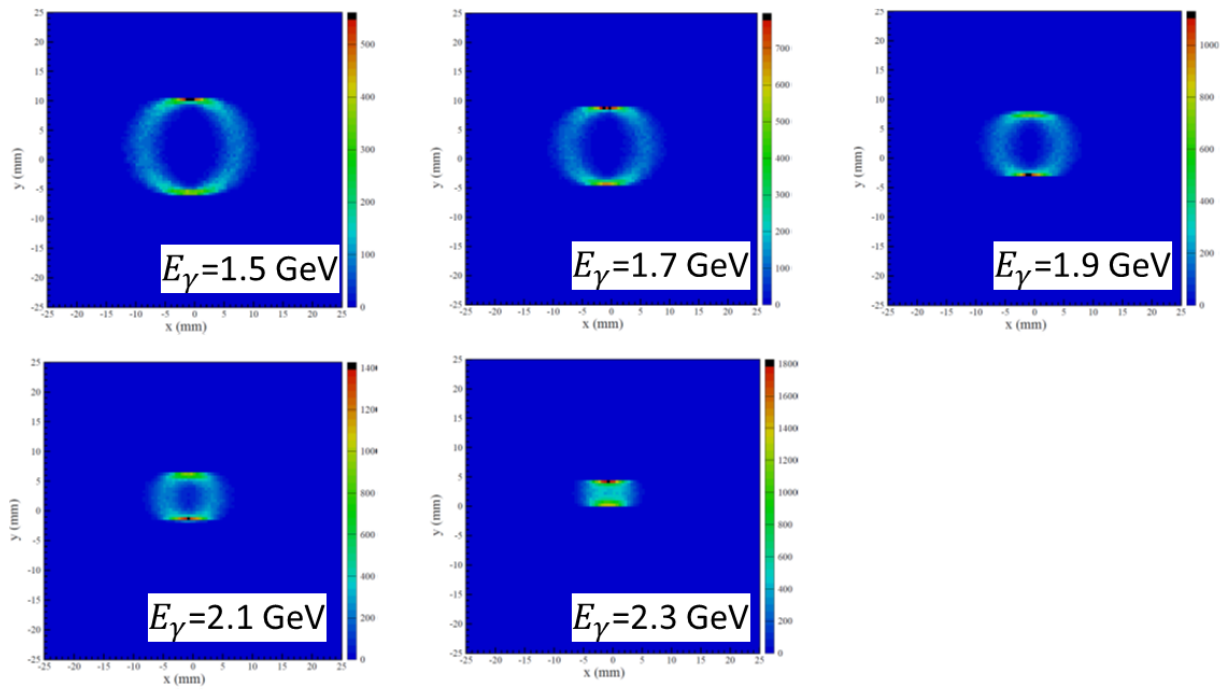


Figure 5.2: The reaction vertex distributions in the xy plane for individual beam energies in the MC simulation.

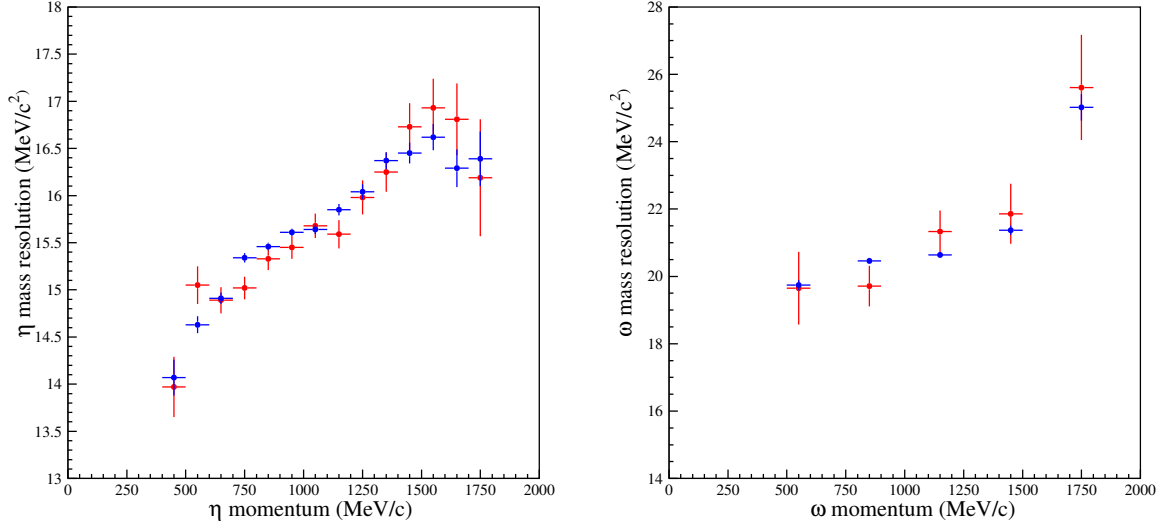


Figure 5.3: The mass resolutions of η (left) and ω (right). The red and the blue points represent the real data and the MC simulation, respectively.

5.3 Mass spectra of background processes

The background distribution in the $\gamma\gamma$ invariant mass spectrum around the η' mass is assumed to be a sum of the quasi-free η' peak, the background originated from ω photoproduction, and other processes including multi-meson photoproduction, as shown in Fig. 5.1. The treatment of each background source in the line shape analysis is described in this section.

5.3.1 Quasi-free η' peak

The quasi-free η' peak in the $\gamma\gamma$ invariant mass spectrum is expressed by a Gaussian function with a fixed width $\sigma_{\eta'}$, which denotes a convolution of the mass resolution and the η' natural width ($\Gamma_{\eta'} = 0.197$ MeV). The mass resolution was evaluated by a MC simulation of $\gamma p \rightarrow \eta' p$ process depending on the momentum of $\gamma\gamma$ system $P_{\gamma\gamma}$, as explained in Sec. 5.2.2. Figure 5.4 shows the evaluated η' mass resolutions.

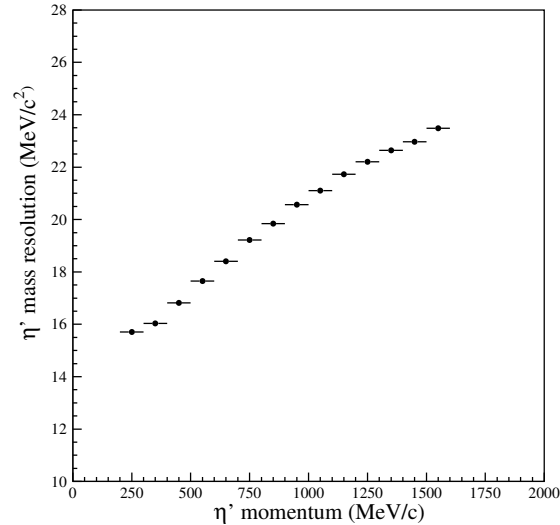


Figure 5.4: The momentum dependence of η' mass resolution evaluated by the MC simulation.

5.3.2 Background from ω mesons

In the $\gamma\gamma$ invariant mass spectrum, tail structure starting from 780 MeV/c² has been observed. This is originated from $\omega \rightarrow \pi^0\gamma \rightarrow \gamma\gamma\gamma$ process, where one of γ 's from the π^0 decay is missing. Since the peak has a tail up to around the η' mass, this process should be considered as a background source in the spectrum fit. The background distribution from the $\gamma p \rightarrow \omega p \rightarrow \gamma\gamma\gamma$ process was simulated depending on the momentum of a $\gamma\gamma$ system. Figure 5.5 shows the simulated distributions from ω meson decays around the η' mass.

5.3.3 Multi-meson background

In this analysis, the multi-meson production is a major and significant background source, where three or more photons are emitted and wrong combinations of $\gamma\gamma$ can be made. In this subsection, the absolute strengths of individual contributions of possible process are discussed along with their treatment in the fit to a $\gamma\gamma$ invariant mass spectrum. An appropriate function was eventually defined to represent all of multi-meson backgrounds.

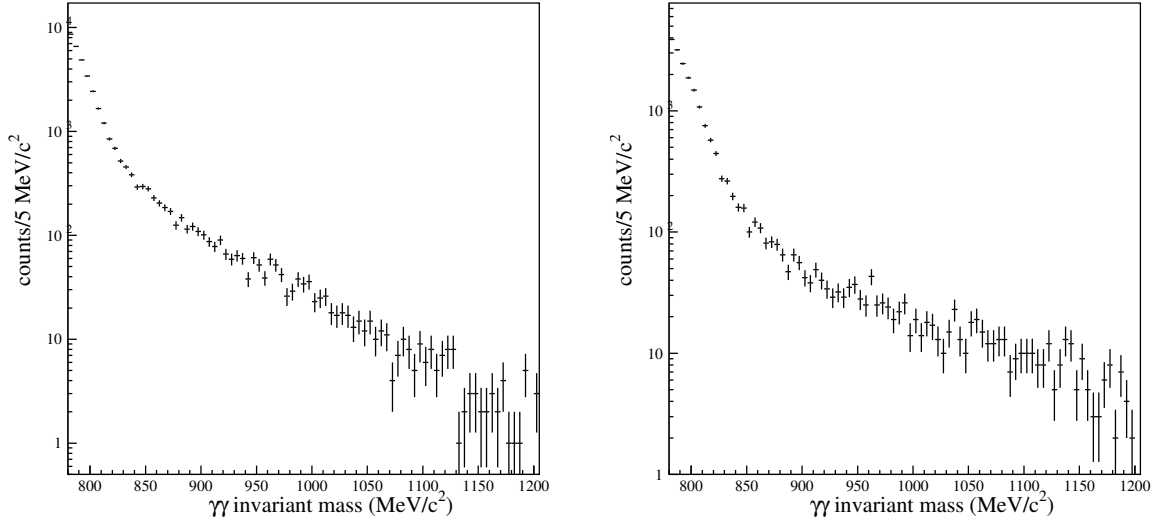


Figure 5.5: The simulated distributions from $\omega \rightarrow \pi^0\gamma$ decays. The left and right panels show the events with $\gamma\gamma$ momentum below and above 1000 MeV/c, respectively.

$\gamma p \rightarrow \pi^0\pi^0 p$ process

The $2\pi^0$ production is expected to be a dominant background source around the η' mass. The contribution in the $\gamma\gamma$ invariant mass spectrum were evaluated using MC simulations, where the samples of four processes ($\pi^0\Delta^+$, $\pi^0 N(1520)^+$, $\pi^0 N(1650)^+$, and non resonant $\pi^0\pi^0$ production) were generated.

To estimate the scale factors of the four samples, $\pi^0 p$ invariant mass distributions of the above MC simulations were simultaneously fitted to the spectra of the real data. For this purpose, the $\pi^0\pi^0 p$ events was exclusively selected in the real data by the following criteria:

1. Four neutral clusters and one charged cluster are found at BGOegg.
2. Missing mass of $\pi^0\pi^0$, $MM_{\pi\pi}$, is required to be in the range of $860 \leq MM_{\pi\pi} < 1020$ MeV/c².
3. The cosine of an opening angle between the missing momentum of $\pi^0\pi^0$ and the direction of the charged cluster is above 0.98.

In order to get a large reduction factor for backgrounds other than the $2\pi^0$ photo-production, the conditions 2–3, corresponding to the 4-momentum conservation, were tightly determined by neglecting the Fermi motion inside a carbon target. Figure 5.6 shows the $\pi^0\pi^0$ invariant mass distributions for five bins of the incident photon beam energy. The normalization results of individual MC processes are also shown in the same figure. The $\gamma\gamma$ invariant mass spectra of individual processes were then obtained by doing the same analysis as the procedure adopted for $\eta' \rightarrow \gamma\gamma$. The sum of $\gamma\gamma$ mass spectra was finally produced by adding the MC spectra with the scale factors determined in the above normalization. Figure 5.7 shows the summed $\gamma\gamma$ invariant mass distributions. These spectra have no specific structure around the η' mass.

The summed distributions are well described by a single form of the following smooth function:

$$F_{M(\gamma\gamma)} = \exp(p_0 + p_1x + p_2x^2 + p_3x^3), \quad (5.2)$$

where p_0 – p_3 are free parameters in the $\gamma\gamma$ mass spectrum fit. Figure 5.8 shows the χ^2 values of fits to the $\gamma\gamma$ spectrum using the above function in different momentum regions and fit ranges. It turns out that the spectrum can be well fitted when the upper bound of a fit range is set below 1150 MeV/c². Note that smaller χ^2 values for $1.0 \leq P(\gamma\gamma) < 1.5$ GeV/c come from the less number of simulated events in the momentum region. The validity of Eq. 5.2 for the variation of scale factors of generated samples were tested by changing the individual scales to $\pm 5\sigma$ values, where σ is the error of a normalization fit. Figure 5.9 shows the χ^2 values of $\gamma\gamma$ spectrum fits with the function (5.2) for individual conditions of varied scale factors. In any case, the χ^2 values are reasonable when the upper bound of the fit region is set below 1150 MeV/c² as well. Therefore, Eq. 5.2 with free parameters is appropriate to express the $\gamma p \rightarrow \pi^0\pi^0p$ backgrounds in any momentum slice.

$\gamma p \rightarrow \pi^0\eta p$ process

The $\pi^0\eta$ production events were also examined as one of multi-meson backgrounds. Non-resonant $\pi^0\eta$ process and $a_0(980)$ production, decaying to $\pi^0\eta$, were simulated with isotropic angular distributions of reaction and decay products in the center-of-mass and meson rest frame, respectively. Scale factors of the MC samples to the real amounts were obtained by fitting the simulated distributions of $\pi^0\eta$ invariant mass simultaneously to the corresponding mass spectrum in the real data. The selection

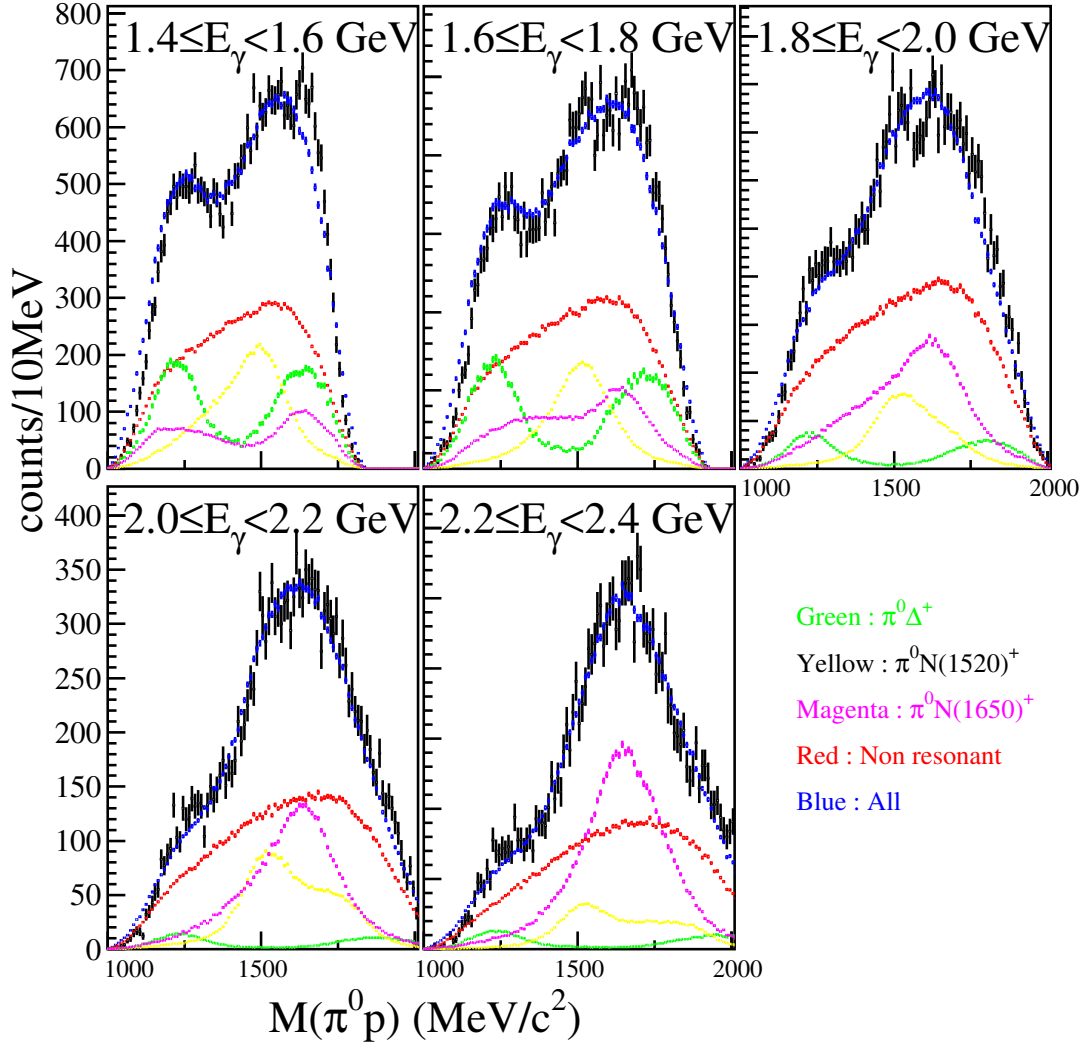


Figure 5.6: The invariant mass spectra of $\pi^0\pi^0$ for five bins of the incident photon beam energy. The black points show the real data and the colored points show the fitting results of the simulated spectra. The green, yellow, magenta, red points represent $\pi^0\Delta^+$, $\pi^0 N(1520)^+$, $\pi^0 N(1650)^+$, and non-resonant $\pi^0\pi^0$ processes, respectively. The blue points are the sum of these simulated spectra after the fits.

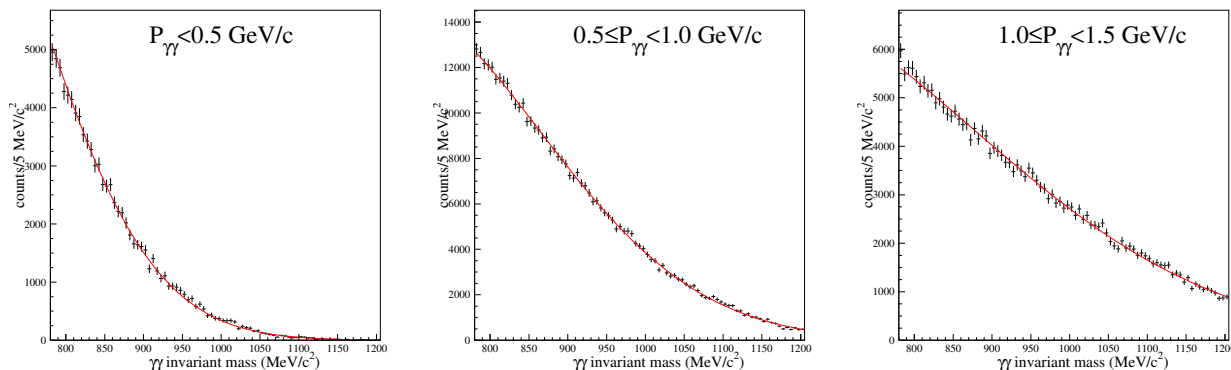


Figure 5.7: The $\gamma\gamma$ invariant mass distributions simulated for $\gamma p \rightarrow \pi^0\pi^0 p$ in different momentum bins. The fitted functions are shown by red lines.

criteria of $\gamma p \rightarrow \pi^0\eta p$ events in the real data were defined as follows:

1. Four neutral clusters and one charged cluster are detected at BGOegg.
2. Missing mass of $\pi^0\eta$, $MM_{\pi\eta}$, is required to be in the range of $820 \leq MM_{\pi\eta} < 1000 \text{ MeV}/c^2$.
3. The cosine of an opening angle between the missing momentum of $\pi^0\eta$ system and the direction of the charged cluster is above 0.98.

There is accidental contamination of $\pi^0\pi^0\pi^0 p$ events with missing two photons in the $\pi^0\eta$ invariant mass distribution. Thus, a $\gamma p \rightarrow \pi^0\pi^0\pi^0 p$ process was also simulated, and the normalization fit was done with 4γ spectrum from this process in addition to non-resonant $\pi^0\eta$ and a_0 production spectra. Figure 5.10 shows the $\pi^0\eta$ invariant mass distributions for five bins of the incident photon beam energy and the normalization results of individual MC processes.

Figure 5.11 shows the simulated $\gamma\gamma$ spectra of $\pi^0\eta$ events in addition to the $\pi^0\pi^0$ case. The non-resonant $\pi^0\eta$ sample and the a_0 sample were mixed according to the determined scale factors. Here, the $\gamma p \rightarrow \pi^0\pi^0\pi^0 p$ process was neglected as described later. A strength of the $\pi^0\eta$ contribution is 20–50% of those of $\pi^0\pi^0$ contribution around the η' mass depending on the momentum of a $\gamma\gamma$ system. The $\pi^0\eta$ sample itself and the sum of $\pi^0\pi^0$ and $\pi^0\eta$ events make no specific structure around the η'

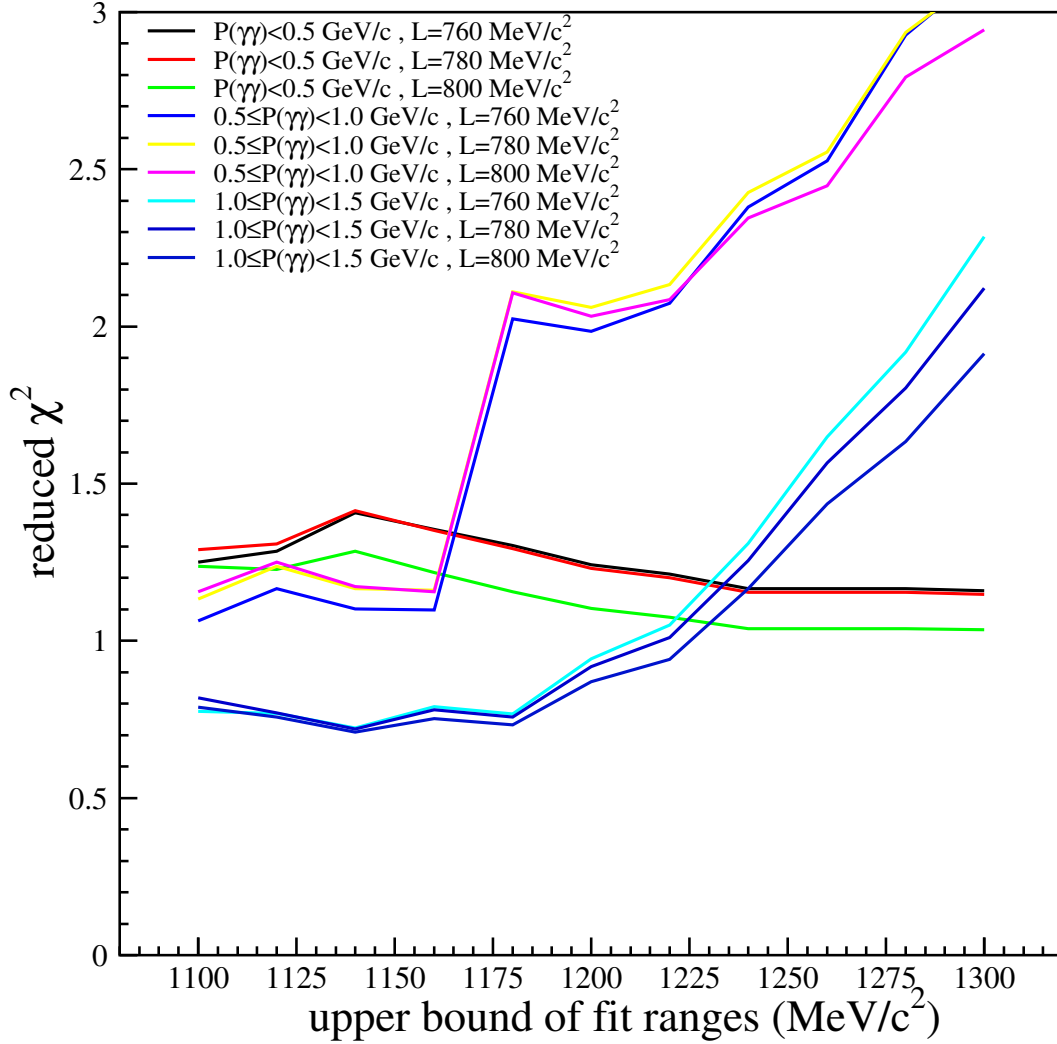


Figure 5.8: The reduced χ^2 values of fits to the $\gamma\gamma$ spectrum with the function (5.2) for the $\pi^0\pi^0$ production processes. The fit was performed in different momentum regions and fit ranges. The horizontal axis represents an upper bound of the fit range. A lower bound of the fit range L and the selected momentum region are described inside the figure.

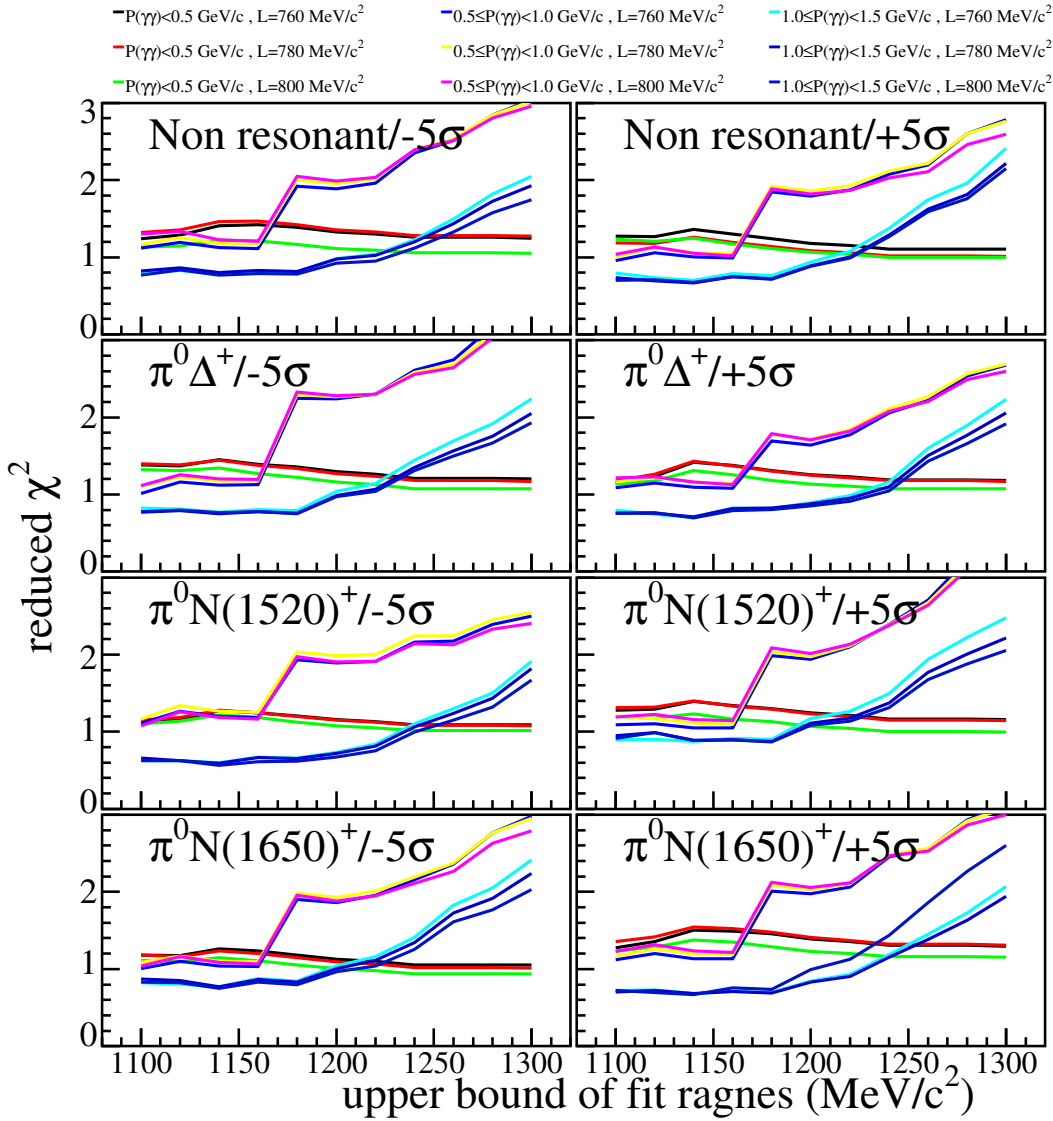


Figure 5.9: Reduced χ^2 values in the fit of Eq. 5.2 to the simulated $\gamma\gamma$ spectrum with varied scale factors for $\pi^0\pi^0$ production processes. The fit was performed in different momentum regions and fit ranges. The horizontal axis represents an upper bound of the fit range. A lower bound of the fit range L and the selected momentum region are described at the top of the figure. The conditions of scale factor setting are described inside individual panels: the process whose scale factor is varied, and the direction of 5σ variation.

mass in the $\gamma\gamma$ invariant mass distribution. Figure 5.12 shows the χ^2 values of fits to the sum of $\pi^0\pi^0$ and $\pi^0\eta$ background distributions using the function (5.2). Even in the case of considering both processes, the background distribution can be well expressed by this function with free parameters.

$\gamma p \rightarrow \pi^0\pi^0\pi^0 p$ process

The $3\pi^0$ production process was also examined as a background source in the $\gamma\gamma$ invariant mass distribution. The contribution of this process is expected to be small compared to $\pi^0\pi^0$ or $\pi^0\eta$ events because six photons are emitted in the final state. Non-resonant $\pi^0\pi^0\pi^0$ production and the single η production decaying into $\pi^0\pi^0\pi^0$ were taken into account at the normalization process. Non-resonant $\pi^0\pi^0\pi^0$ production was simulated with isotropic angular distributions in the center-of-mass system. The absolute normalization of each component in the real data was performed using a $\pi^0\pi^0\pi^0$ invariant mass distribution. Figure 5.13 shows the $\pi^0\pi^0\pi^0$ invariant mass spectra for five bins of the incident photon beam energy. These distributions were fitted with the simulated non-resonant $\pi^0\pi^0\pi^0$ distribution and a Gaussian function corresponding to the η peak in order to determine the scale factors of these processes. Then the contribution of these processes in the $\gamma\gamma$ invariant mass spectrum was evaluated from the amount of normalized MC samples, where the same procedure as the analysis for the $\eta' \rightarrow \gamma\gamma$ process was adopted. It was confirmed that only a few events per invariant mass bin survive for $\pi^0\pi^0\pi^0$ background while hundreds of other background events exist around the η' mass. Therefore, it is concluded that the $\pi^0\pi^0\pi^0$ production process is negligible.

5.3.4 Unphysical background

As described in Sec. 4.2, there are a lot of charged particles coming from the reactions at upstream materials, making fake “neutral” clusters at BGOegg. Although the cut conditions described in Sec. 4.2 have been introduced to eliminate these “unphysical” clusters, they may remain as backgrounds after those cuts. Actually, such a situation is indicated by the distribution of effective cluster radius R_{cls} , as shown in Figure 5.14. The R_{cls} ideally distributes in two peaks shown in the right panel (MC simulation), where the peak at $R_{\text{cls}} \sim 10$ mm represents normal clusters, made by particles from

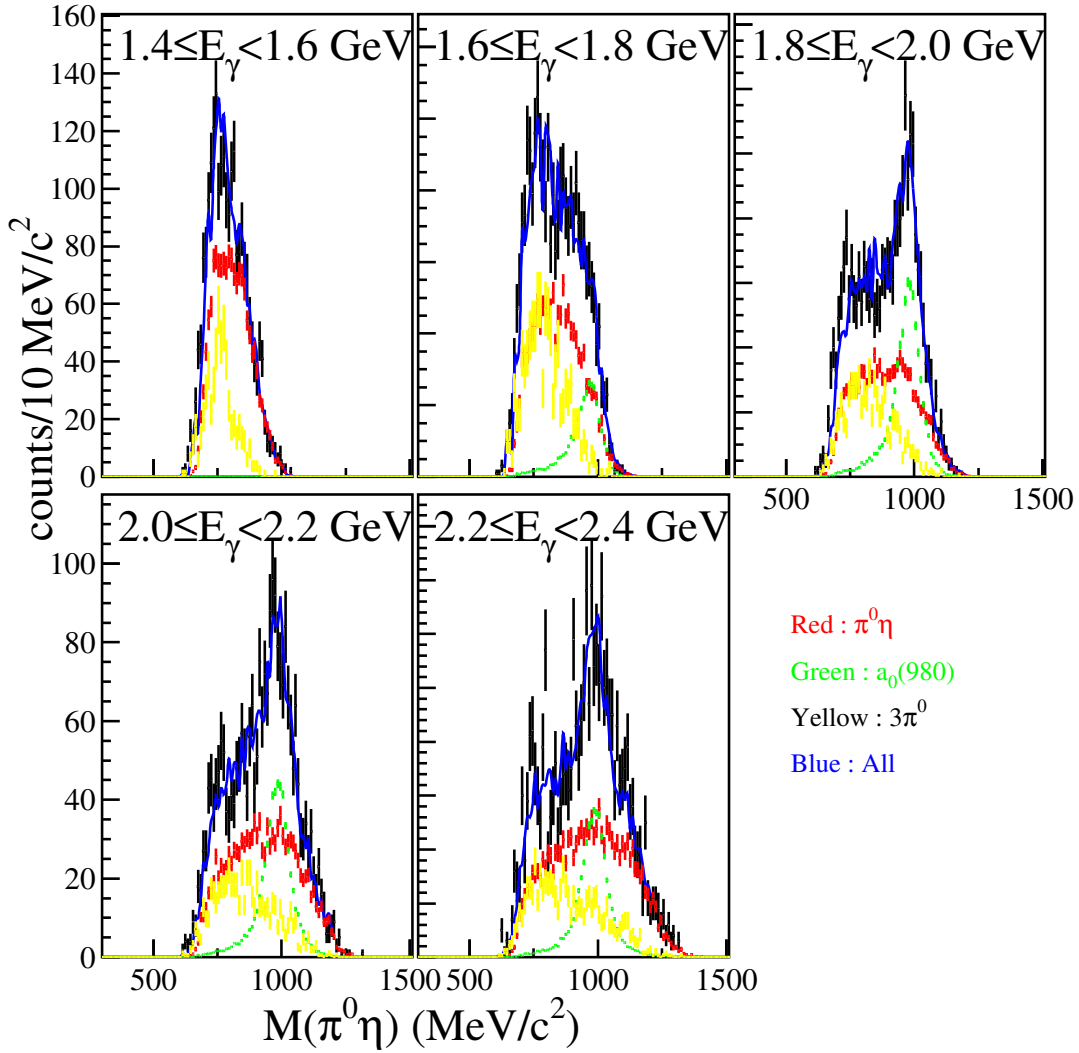


Figure 5.10: The invariant mass spectra of $\pi^0\eta$ for five bins of the incident photon beam energy. The black points show mass spectra from the real data, and the colored points show fitting results of the simulated spectra. The red, green, yellow points represent $\pi^0\eta$, $a_0(980)$, $\pi^0\pi^0\pi^0$ events, respectively. The blue points are the sum of these simulated spectra after the fit.

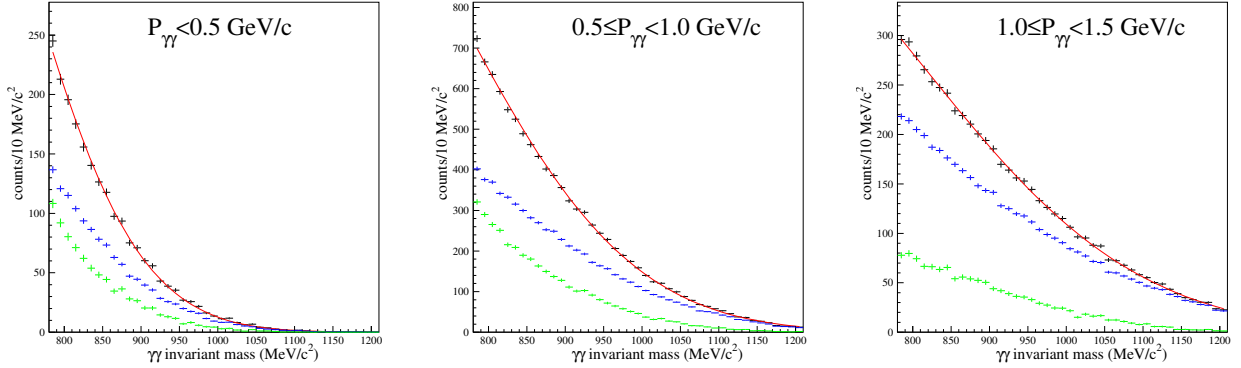


Figure 5.11: The $\gamma\gamma$ invariant mass distributions simulated with $\gamma p \rightarrow \pi^0 \eta p$ in addition to $\gamma p \rightarrow \pi^0 \pi^0 p$ in different momentum bins. The blue and green points represent $\pi^0 \pi^0$ and $\pi^0 \eta$ events, respectively. The black points are the sum of them. The fitted functions are shown by red lines

the target, and the peak at $R_{\text{cls}} \sim 30$ mm represents large clusters combining two photons, which can be finally removed by the R_{cls} cut described in Sec. 4.2. However, there is another component distributing widely and continuously in the real data shown in the left panel of Fig. 5.14. This can be interpreted as the distribution of unphysical clusters, and some of them seem to survive even after requiring the R_{cls} cut. In this subsection, the background spectrum made by unphysical clusters remaining in the final sample is discussed.

To evaluate the amount of unphysical clusters and their $\gamma\gamma$ spectrum, events in the region of $18 \leq R_{\text{cls}} < 25$ mm, where unphysical clusters should be dominant, were selected. As shown in the left panel of Fig. 5.15, there are forward and backward peaks in the polar angle distribution of selected unphysical clusters. The backward component is rejected by tight R_{cls} -cut conditions for backward layers. (See Sec. 4.2.) Therefore, only the forward component can remain after the R_{cls} cut. Actually, as shown in the right panel of Fig. 5.15, few events survive after the R_{cls} cut in the region of $\theta > 80$ degrees, where θ is the polar angle of a $\gamma\gamma$ system. Thus, the forward component with $\theta \leq 80$ degrees was further selected from the sample of unphysical cluster events with $18 \leq R_{\text{cls}} < 25$ mm. The absolute strength of its contribution was determined by fitting the $\gamma\gamma$ invariant mass spectrum made by the above sample of unphysical clusters to the real data spectrum in the mass region of

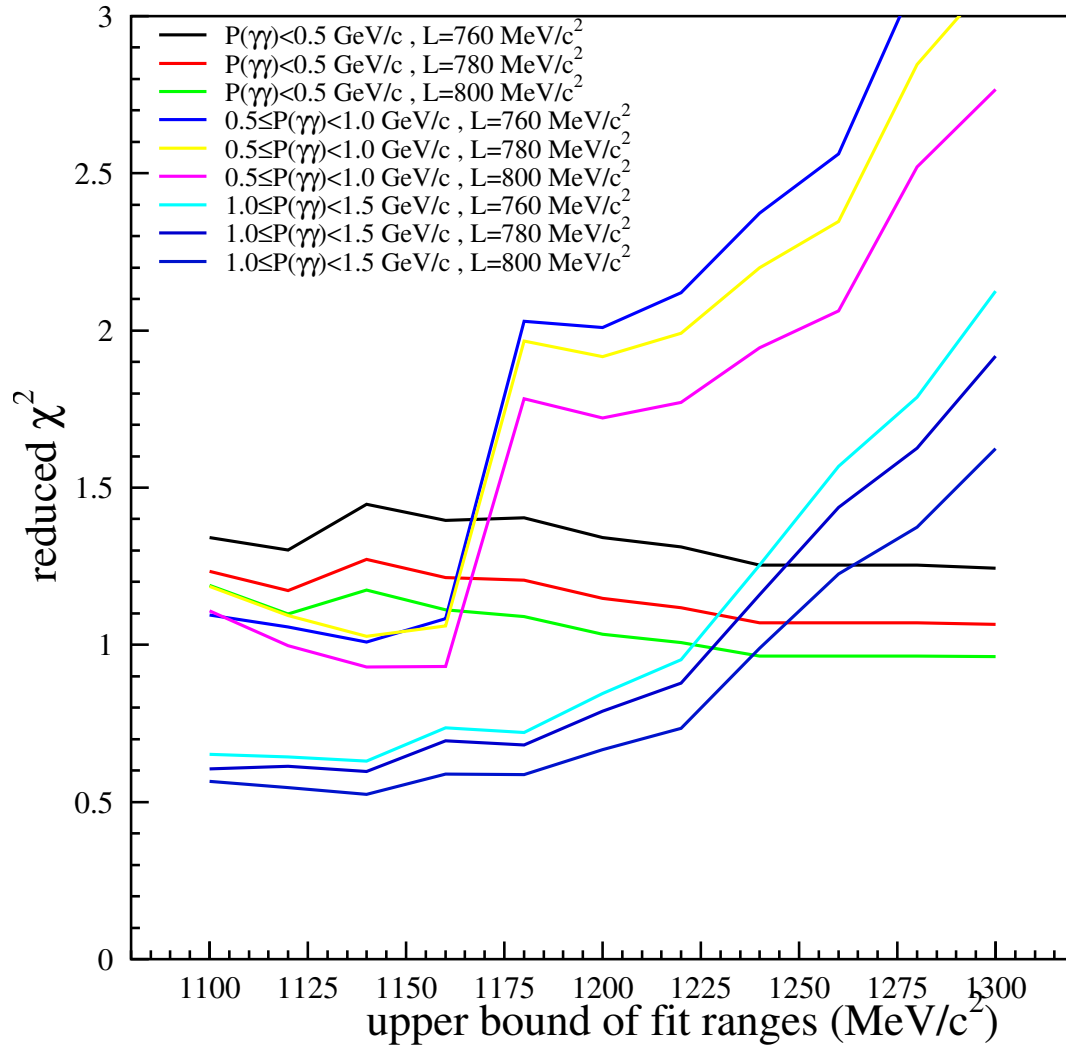


Figure 5.12: The χ^2 values of fits with the function 5.2 to the sum of normalized $\pi^0\pi^0$ and $\pi^0\eta$ background distributions. The fit was performed in different momentum regions and fit ranges. The horizontal axis represents an upper bound of the fit range. A lower bound of the fit range L and the selected momentum region are described inside the figure.

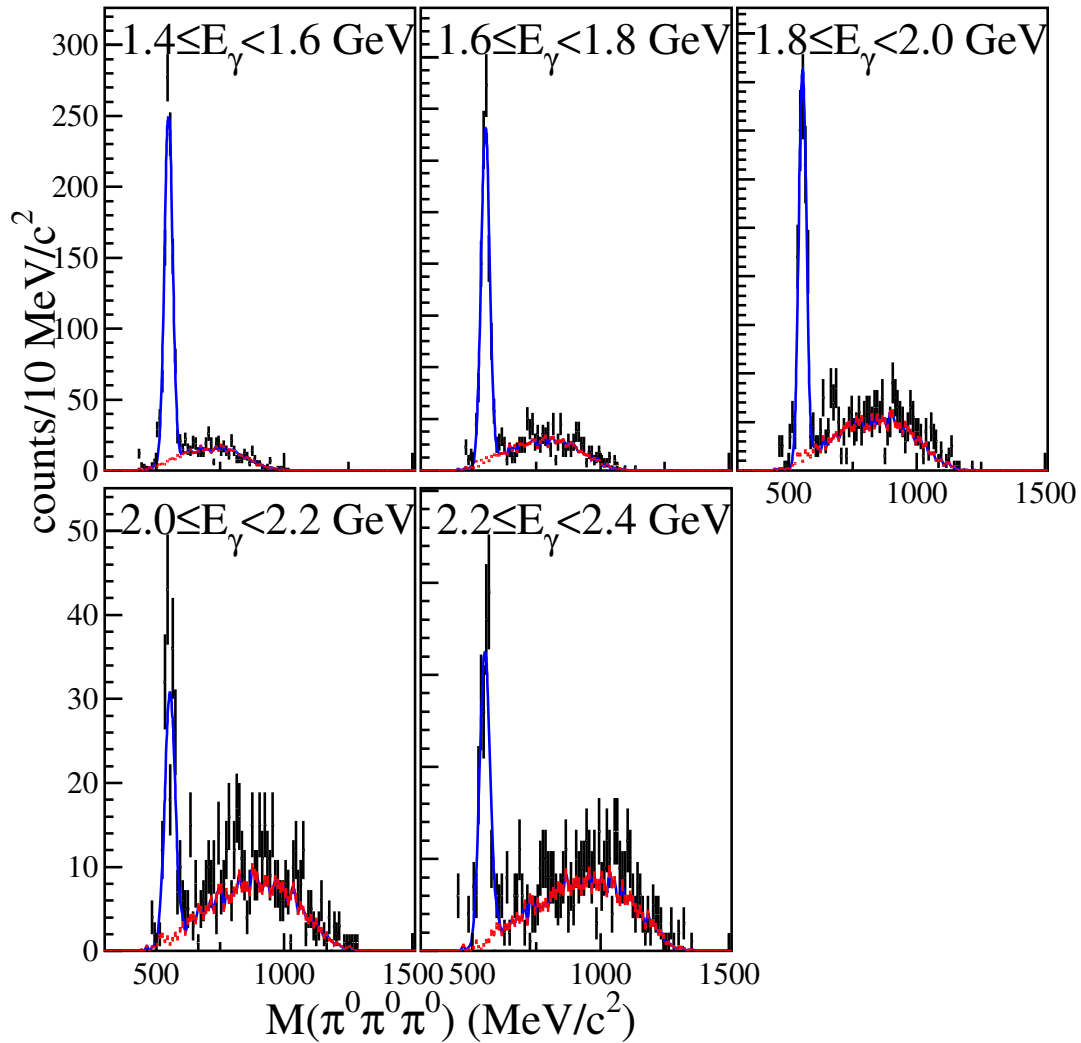


Figure 5.13: The invariant mass spectra of $\pi^0\pi^0\pi^0$ for five bins of the incident photon beam energy. The black points come from a sample selected in the real data, and the red points show the simulated spectra of non-resonant $\pi^0\pi^0\pi^0$. A Gaussian function fitted to the η peak is shown by blue lines.

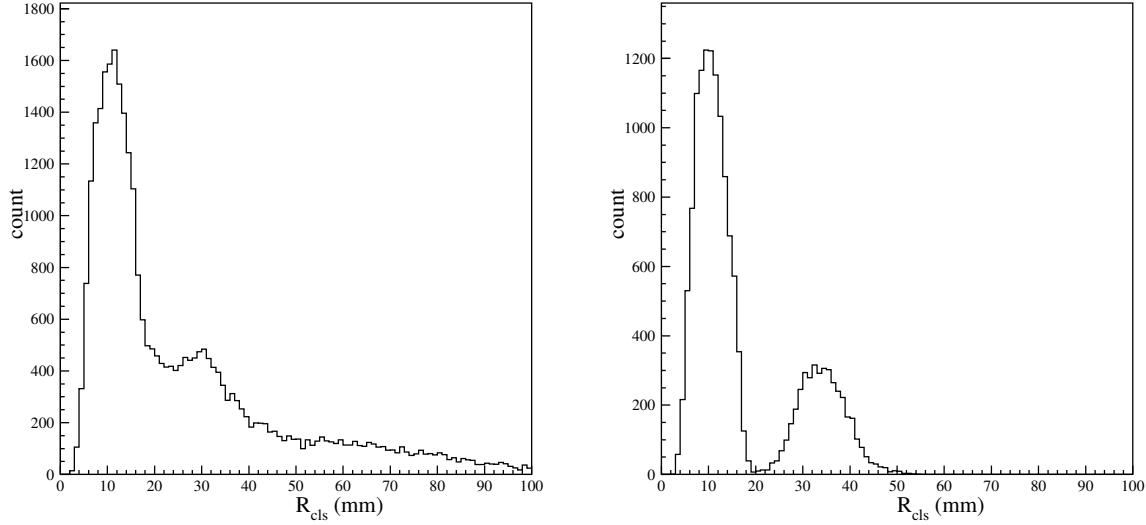


Figure 5.14: The distributions of the effective cluster radius R_{cls} in the real data (left) and the MC simulation (right). The $\gamma p \rightarrow \pi^0 \pi^0 p$ events were generated in the MC sample.

$M_{\gamma\gamma} > 1200 \text{ MeV}/c^2$, where the contributions of physics processes should be limited. This normalization fit was performed using the normalized spectra of $\pi^0 \pi^0$ and $\pi^0 \eta$ events determined in the previous subsection. Figure 5.16 shows the scaled spectra of unphysical clusters along with those of $\pi^0 \pi^0$ and $\pi^0 \eta$ events. The contamination ratio of unphysical clusters in the $\gamma\gamma$ invariant mass spectrum were evaluated to be less than 10% around the η' mass region. Figure 5.17 shows the χ^2 values of fits to the sum of $\pi^0 \pi^0$, $\pi^0 \eta$, and unphysical background distributions by using Eq. 5.2 as a fitting function. It was confirmed that the function (5.2) with free parameters still describes the background spectra considering the contamination of unphysical clusters in addition to $\pi^0 \pi^0$ and $\pi^0 \eta$ events.

5.4 Fit to the $\gamma\gamma$ invariant mass spectrum

This section describes the fit of the prepared spectral functions to the measured $\gamma\gamma$ invariant mass distributions. In Sec. 5.4.1, appropriate conditions of the line shape analysis to investigate in-medium modification of the η' mass spectrum are discussed.

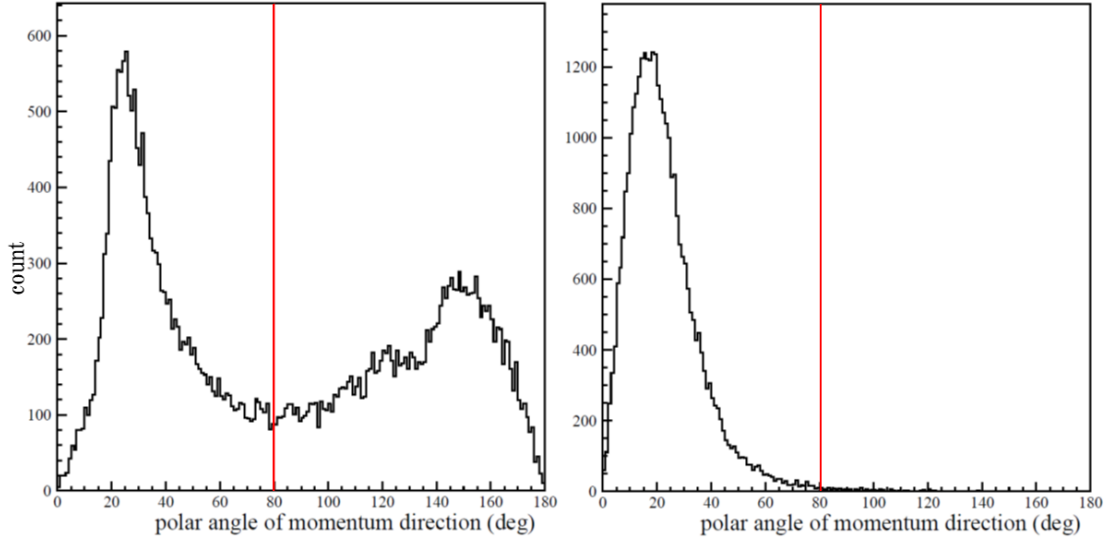


Figure 5.15: The polar angle distributions of unphysical clusters in the region $18 \leq R_{\text{cls}} < 25$ mm (left), and the surviving events after the R_{cls} -cut (right). In the left panel, events below the cut point indicated by a red line were selected as the sample to examine the $\gamma\gamma$ distribution of unphysical clusters.

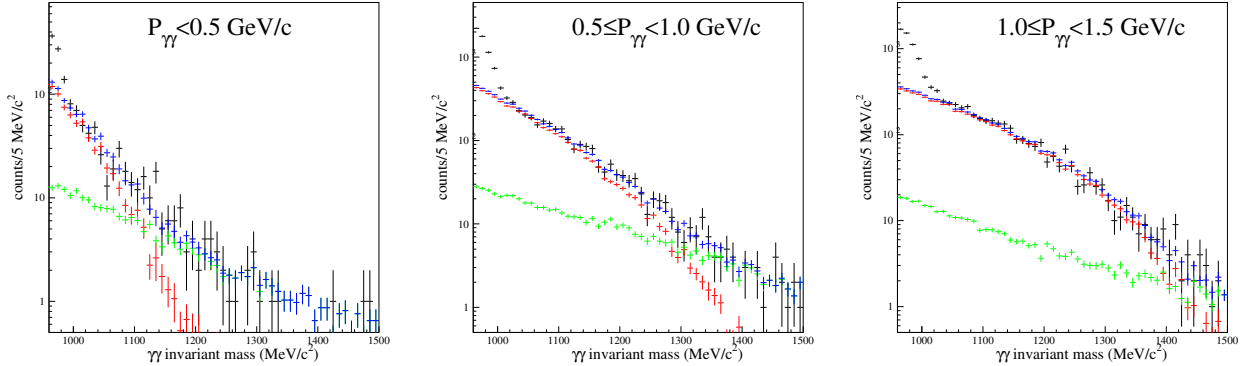


Figure 5.16: The $\gamma\gamma$ invariant mass distributions above the η' mass region for different $\gamma\gamma$ momentum bins. The vertical axes are shown in log scales. The black points represent the surviving events after all cuts. The green points indicate the spectra of unphysical cluster events. The red points are the sum of simulated and normalized spectra of $\pi^0\pi^0$ and $\pi^0\eta$ events.

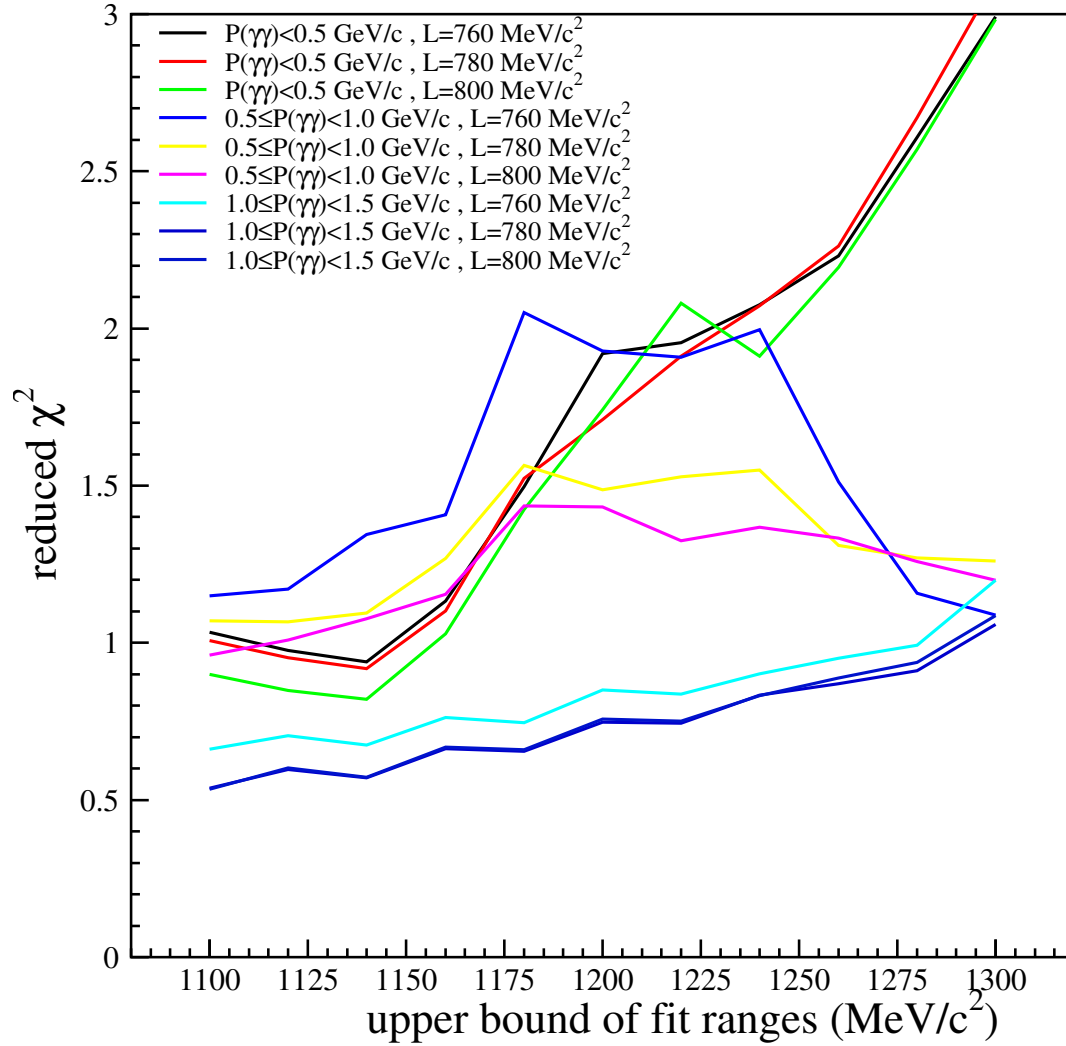


Figure 5.17: The χ^2 values of fits to the sum of normalized $\pi^0\pi^0$, $\pi^0\eta$, and unphysical background distributions by using Eq. 5.2 as a fitting function. The fit was performed in different momentum regions and fit ranges. The horizontal axis represents an upper bound of the fit range. A lower bound of the fit range L and the momentum region are described inside the figure.

The fit results are shown in Sec. 5.4.2.

5.4.1 Momentum cut of the samples for the line shape analysis

As the momentum of the η' decreases, the fraction of the η' decay inside a nucleus to the quasi-free events is expected to increase due to a short decay length in the laboratory frame. Thus, low-momentum events should be used for the line shape analysis. Figure 5.18 shows the momentum distribution of $\gamma\gamma$ pairs for events in the η' mass region of the real data. The number of events in the low-momentum region is limited, as shown in Fig. 5.18. Therefore, it is important to determine an appropriate cut point considering both the expected ratio of in-medium signals and the statistics of a whole sample.

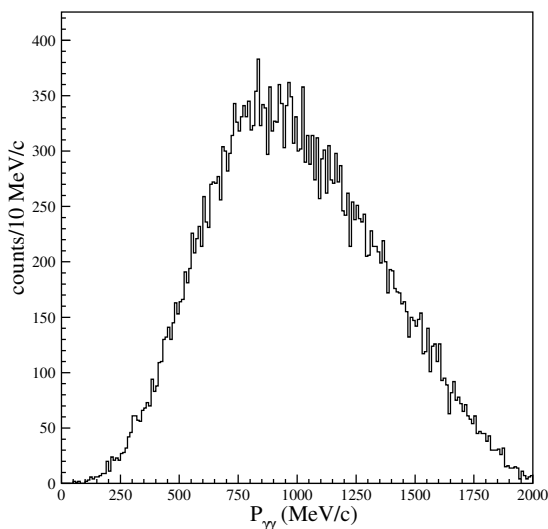


Figure 5.18: The $\gamma\gamma$ momentum distribution for the mass region of $860 \leq M_{\gamma\gamma} < 1060$ MeV/ c^2 in the real data.

The relative amount of in-medium signals to the statistical fluctuations of backgrounds was studied as a function of the η' momentum by using a MC simulation. The conditions of the MC simulation are same as those explained in Sec. 6.1.1. The generated number of in-medium η' decays was normalized by comparing the amount of η' mesons going outside of a nucleus with that of quasi-free η' events in the real

data for every 100 MeV/c bin. Figure 5.19 shows the ratio N_{in}/\sqrt{N} as a function of the momentum cut point P_{cut} dividing the sample to the low-momentum region ($P_{\gamma\gamma} \leq P_{\text{cut}}$) and the high-momentum region ($P_{\gamma\gamma} > P_{\text{cut}}$), where N_{in} and N represent the number of in-medium η' events and that of background events, respectively. The number of background events were determined by the events in the mass region of $860 \leq M_{\gamma\gamma} < 960$ MeV/c² in the real data. For the low-momentum sample, N_{in}/\sqrt{N} becomes small when the momentum cut point is too low. This happens due to the poor statistics although the fraction of in-medium decays is expected to increase. For the high-momentum sample, N_{in}/\sqrt{N} decreases as P_{cut} increases because both the fraction of in-medium decays and the sample statistics become low. Then, it turns out to be appropriate to set $P_{\text{cut}} = 1$ GeV/c for the following reasons:

1. For the sample of $P_{\gamma\gamma} \leq P_{\text{cut}}$, N_{in}/\sqrt{N} stably reach the maximum value at $P_{\text{cut}} \geq 1$ GeV/c.
2. For the sample of $P_{\gamma\gamma} > P_{\text{cut}}$, N_{in}/\sqrt{N} becomes low compared with that of $P_{\gamma\gamma} \leq P_{\text{cut}}$.
3. Enough amount of events exist in both regions.

The sample of $P_{\gamma\gamma} > P_{\text{cut}}$ can be used as a reference of the line shape analysis because of the conditions 2 and 3. Hereafter, the sample of $P_{\gamma\gamma} \leq 1$ GeV/c and $P_{\gamma\gamma} > 1$ GeV/c are referred as the low-momentum sample and the high-momentum sample, respectively.

5.4.2 Fit results of the $\gamma\gamma$ invariant mass spectra

For a fit to the $\gamma\gamma$ invariant mass spectrum, the following function was prepared as described in the previous chapter:

$$F_{\gamma\gamma}(x) = \alpha_1 \{F_\omega(x) + \exp(p_0 + p_1x + p_2x^2 + p_3x^3)\} + \alpha_2 \exp \left\{ \frac{-(x - \mu)^2}{2\sigma_{\text{QF}}^2} \right\}, \quad (5.3)$$

where $\alpha_1, \alpha_2, p_0, p_1, p_2, p_3, \mu$ are free fitting parameters. $F_\omega(x)$ is the MC-simulated distribution for ω photoproduction with $\gamma\gamma$ detection, as described in Sec. 5.3.2. The

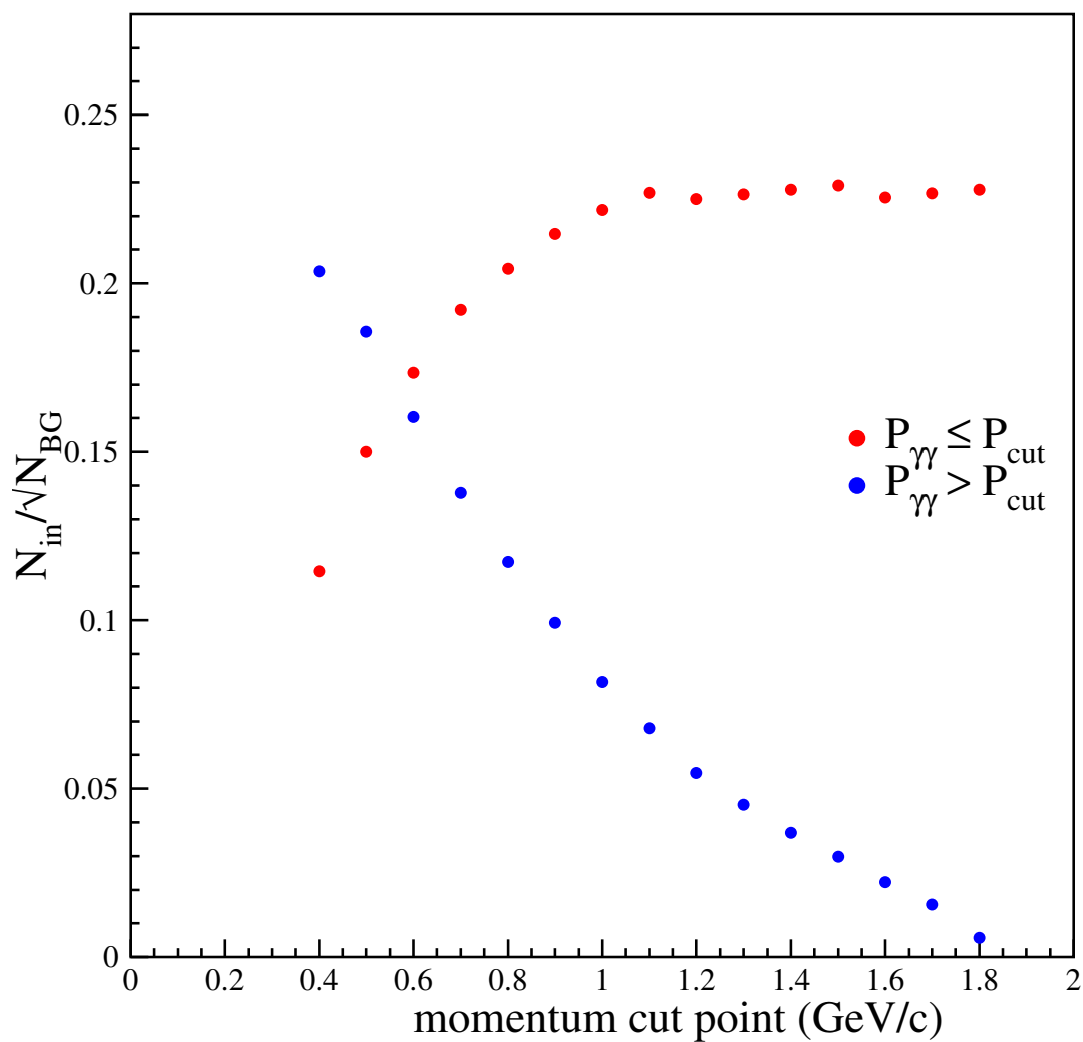


Figure 5.19: The ratio N_{in}/\sqrt{N} as a function of the momentum cut point P_{cut} . Red points show the samples of the low-momentum region ($P_{\gamma\gamma} \leq P_{\text{cut}}$) and blue points show the high-momentum region ($P_{\gamma\gamma} > P_{\text{cut}}$).

second term expresses a main background function for multi-meson photoproduction and unphysical BGOegg hits, as introduced in Secs. 5.3.3 and 5.3.4. A Gaussian form in the third term represents quasi-free η' photoproduction. The σ_{QF} is an experimental mass resolution, determined by using a realistic MC simulation as explained in Sec. 5.3.1. $\sigma_{\text{QF}} = 19.09 \text{ MeV}/c^2$ and $\sigma_{\text{QF}} = 22.48 \text{ MeV}/c^2$ were used for the low-momentum sample and the high-momentum sample, respectively. A fitting region was set to $780 \leq M_{\gamma\gamma} < 1100 \text{ MeV}/c^2$, where a smooth background shape expressed by the function (5.2) was guaranteed as discussed in Sec. 5.3.3.

Figure 5.20 shows a $\gamma\gamma$ invariant mass spectra of the final sample selected by the conditions in Chapter 4. For the high-momentum sample, the spectrum is well reproduced by the fit, returning $\chi^2/ndf = 60.1/58$. On the other hand, the χ^2 of the fit becomes worse with $\chi^2/ndf = 72.1/58$ for the low-momentum sample. Figure 5.21 shows mass dependences of the residual from the fit divided by statistical errors. The left and right panels show the low-momentum and high-momentum samples, respectively. As discussed in Chapter 1, the meson mass spectrum modification can be seen just below the meson pole mass. Therefore, hereafter, we concentrate on the mass region around $910 \text{ MeV}/c^2$ and test whether any excess of the events exists concerning the spectral shape discussed in this chapter or not. It looks that the residuals show particular deviations around $910 \text{ MeV}/c^2$ for the low-momentum sample, while they fluctuate statistically around zero for the high-momentum sample. The worse value of χ^2 for the low-momentum sample comes from the data points of such region. To evaluate the significance of this “excess”, fits were performed by excluding certain regions around $910 \text{ MeV}/c^2$ so that the background functions should be determined without being affected by these regions. The significance was determined by $(N_{\text{data}} - N_{\text{fit}})/\sqrt{N_{\text{data}}}$, where N_{data} and N_{fit} represent the number of events in the excluded region for the real data and the fit result, respectively. The variation of the excluded regions in seven cases are examined. Figure 5.22 shows an example of these fits. Table 5.1 shows the obtained significances for individual cases of excluded regions. We obtained significances of at least 3.3σ , although the values varied up to 3.9σ due to the instability of the fits. This suggests that there is a component which can not explained by the quasi-free η' peak and known background distributions in the low-momentum sample.

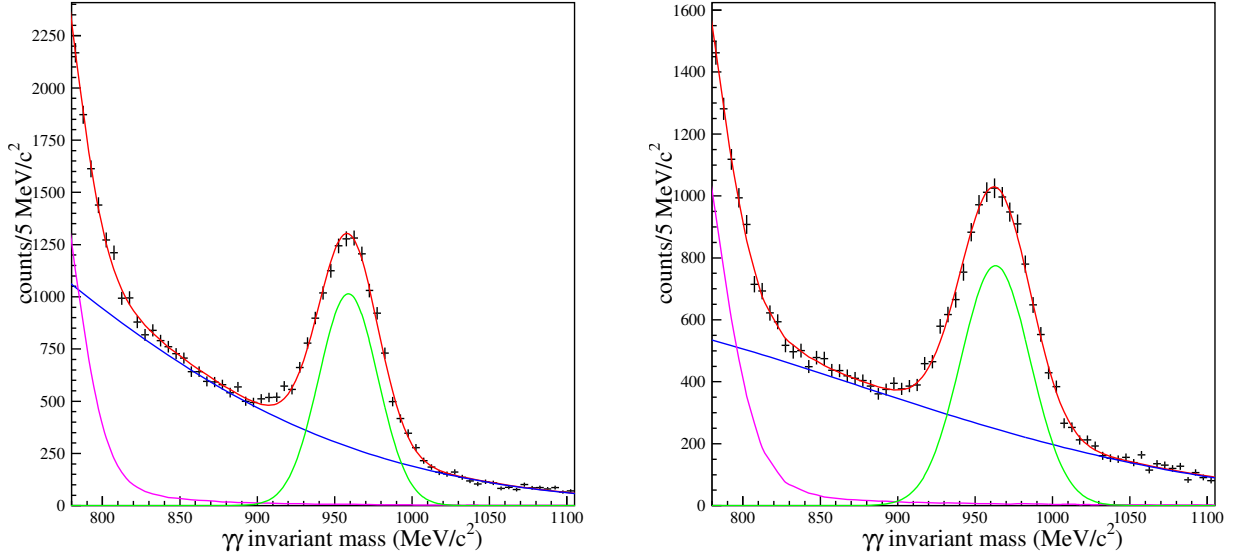


Figure 5.20: The $\gamma\gamma$ invariant mass spectra of selected signal samples. The left and right panels show the low-momentum and high-momentum samples, respectively. Fitting results with only background functions are also shown in those panels. The green, blue, magenta, and red lines show the quasi-free η' peak, the smooth backgrounds from multi-meson photoproduction etc., the background from ω meson photoproduction, and the sum of all components, respectively.

Table 5.1: The obtained significance of deviations from the fits excluding individual regions.

Excluded region (MeV/c^2)	Significance
$870 \leq M_{\gamma\gamma} < 920$	3.8
$880 \leq M_{\gamma\gamma} < 920$	3.7
$890 \leq M_{\gamma\gamma} < 920$	3.4
$870 \leq M_{\gamma\gamma} < 930$	3.6
$880 \leq M_{\gamma\gamma} < 930$	3.7
$890 \leq M_{\gamma\gamma} < 930$	3.3
$900 \leq M_{\gamma\gamma} < 930$	3.9

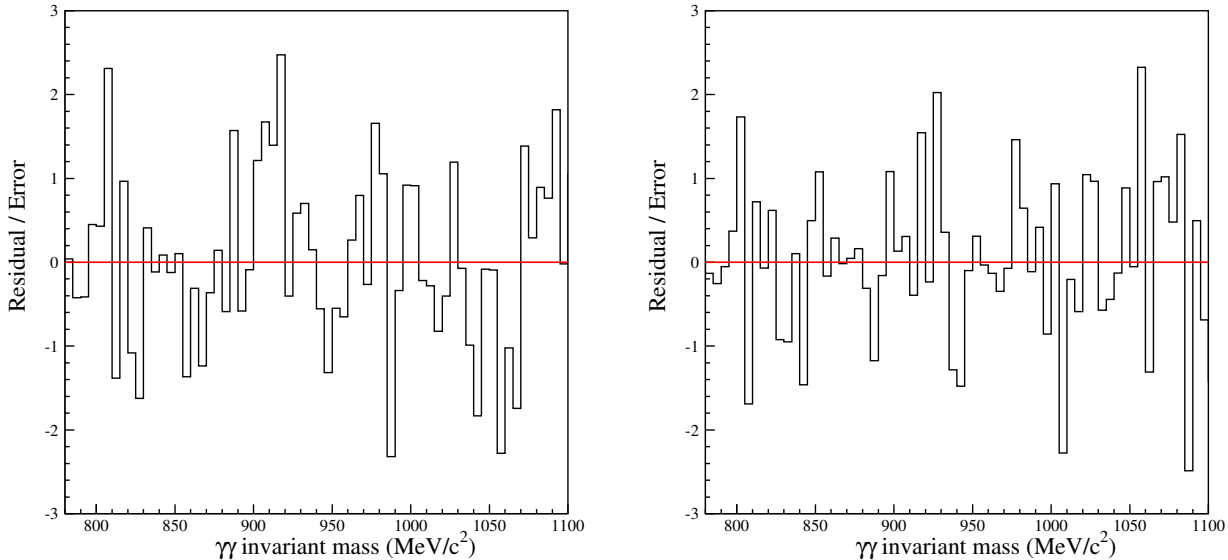


Figure 5.21: The mass dependences of the residual from the fit divided by statistical errors. The left and right panels show the low-momentum and high-momentum samples, respectively.

5.4.3 Examination of systematic uncertainties

This section describes the systematic studies to examine whether other sources could make the enhancement in the $\gamma\gamma$ invariant mass spectra or not. The most suspicious factor which distorts the spectrum is “leaked energy” of clusters. The leaked energy is the energy which escaped from the area of the cluster definition. Although the leaked energy is taken into account by applying the leak correction based on a MC simulation, as described in Chapter 3, events with higher leaked energy might result in the low $\gamma\gamma$ invariant masses. Thus, a tighter selection condition to eliminate clusters with high leaked energies is examined although the acceptance decreases.

The leaked energy E_{leak} is defined by the energy deposit outside the cluster and within 120 mm from the closest cluster center. (See Fig. 5.23.) Figure 5.24 shows the distribution of the leaked energy ratio to the cluster energy, $E_{\text{leak}}/E_{\text{leak}}^{\text{fin}}$, for individual cluster energy bins. The cut points are determined depending on the cluster energy so that 2/3 of the clusters are accepted. The cut are applied to each cluster.

The effectiveness of the developed cut were confirmed using the $\eta \rightarrow \gamma\gamma$ spectrum.

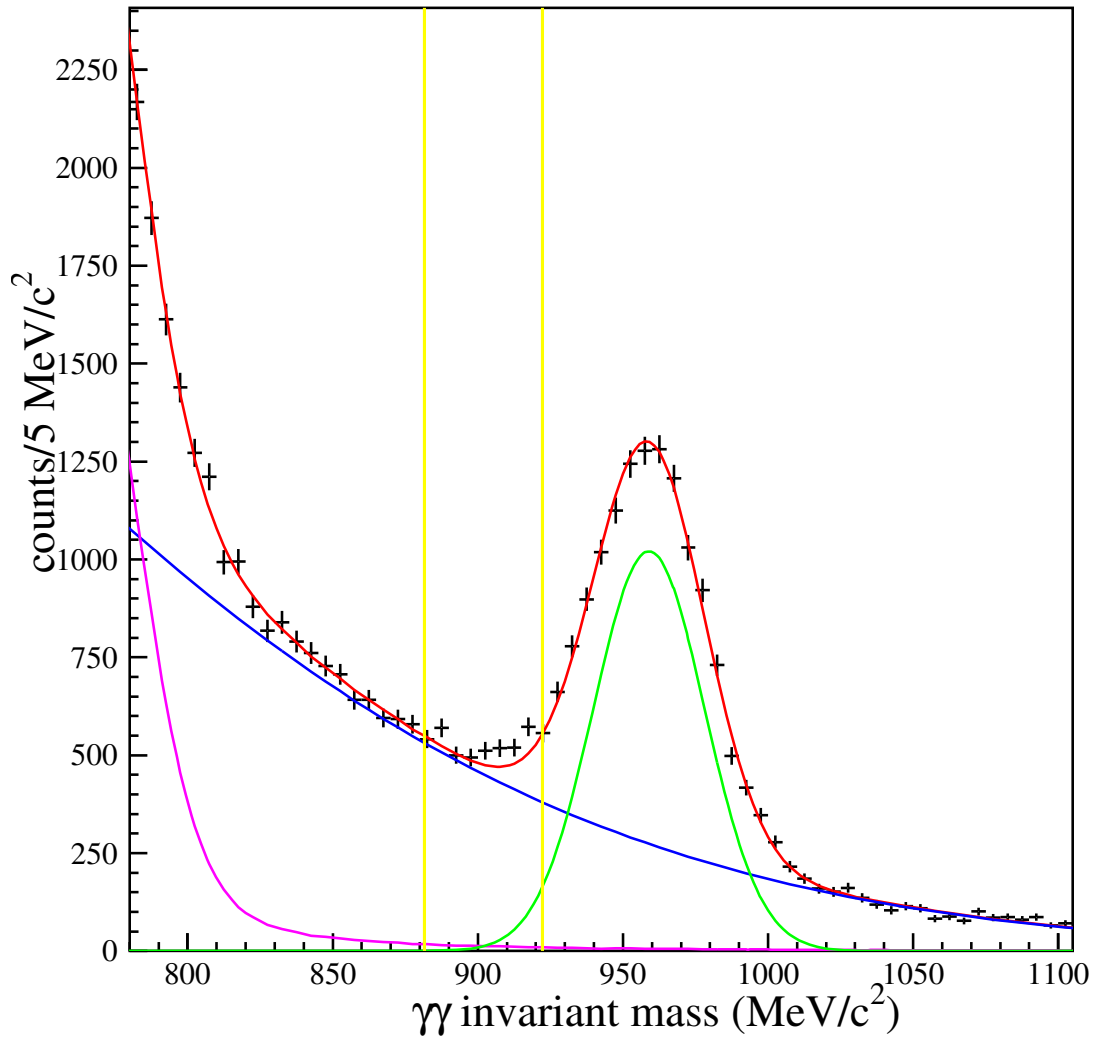


Figure 5.22: The spectral fit excluding a region $880 \leq M_{\gamma\gamma} < 920 \text{ MeV}/c^2$. The green, blue, and red lines show the quasi-free η' peak, the sum of smooth backgrounds from multi-meson photoproduction etc. and ω photoproduction, and the sum of all components, respectively. The excluded region is shown by yellow lines.

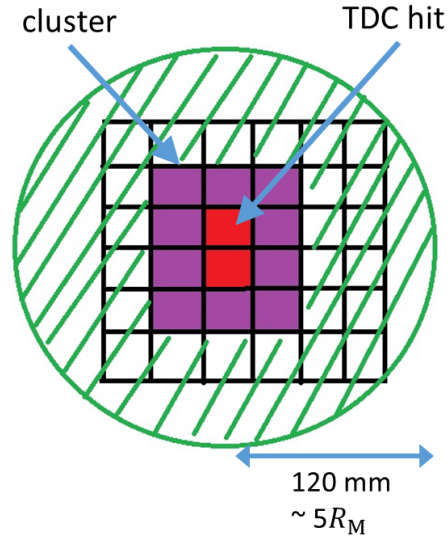


Figure 5.23: The definition of the leaked energy E_{leak} in this analysis. The cluster is defined by crystals indicated in red and violet. The leaked energy E_{leak} is defined as the energy deposit in the shadowed area.

The η spectrum is affected by the leaked energy because there are a lot of clusters with energies less than 200 MeV, which have significantly larger $E_{\text{leak}}/E_{\text{leak}}^{\text{fin}}$. The $\eta \rightarrow \gamma\gamma$ events are selected by the same conditions as used for the $\eta' \rightarrow \gamma\gamma$ analysis. Figure 5.25 shows the $\eta \rightarrow \gamma\gamma$ spectra with $P_{\gamma\gamma} \leq 1$ GeV/c before and after applying the developed cut. A linear combination of a Gaussian function and a 4th-order polynomial function were fitted to the spectra. The fitted functions are also shown in Fig. 5.25 by red lines. The lower tail in the spectrum due to the leaked energy was suppressed by the cut, and the fitness was much improved from $\chi^2/ndf = 158.7/33$ to $\chi^2/ndf = 54.7/33$.

The cut was applied to the $\eta' \rightarrow \gamma\gamma$ analysis, and check the significance of the enhancement obtained in the previous section. The significance was evaluated in the same way as described in Sec. 5.4.2. Table. 5.2 shows the evaluated significances for individual mass regions after applying the cut. Figure. 5.26 shows an example of spectral fits for η' after applying the cut. The significances are consistent with those in Table. 5.1 considering the decrease of statistics by the cut. It has been confirmed that the enhancement in the $\eta' \rightarrow \gamma\gamma$ spectrum does not disappear even after applying

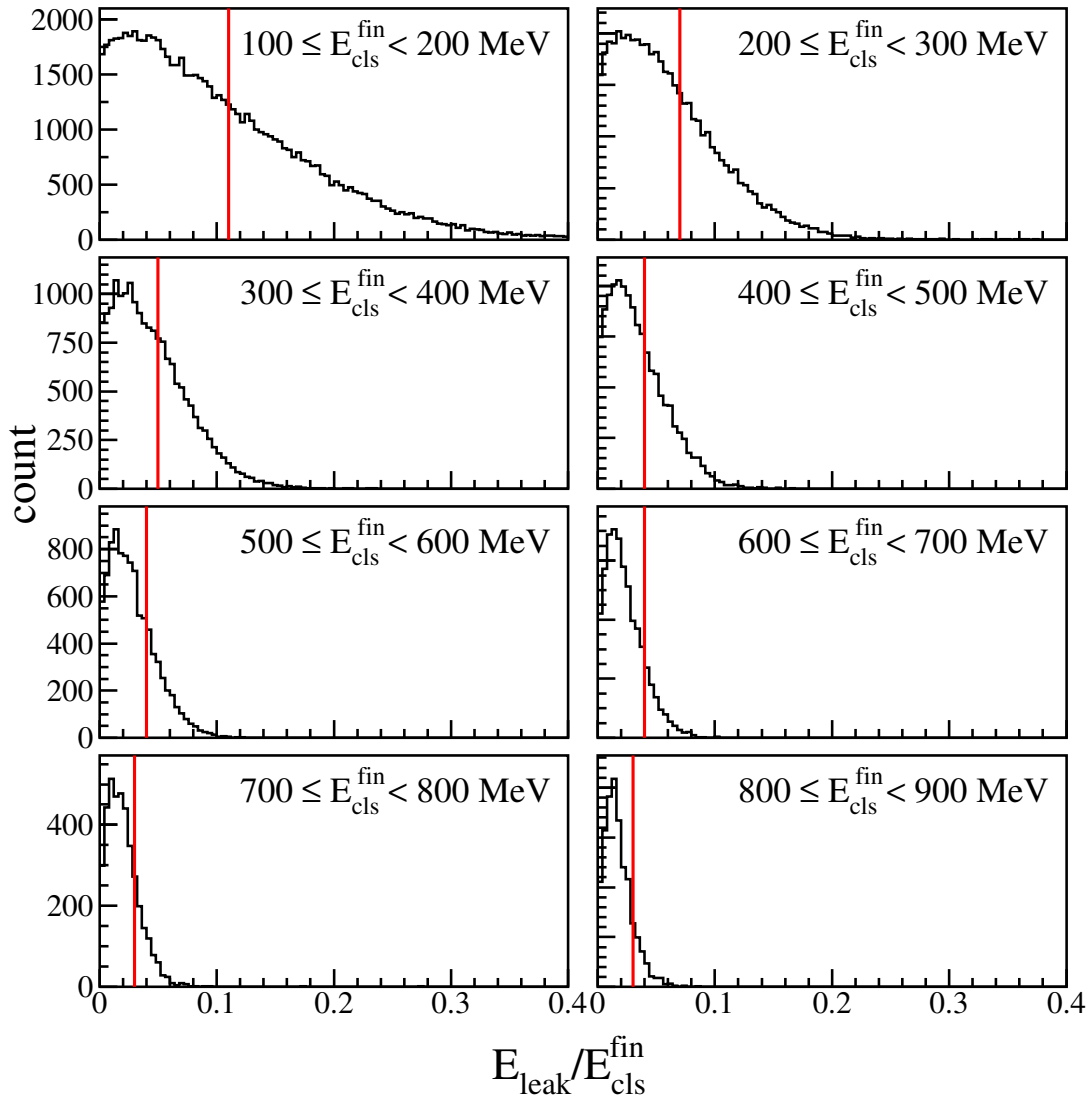


Figure 5.24: The distribution of the leaked energy ratio to the cluster energy, $E_{\text{leak}}/E_{\text{cls}}^{\text{fin}}$, for individual cluster energy bins. The cut points are shown by red lines.

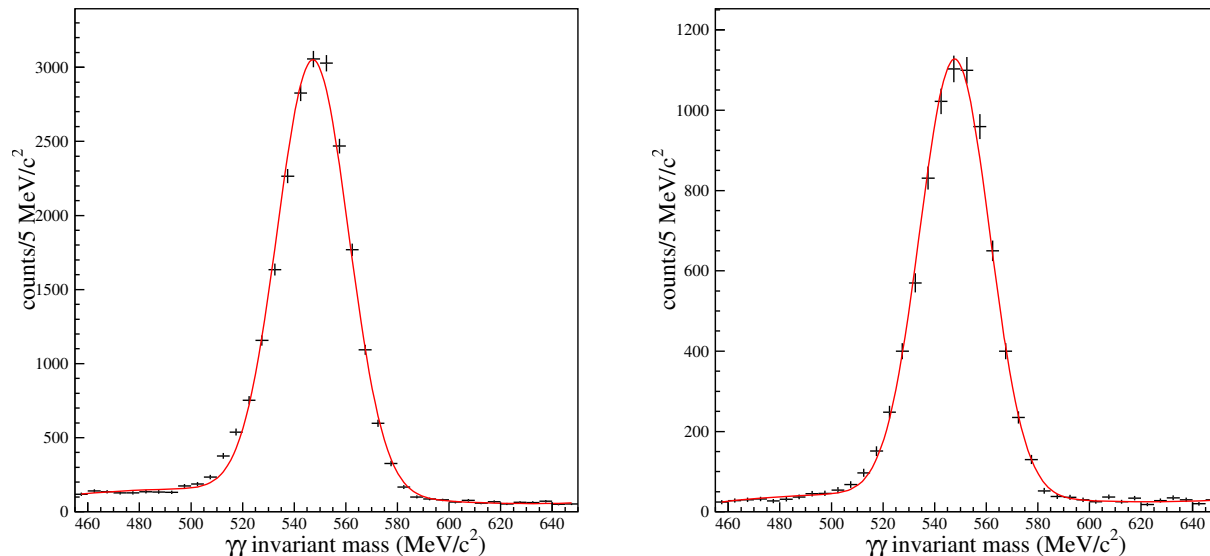


Figure 5.25: shows the $\eta \rightarrow \gamma\gamma$ spectra with $P_{\gamma\gamma} \leq 1$ GeV/c before (left) and after (right) applying the cut to eliminate clusters with high leaked energies. The fitted functions are shown by red lines.

the cut to eliminate clusters with high leaked energies. This result indicates that the enhancement does not come from the leaked energy.

Various systematic studies were also performed. Here, we summarize these studies. The proton target data was analyzed as a reference sample. The η' spectrum was well reproduced by only the quasi-free η' peak and the background functions, and no enhancement was observed in the $\gamma\gamma$ invariant mass spectrum. Details of this analysis are described in Sec. 6.2.1. Some variation of spectral functions to be fitted were examined. It was confirmed that systematic uncertainties due to choice of spectral functions are small. Details of these studies are described in Secs. 6.2.2 and 6.2.3. In addition, some different analysis conditions were examined in order to check the robustness of our results. The spectral enhancement in the low-momentum sample was consistently confirmed in any analysis conditions. Details of these studies are described in Appendix A.

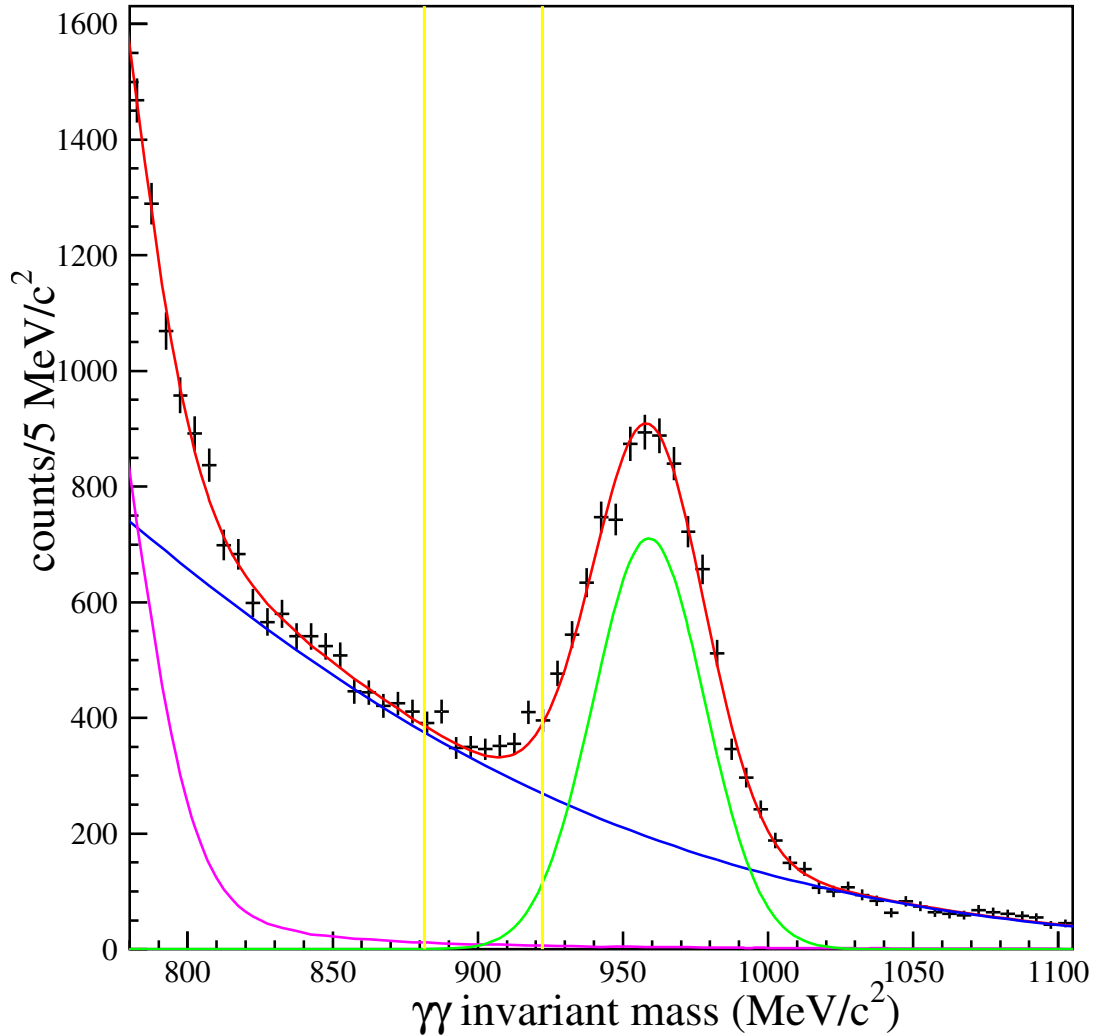


Figure 5.26: The spectral fit excluding a region $880 \leq M_{\gamma\gamma} < 920 \text{ MeV}/c^2$ after the cut to eliminate clusters with high leaked energies. The green, blue, and red lines show the quasi-free η' peak, the sum of smooth backgrounds from multi-meson photo-production etc. and ω photoproduction, and the sum of all components, respectively. The excluded region is shown by yellow lines.

Table 5.2: The obtained significance of the enhancement in individual mass regions after applying the cut to eliminate clusters with high leaked energies.

Mass region (MeV/c ²)	Significance
$870 \leq M_{\gamma\gamma} < 920$	3.0
$880 \leq M_{\gamma\gamma} < 920$	2.8
$890 \leq M_{\gamma\gamma} < 920$	2.6
$870 \leq M_{\gamma\gamma} < 930$	3.2
$880 \leq M_{\gamma\gamma} < 930$	2.9
$890 \leq M_{\gamma\gamma} < 930$	2.7
$900 \leq M_{\gamma\gamma} < 930$	2.6

Chapter 6

Discussions

In this chapter, possible modification of the η' mass and width in nuclear medium is discussed from the fit results. The spectral functions of in-medium modification signals using a simple model are introduced to confirm the statistical significance of the enhancement obtained in the previous chapter and to investigate whether the enhancement is explained by in-medium modification signals or not. Systematics checks of the obtained results are also described.

6.1 χ^2 difference test for the $\gamma\gamma$ spectra

The fit results of the $\gamma\gamma$ invariant mass spectra indicate an enhancement of low-mass components in the η' mass region for the low-momentum sample. In this section, we discuss whether the enhancement is explained by possible in-medium modifications of the η' mass spectrum by including a component of in-medium modification signals to the spectral fits. The significance of signals was also evaluated by comparing the χ^2 values of fits with and without in-medium signals. In Sec.6.1.1, spectral functions for in-medium η' signals are prepared with simple assumptions. The spectral fits including the signal functions are performed, and discussions on in-medium modification parameters are given in Sec.6.1.2.

6.1.1 Simulation of in-medium η' decay signals

To perform the line shape fit of the η' mass spectrum including the in-medium modification signals, the $\gamma\gamma$ invariant mass distributions of in-medium η' decay should be prepared reliably. The signal line shapes of η' decays inside a nucleus were generated by a MC simulation with the following conditions:

1. The η' meson was generated for the reaction $\gamma p \rightarrow \eta' p$ according to its differential cross section. The energy distribution of inverse Compton scattering was adopted for an incident photon beam.
2. The creation points of η' mesons are distributed in proportion to the nuclear density of Woods-Saxon type:

$$\rho(r) \propto [1 + \exp\{(r - R)/d\}]^{-1}, \quad (6.1)$$

where r is the distance from the center of a nucleus. R and d were set to 2.3 fm and 0.57 fm, respectively, for the carbon nucleus [15].

3. The generated η' propagates to a random direction in a nucleus by a step of $dl = 0.01$ fm, and decays with the probability of $\exp(-dl/L)$, where L is the decay length determined by the total decay width Γ_{tot} . The decay length is modified for each step along with the Eqs. (6.1) and (6.3) as described in the following item 5.
4. The η' decays into $\gamma\gamma$ with the branching ratio of $\Gamma_{\gamma\gamma}/\Gamma_{\text{tot}}$, where $\Gamma_{\gamma\gamma}$ is the partial decay width of $\eta' \rightarrow \gamma\gamma$ in vacuum. It was assumed that $\Gamma_{\gamma\gamma}$ should be unchanged inside a nucleus.
5. At individual steps during the propagation, the mass $m_{\eta'}$ and the total decay width Γ_{tot} were assumed to be modified in a nucleus as a function of the density ρ by

$$m_{\eta'}(\rho) = m_0 \left(1 - k_1 \frac{\rho}{\rho(0)} \right) \quad (6.2)$$

$$\Gamma_{\text{tot}}(\rho) = \Gamma_0 \left(1 + k_2 \frac{\rho}{\rho(0)} \right), \quad (6.3)$$

where $m_0 = 957.8 \text{ MeV}/c^2$, $\Gamma_0 = 0.197 \text{ MeV}$ [1] are the mass and width of η' in vacuum, respectively. The coefficients k_1 and k_2 are variable input parameters corresponding to the mass reduction and the width broadening, respectively. Signal shape simulations were done with various combinations of k_1 and k_2 , as described later. The mass of η' at the decay point was determined from the Breit-Wigner distribution with the mass $m_{\eta'}(\rho)$ and the width $\Gamma_{\text{tot}}(\rho)$ described above.

6. The $\gamma\gamma$ invariant mass was reconstructed by using BGOegg with a realistic energy resolution.

To extract the $\gamma\gamma$ invariant mass distribution of in-medium decays, a nucleus volume was defined by weighting the decay points with the nuclear density, Eq. (6.1). The parameters k_1 and k_2 were fixed for each simulation sample. The samples were generated for k_1 with every 0.01 step from 0.02 to 0.15. Then, $k_2 = 50, 125, 250, 500, 1000$ were combined for individual setting of k_1 . Figures 6.1–6.10 show the simulated $\gamma\gamma$ invariant mass distributions of in-medium decay signals for all the input combinations of k_1 and k_2 parameters. Figures 6.1–6.5 correspond to the samples with the low-momentum region of $P_{\gamma\gamma} \leq 1 \text{ GeV}/c$, and Figures 6.6–6.10 correspond to those with the high-momentum region of $P_{\gamma\gamma} > 1 \text{ GeV}/c$. The distribution becomes broad as k_1 increases because the mass at decay points varies in the range of m_0 and $m_0(1 - k_1)$ according to the nuclear density distribution.

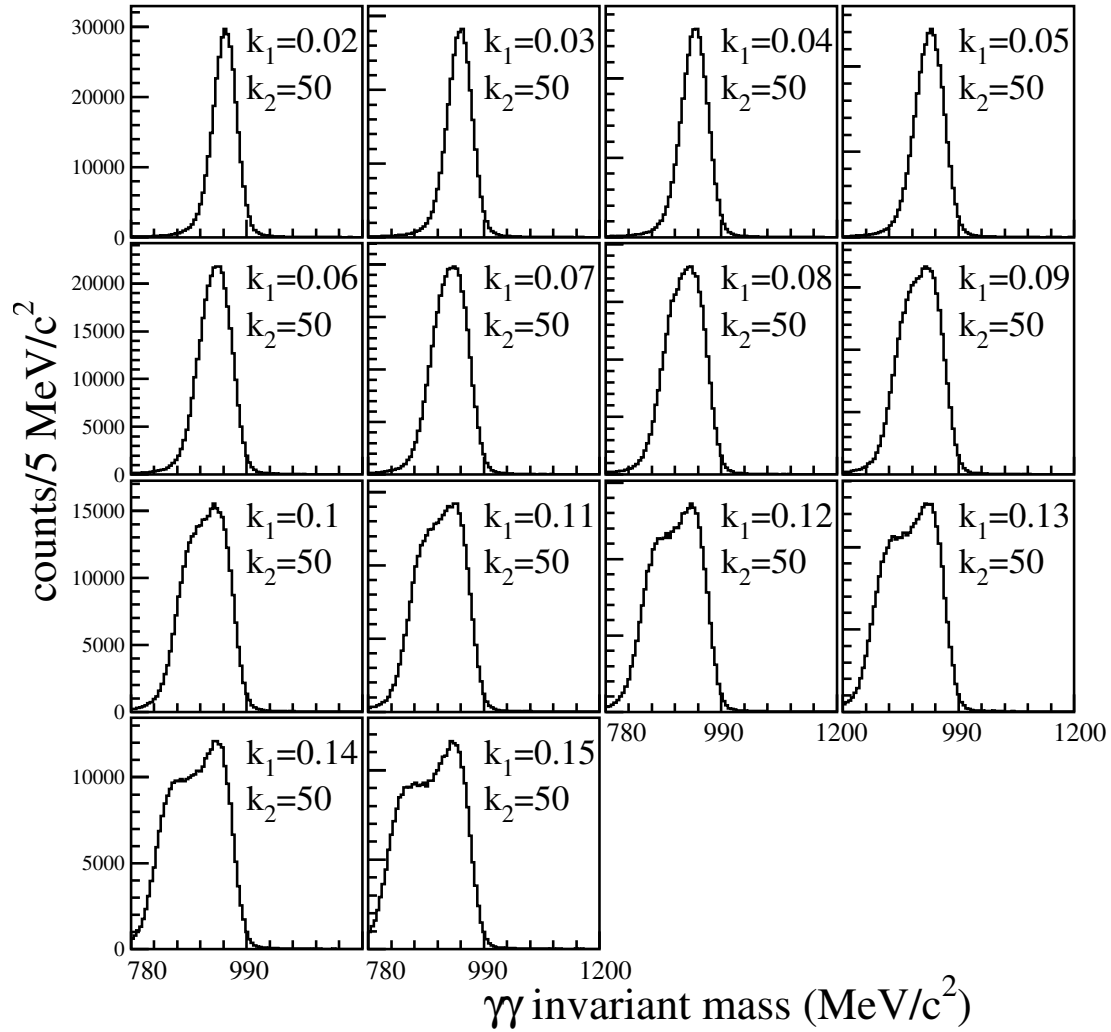


Figure 6.1: The simulated spectra of in-medium η' decays for $P_{\gamma\gamma} \leq 1 \text{ GeV}/c$. The cases of $k_2 = 50$ are shown.

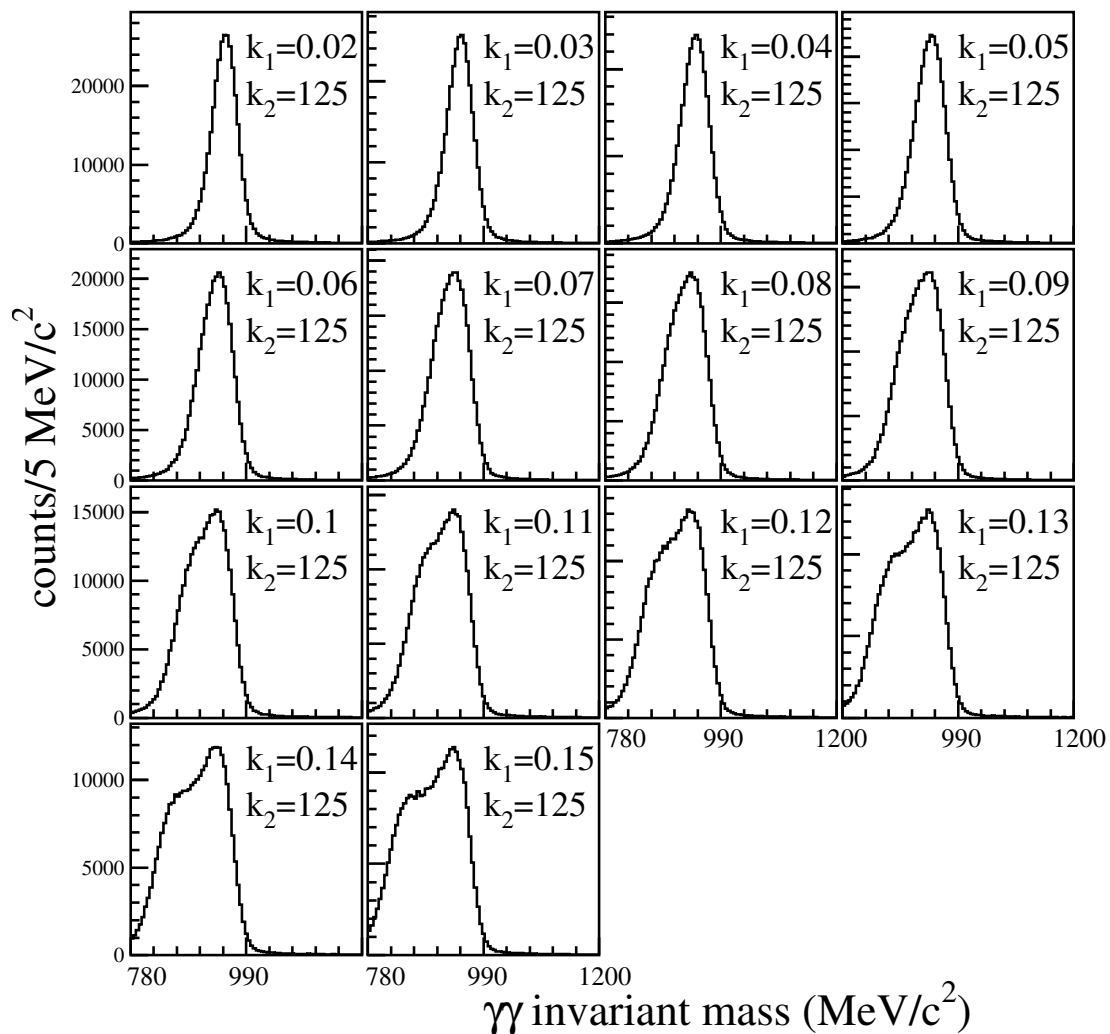


Figure 6.2: The simulated spectra of in-medium η' decays for $P_{\gamma\gamma} \leq 1 \text{ GeV}/c$. The cases of $k_2 = 125$ are shown.

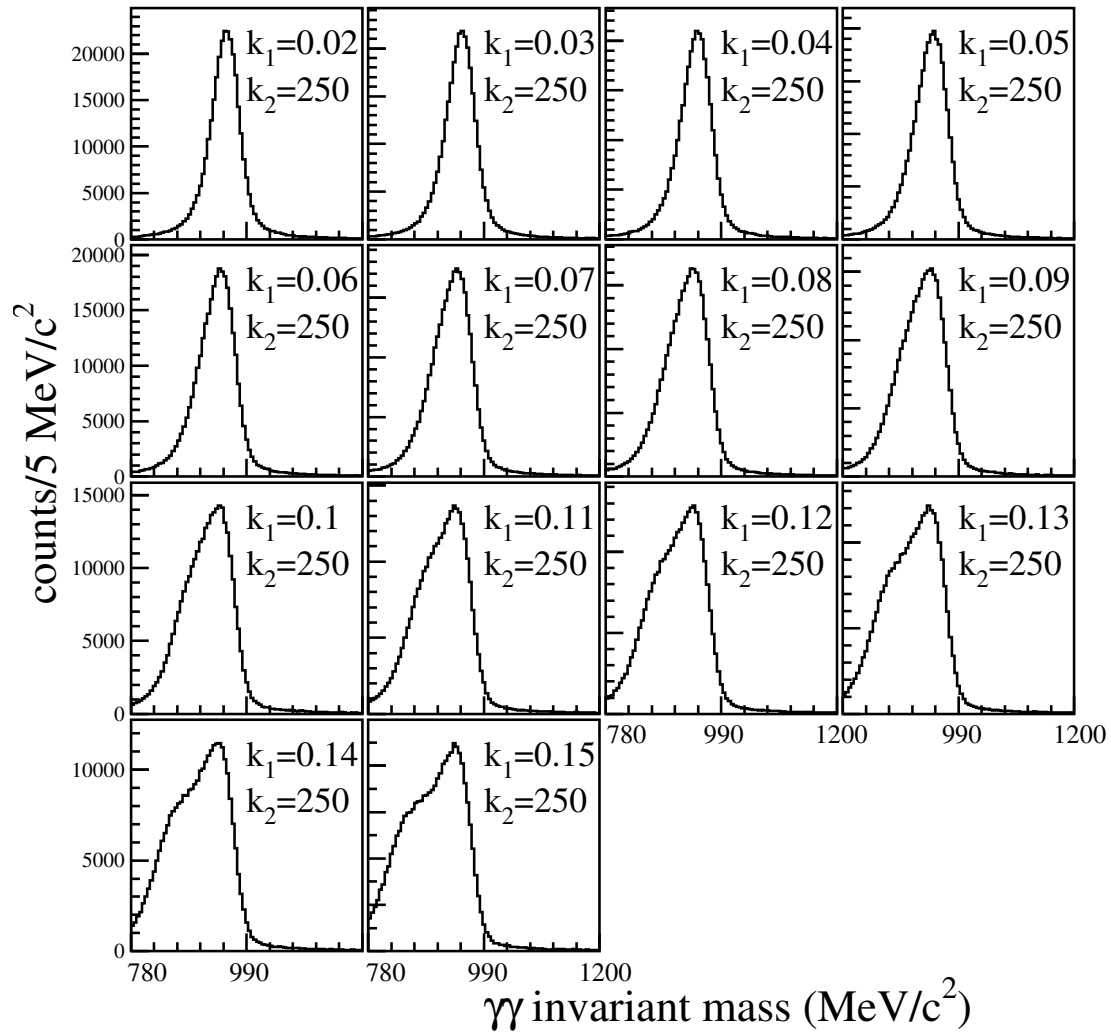


Figure 6.3: The simulated spectra of in-medium η' decays for $P_{\gamma\gamma} \leq 1 \text{ GeV}/c$. The cases of $k_2 = 250$ are shown.

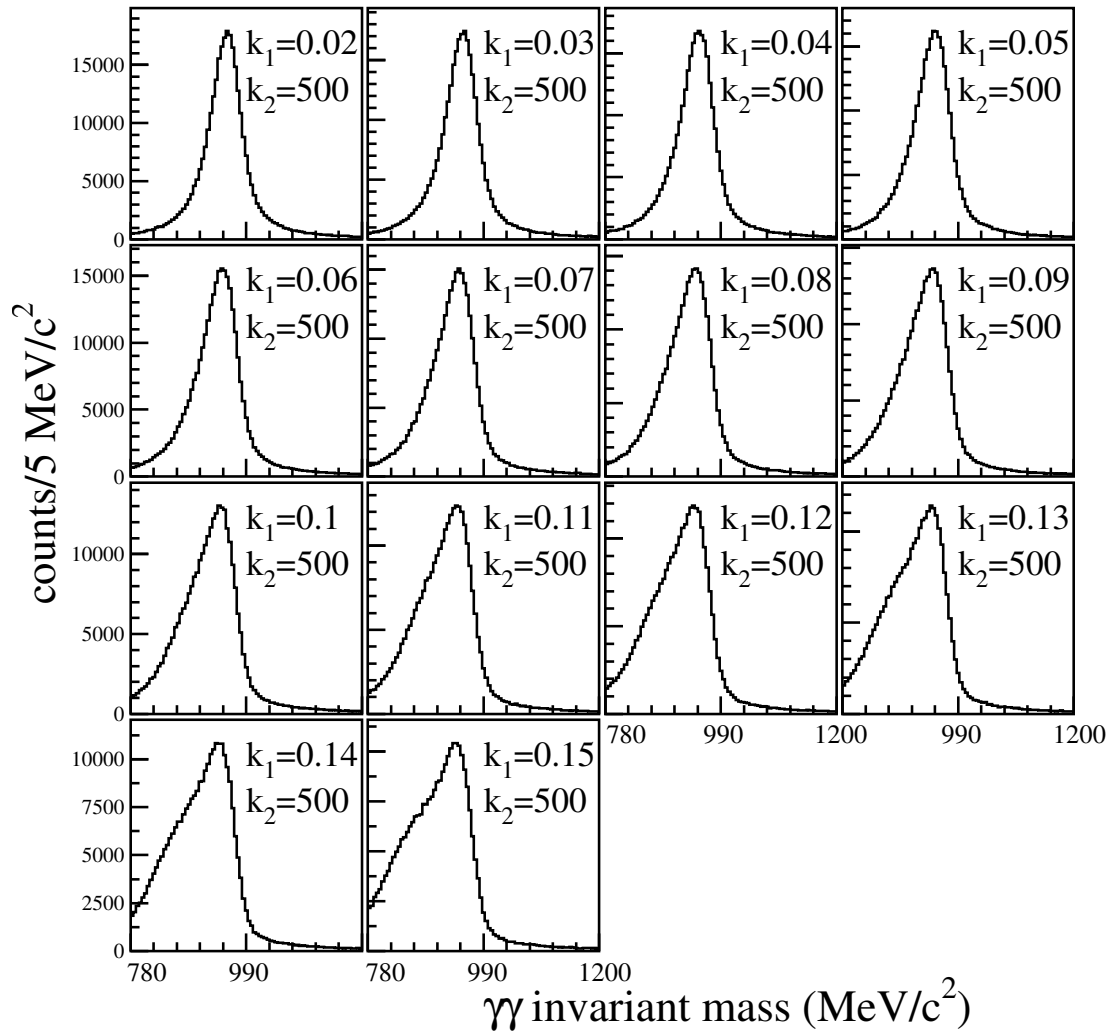


Figure 6.4: The simulated spectra of in-medium η' decays for $P_{\gamma\gamma} \leq 1$ GeV/c. The cases of $k_2 = 500$ are shown.

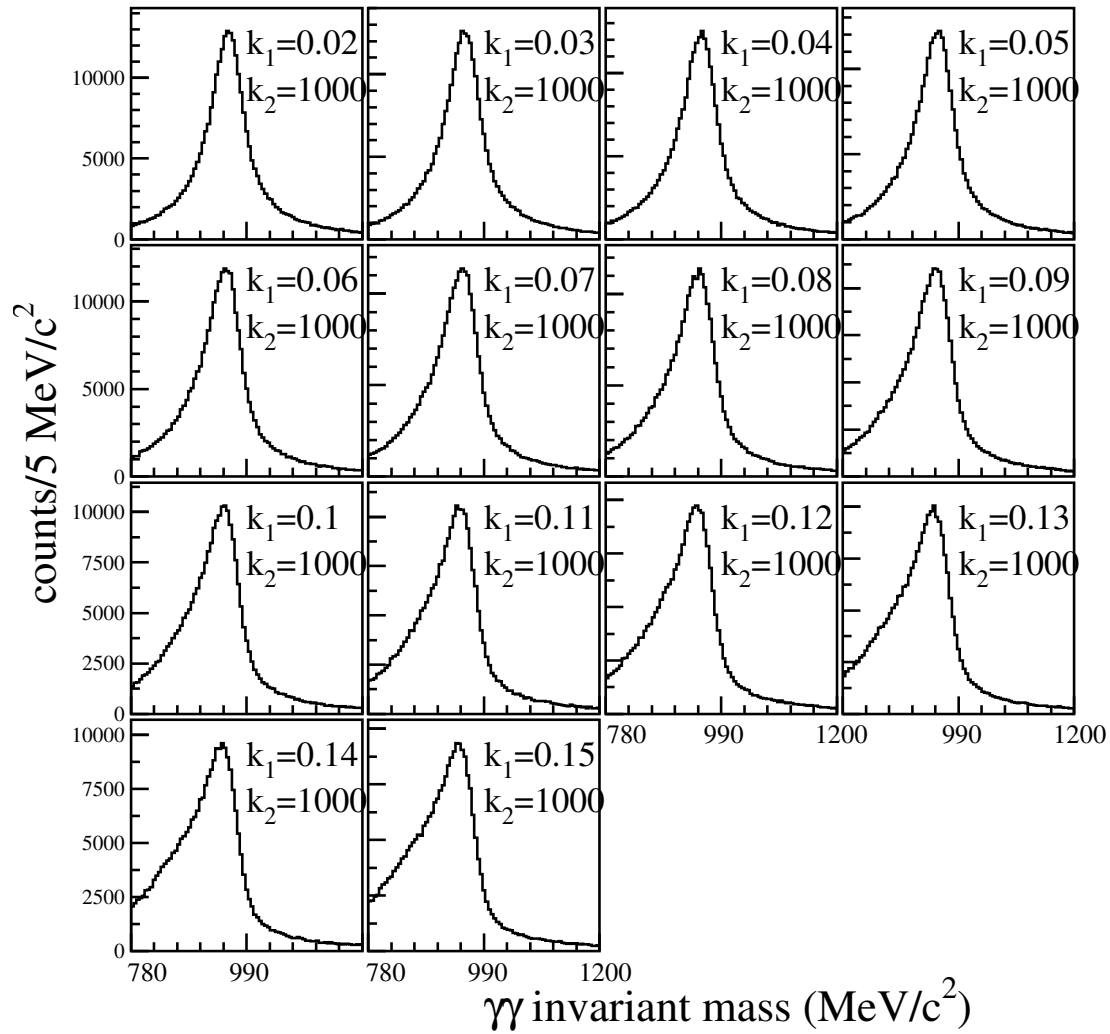


Figure 6.5: The simulated spectra of in-medium η' decays for $P_{\gamma\gamma} \leq 1 \text{ GeV}/c$. The cases of $k_2 = 1000$ are shown.

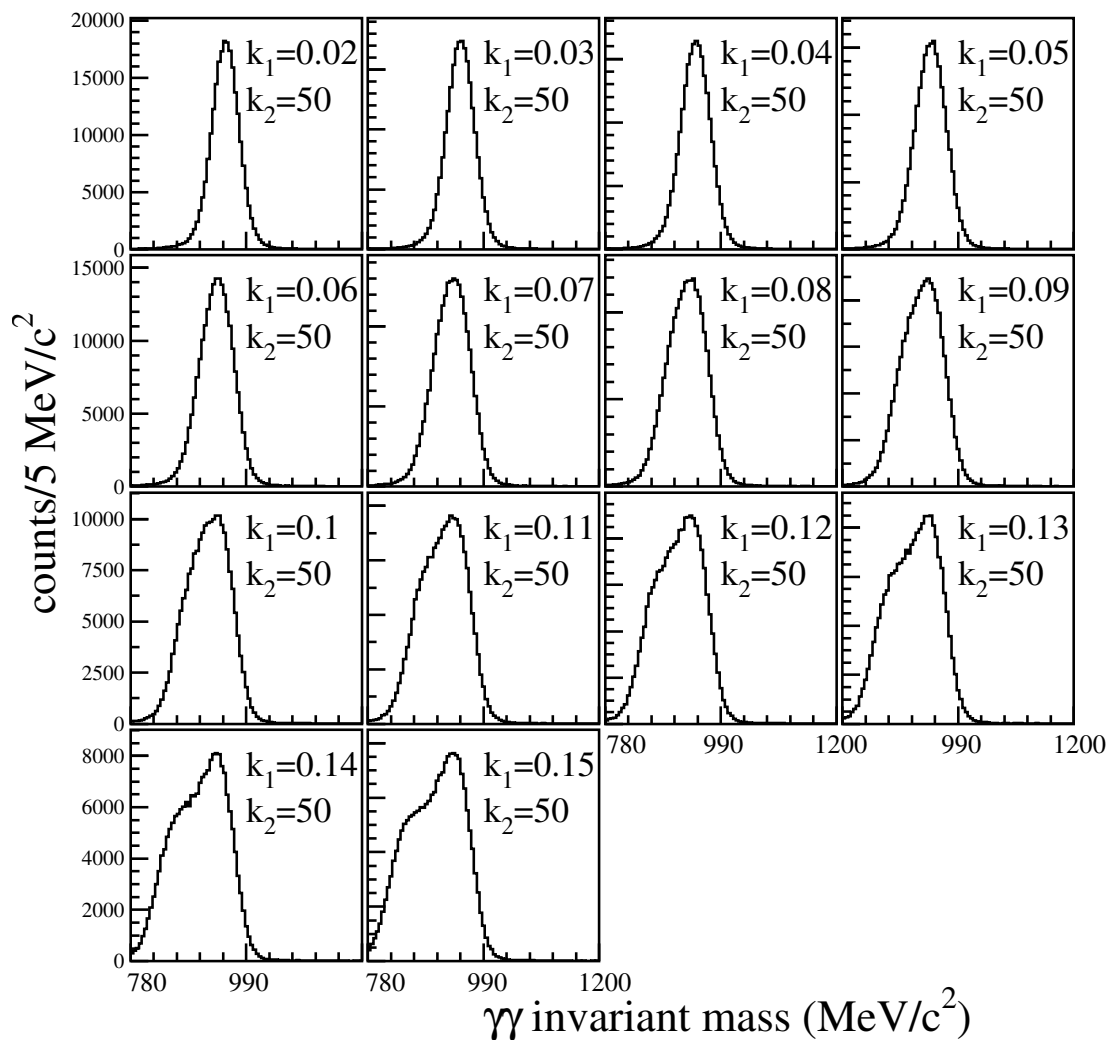


Figure 6.6: The simulated spectra of in-medium η' decays for $P_{\gamma\gamma} > 1$ GeV/c. The cases of $k_2 = 50$ are shown.

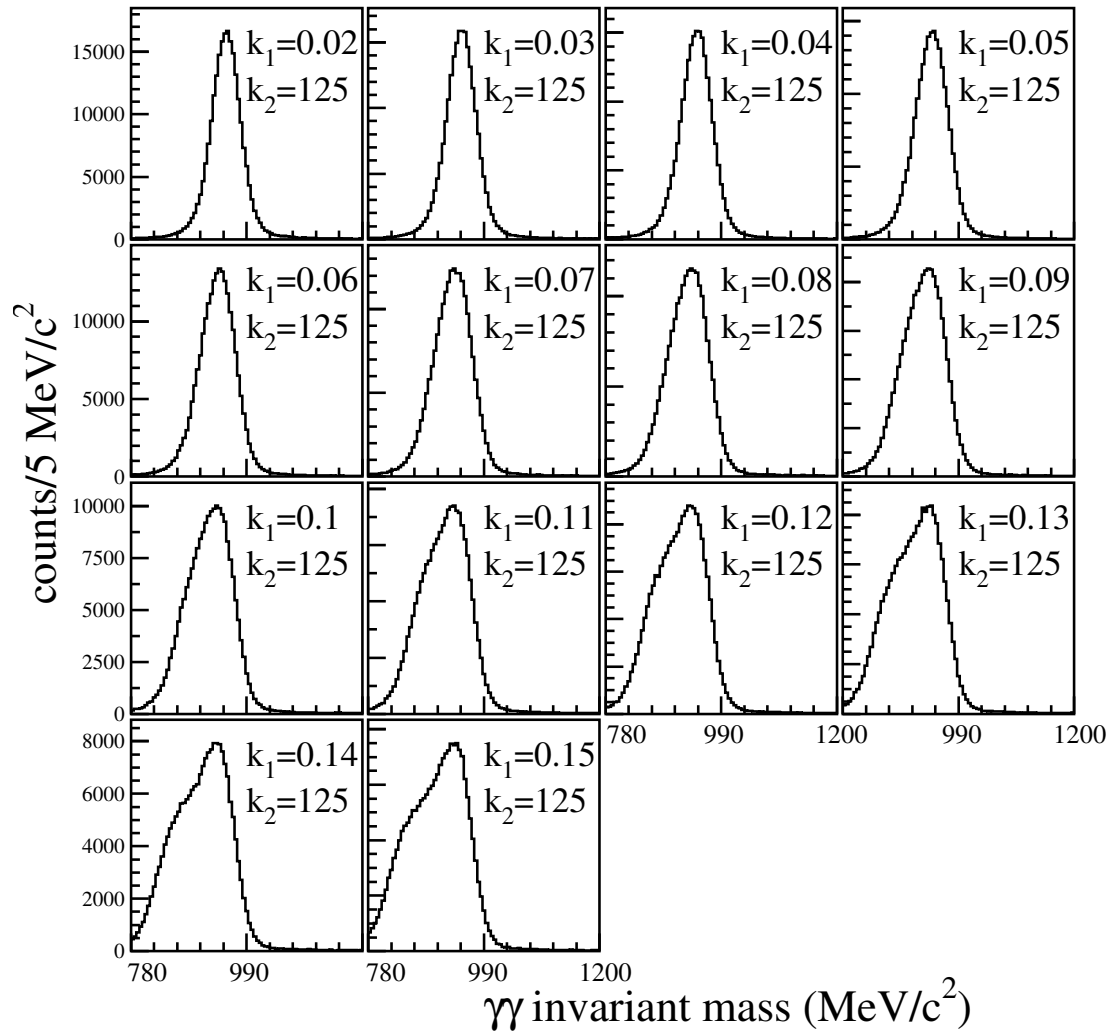


Figure 6.7: The simulated spectra of in-medium η' decays for $P_{\gamma\gamma} > 1 \text{ GeV}/c$. The cases of $k_2 = 125$ are shown.

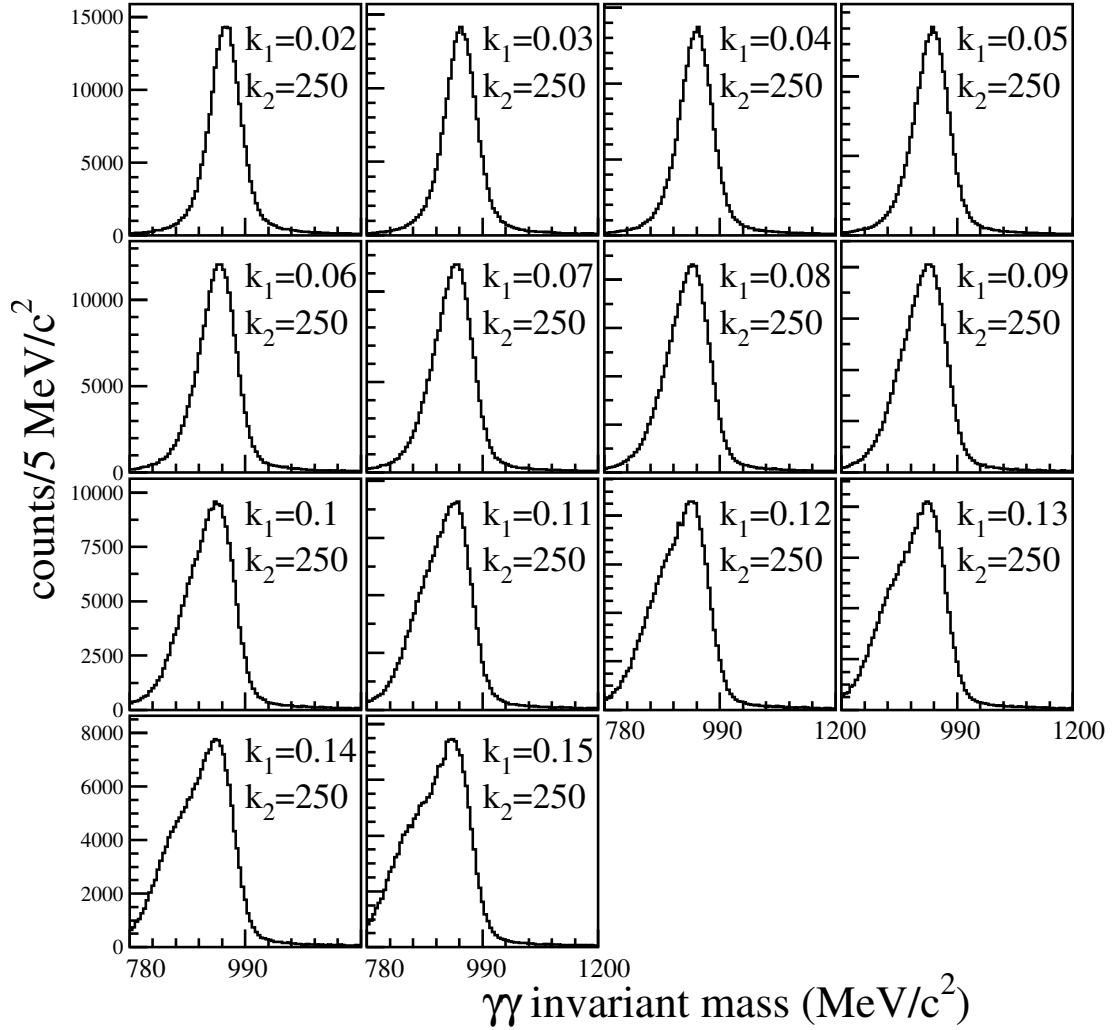


Figure 6.8: The simulated spectra of in-medium η' decays for $P_{\gamma\gamma} > 1 \text{ GeV}/c$. The cases of $k_2 = 250$ are shown.

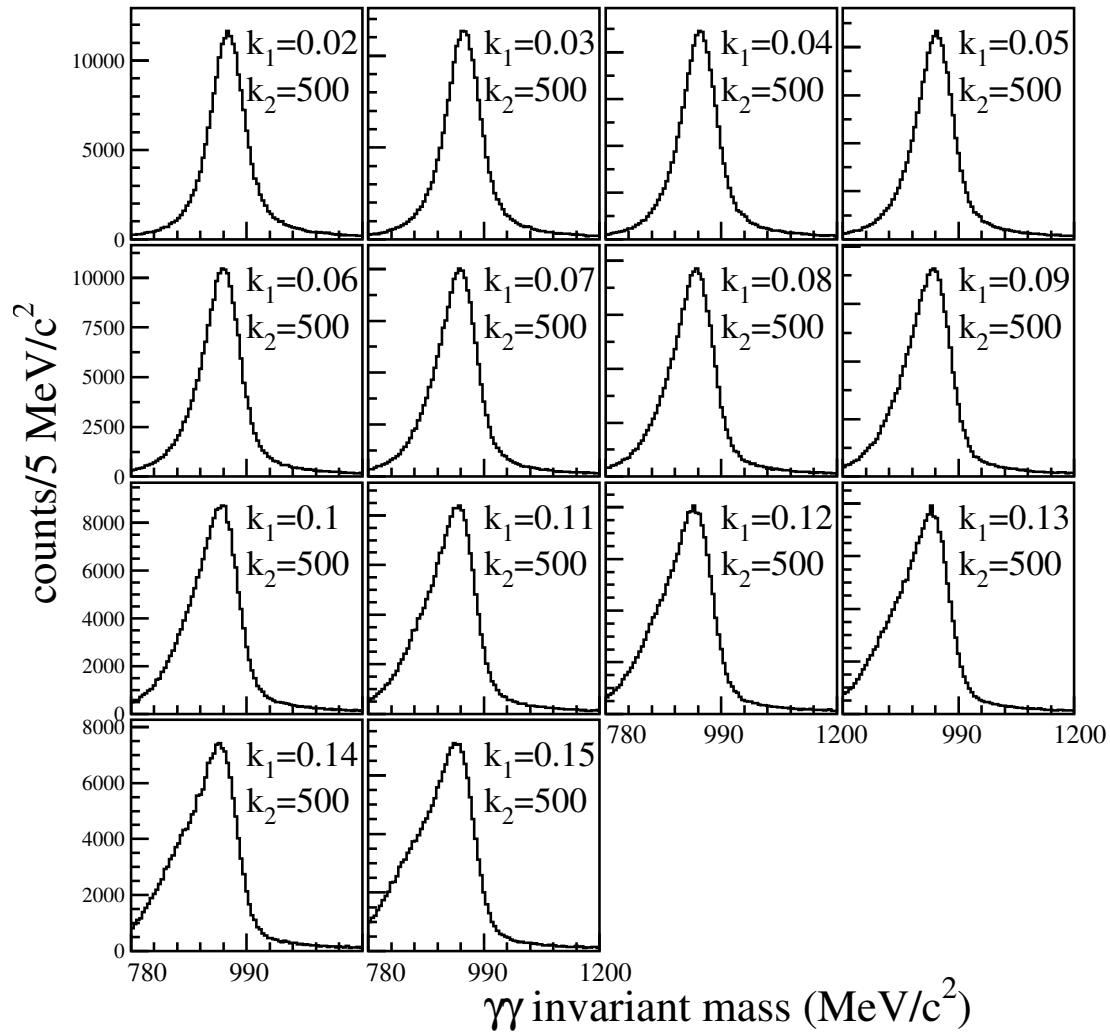


Figure 6.9: The simulated spectra of in-medium η' decays for $P_{\gamma\gamma} > 1 \text{ GeV}/c$. The cases of $k_2 = 500$ are shown.

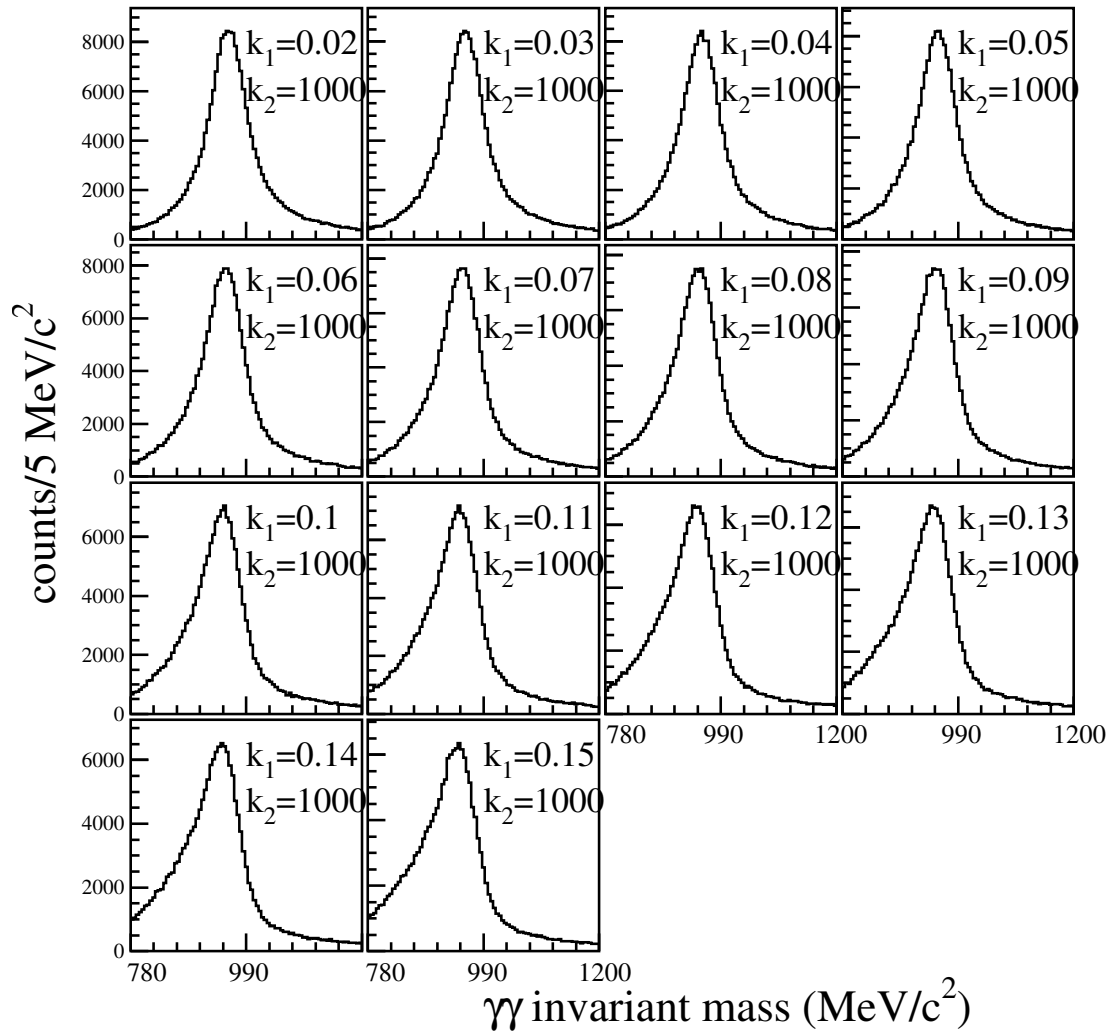


Figure 6.10: The simulated spectra of in-medium η' decays for $P_{\gamma\gamma} > 1 \text{ GeV}/c$. The cases of $k_2 = 1000$ are shown.

6.1.2 Fit results including in-medium modification signals

The function to be fitted is as follows:

$$F_{\gamma\gamma}(x) = \alpha_1 \{F_\omega(x) + \exp(p_0 + p_1x + p_2x^2 + p_3x^3)\} + \alpha_2 \exp\left\{\frac{-(x - \mu)^2}{2\sigma_{\text{QF}}^2}\right\} + \alpha_{\text{sig}} F_{\text{sig}}(x; k_1, k_2). \quad (6.4)$$

The first and second term are same as Eq. (5.3). $F_{\text{sig}}(x; k_1, k_2)$ in the final term is the simulated signal distribution of in-medium η' decays with fixed parameters k_1 and k_2 as described in the previous subsection. α_{sig} is the additional fitting parameter. In order to evaluate the statistical significance of the in-medium mass modification signals, the fit of Eq. (6.4) was performed in two cases: including the signal function where α_{sig} was treated as a free parameter, or excluding the signal function where α_{sig} was fixed to 0. Then, the results of two fits were compared to discuss a signal significance. Note that the degree of freedom ndf in the fit of former case is one less than that of the latter fit. In the case of including a signal function, the spectral fit was performed for each value of k_1 with every 0.01 step from 0.02 to 0.15 and for $k_2 = 50, 125, 250, 500, 1000$. A calculation of the signal significance was done from the difference of χ^2 in the fits with and without the signal function. Fitting without the signal function corresponds to minimizing χ^2 under the constraint of $\alpha_{\text{sig}} = 0$. The difference of χ^2 , $\Delta\chi^2$, should follow the chi-square distribution with the degree of freedom which equals $\Delta ndf = 1$. Thus, the significance is evaluated based on the cumulative probability of a chi-square distribution:

$$P_{\chi^2}(x, \Delta ndf = 1) = \int_x^\infty \chi^2(t, \Delta ndf = 1) dt, \quad (6.5)$$

where $\chi^2(t, \nu)$ is the probability density function of a chi-square distribution with ν degrees of freedom. The statistical significance is defined by a standard deviation of Gaussian distribution, σ , corresponding to the probability that the values above $\Delta\chi^2$ are accidentally obtained, $P_{\chi^2}(\Delta\chi^2, \Delta ndf = 1)$.

For the low-momentum sample, an example of the fit including the signal function is shown in Fig. 6.11, where k_1 and k_2 parameters are chosen to be 0.06 and 125, respectively. Similar fits with variations of k_1 and k_2 were performed to get χ^2 's.

Figure 6.12 shows the χ^2 values of the fits including the signal functions. The left and right panels show the parameter dependence of χ^2 for the low-momentum and high-momentum samples, respectively. In addition, the red straight lines show the reference χ^2 values in the case of fitting only background function. By including signal functions, χ^2 values become much better for the low-momentum sample while no significant difference appears for the high-momentum sample. The corresponding significance is shown in Fig. 6.13. The difference of χ^2 's between the two fits with and without a signal function reaches the maximum value of $\Delta\chi^2 = 12.6$ at $k_1 = 0.06$ and $k_2 = 125$, which corresponds to the significance of 3.7σ .

The obtained significance is not very large. However, the fit result indicates that the $\gamma\gamma$ invariant mass spectrum for the low-momentum sample can be expressed reasonably by including the in-medium modification signals with the appropriate parameters of k_1 and k_2 . On the other hand, the signal significance for the high-momentum sample is small enough to be understood as statistical fluctuations for any k_1 and k_2 parameters. In addition, the significance obtained by this χ^2 difference test is consistent with that obtained by the fits without signal functions, described in the previous section. Furthermore, a large drop of χ^2 is seen depending on the k_1 and k_2 parameters. This means a specific value of k_1 and k_2 reasonably reproduces the obtained $\gamma\gamma$ spectrum.

Figure 6.14 shows the map of $\Delta\chi^2$ relative to the minimum value in the k_1 - k_2 space for the low-momentum sample. Standard deviations for the k_1 and k_2 parameters were determined by finding their values when $\Delta\chi^2$ was increased by 1 from the minimum value. The area by a deep blue color is the most favored region of k_1 and k_2 within 1σ . We obtained the parameter k_1 in the range of 0.04–0.07, corresponding to the mass reduction of $\Delta m = 38$ – 67 MeV/ c^2 . In addition, the parameter range of $k_2 < 300$ was obtained as a 1σ region, limiting the width broadening $\Delta\Gamma_{\text{tot}}$ to the value less than 60 MeV. Unfortunately, there is no sensitivity to restrict k_2 further in the region below 300 due to the mass resolution of BGOegg.

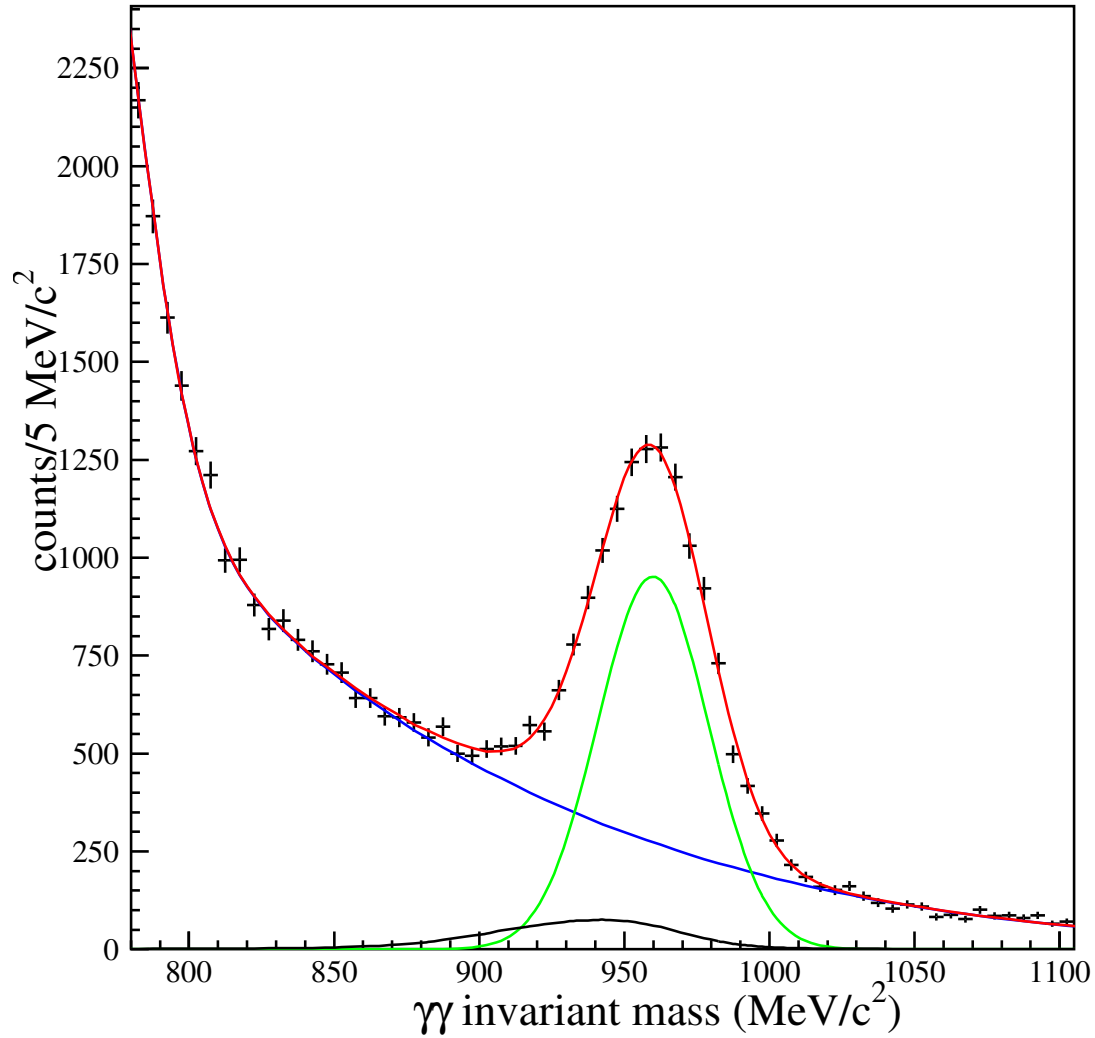


Figure 6.11: An example of the fit including a signal function for the low-momentum sample. The green, blue, black, and red lines show the quasi-free η' peak, the sum of smooth backgrounds from multi-meson photoproduction etc. and ω photoproduction, the signal function, and the sum of all components, respectively. $k_1 = 0.06$ and $k_2 = 125$ were used for the signal function.

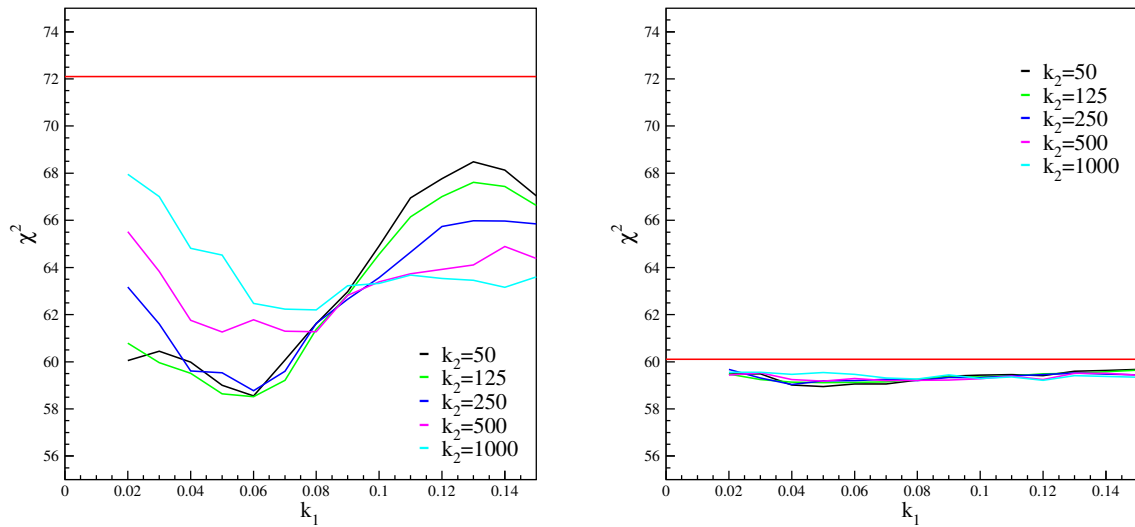


Figure 6.12: The χ^2 values of fits including the signal functions with various k_1 and k_2 parameters. The left and right panels show the low-momentum and high-momentum samples, respectively. The χ^2 values of fits without signal functions are shown by red lines.

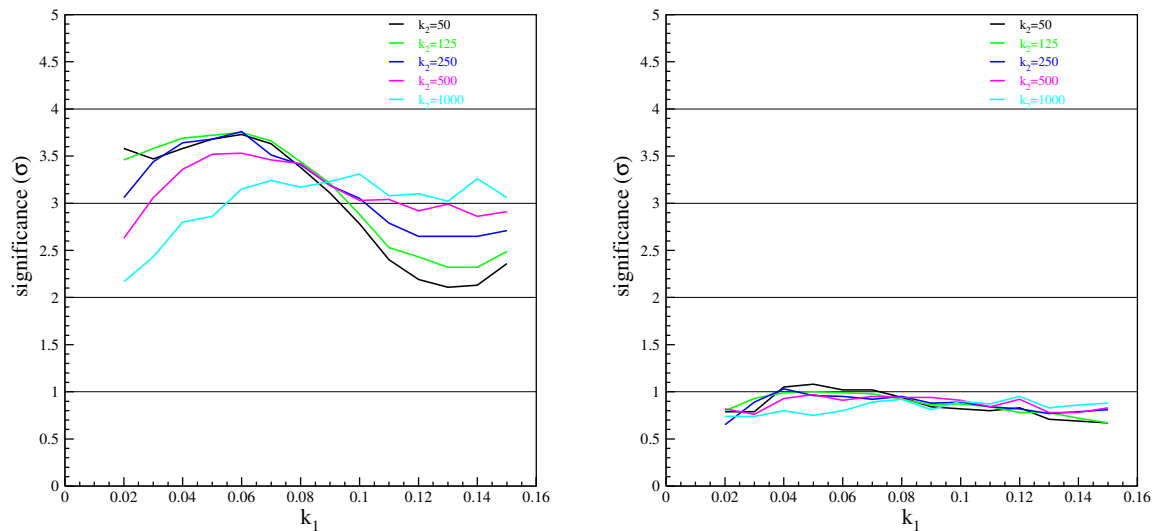


Figure 6.13: The significance of in-medium signals with various k_1 and k_2 parameters. The left and right panels show the low-momentum and high-momentum samples, respectively.

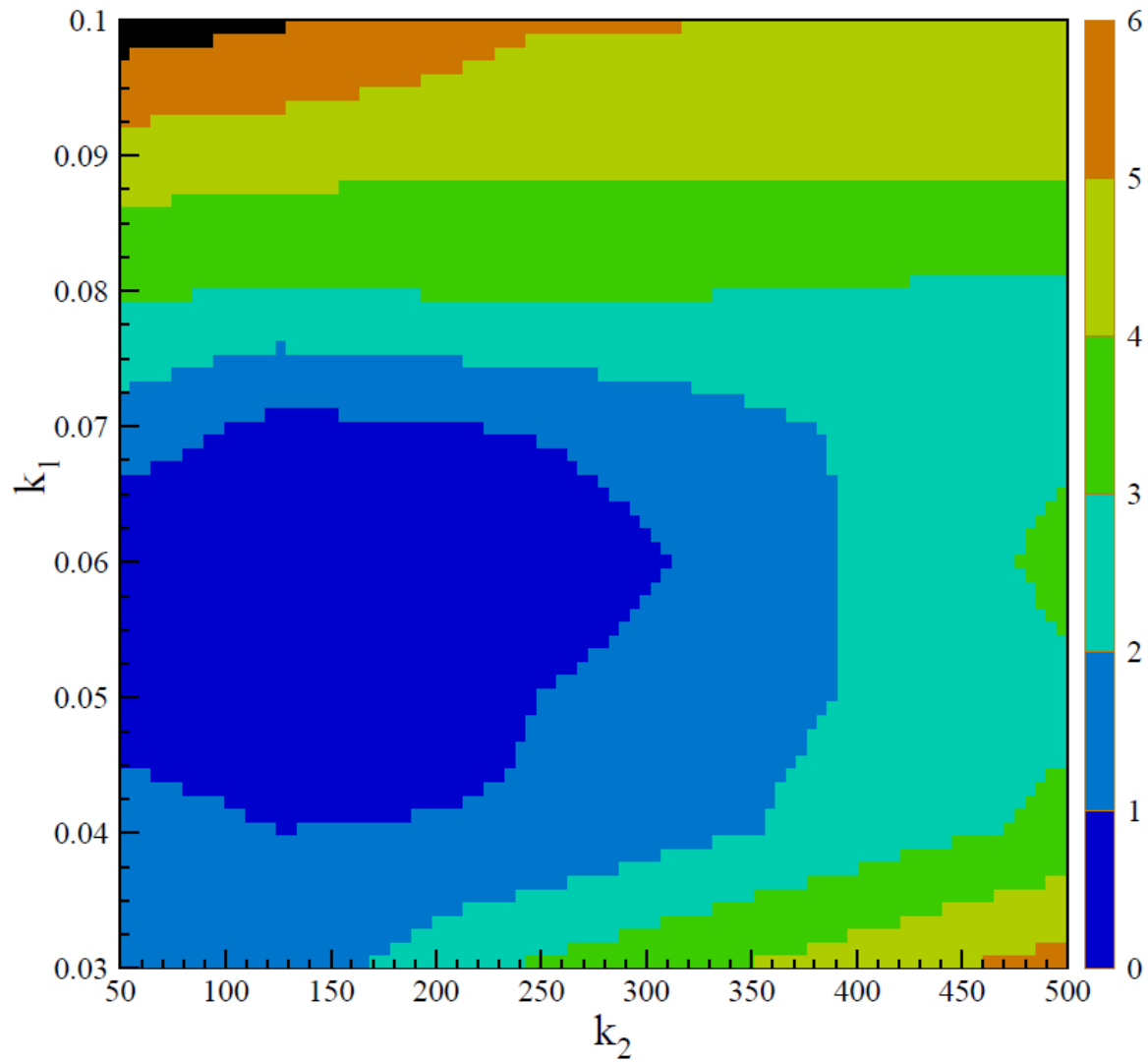


Figure 6.14: The map of $\Delta\chi^2$ relative to the minimum value in the k_1 - k_2 space. The $\Delta\chi^2$ scale by different colors is shown in the right-hand side.

6.2 Systematic studies

6.2.1 Analysis for the proton target data

In order to test the analysis procedure by using another independent sample, η' photoproduction events from a proton target, which were collected in a different experimental period, were also analyzed. The analysis conditions described in Chapter 4 were applied to the proton target data. The background distribution from ω photoproduction and the momentum-dependent mass resolutions of a quasi-free η' peak were additionally simulated with a setup of the liquid hydrogen target. Note that the mass resolutions become worse because of a longer length of the liquid hydrogen target. Figure 6.15 shows a $\gamma\gamma$ spectrum of the proton target data with $P_{\gamma\gamma} \leq 1$ GeV/c. The function (6.4) was fitted to the $\gamma\gamma$ spectrum as well, in the two cases with and without the signal function. The spectrum was well reproduced by the fit without the signal function, resulting in $\chi^2/ndf = 26.0/26$. Figure 6.16 shows the χ^2 values of the fits (left panel) and the signal significance (right panel) with various signal functions, which are simulated in the same way as the carbon target case. There was no significant difference between the two cases with and without the signal functions. In addition, the signal significance was small consistent with the statistical fluctuations for any k_1 and k_2 parameters.

6.2.2 χ^2 difference test with another signal function

For the χ^2 difference test described in Sec.6.1, we used in-medium signal functions obtained by a MC simulation, which depends on the conditions described in Sec.6.1.1. To examine the effect by variation of signal functions, a χ^2 difference test was performed using a Gaussian function as another signal function. The function to be fitted to the $\gamma\gamma$ spectrum is as follows:

$$F_{\gamma\gamma}(x) = \alpha_1 \{F_\omega(x) + \exp(p_0 + p_1x + p_2x^2 + p_3x^3)\} + \alpha_2 \exp\left\{\frac{-(x - \mu)^2}{2\sigma_{\text{QF}}^2}\right\} + \alpha_{\text{sig}} \exp\left\{\frac{-(x - \mu_{\text{sig}})^2}{2\sigma_{\text{sig}}^2}\right\}. \quad (6.6)$$

The first and second term are same as Eq.(6.4). The final term was used as a signal function instead of $\alpha_{\text{sig}}F_{\text{sig}}(x; k_1, k_2)$ in Eq.(6.4). Three parameters α_{sig} , μ_{sig}

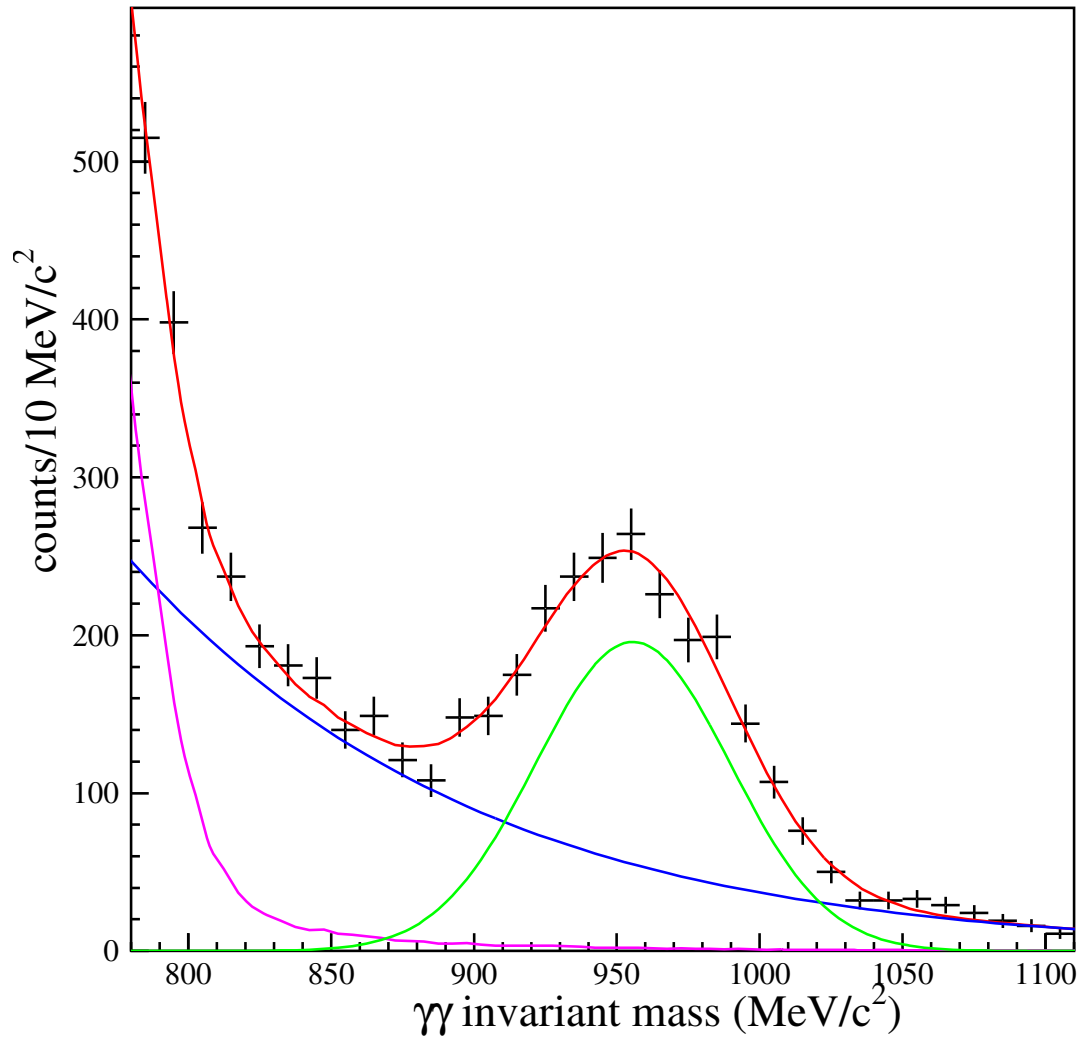


Figure 6.15: The $\gamma\gamma$ invariant mass spectrum in the momentum region below 1 GeV/c for the proton target data. Fitting results are overlaid in the same panel. The green, blue, magenta, and red lines show the quasi-free η' peak, the smooth backgrounds, the background from ω photoproduction, and the sum of all components, respectively.

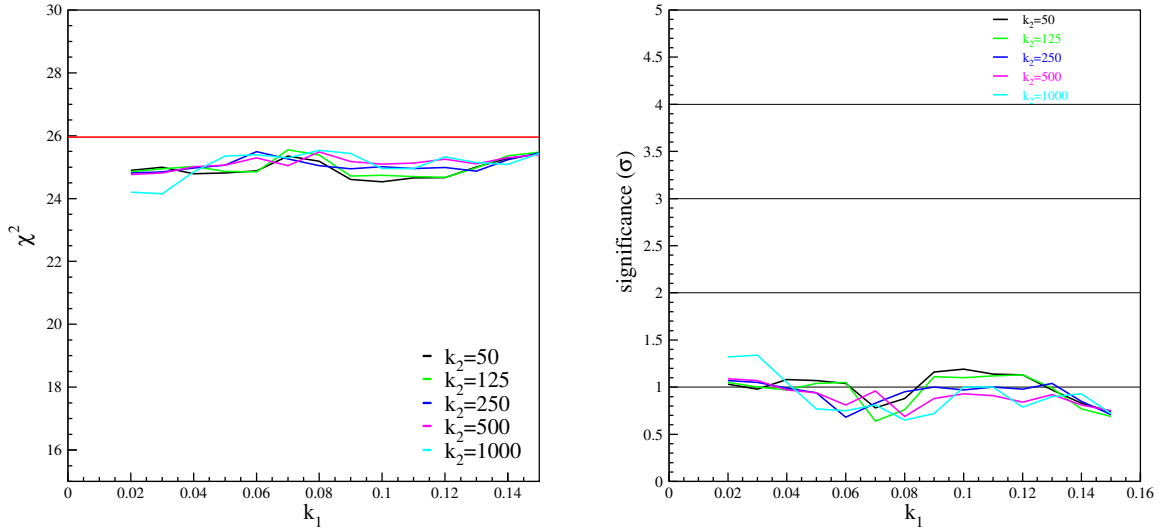


Figure 6.16: The χ^2 of fits for the proton target data including the signal functions (left) and the obtained signal significance (right) with various k_1 and k_2 parameters. The χ^2 values of a fit without a signal functions is shown by a straight red line.

and σ_{sig} were treated as free parameters. The χ^2 difference test was performed in the same way as described in Sec.6.1.2. The difference of χ^2 's between the fits with and without a signal function, $\Delta\chi^2$, should follow the χ^2 distribution with the degree of freedom which equals $\Delta ndf = 3$ under the hypothesis that there are no in-medium signals.

Figure 6.17 shows the fit result including the Gaussian signal function for the low-momentum sample. $\mu_{\text{sig}} = 919 \pm 10 \text{ MeV}/c^2$ and $\sigma_{\text{sig}} = 24 \pm 6 \text{ MeV}/c^2$ were obtained from the fit. The χ^2 difference between the fits with and without a signal function was obtained to be $\Delta\chi^2 = 16.2$, which corresponds to the significance of 3.3σ . This value is consistent with those obtained in Secs. 5.4.2 and 6.1.2. The enhancement in the $\gamma\gamma$ spectrum for the low-momentum sample was consistently confirmed in this analysis. This result means that the signal significance evaluated by the χ^2 difference test does not largely depend on the assumed signal function.

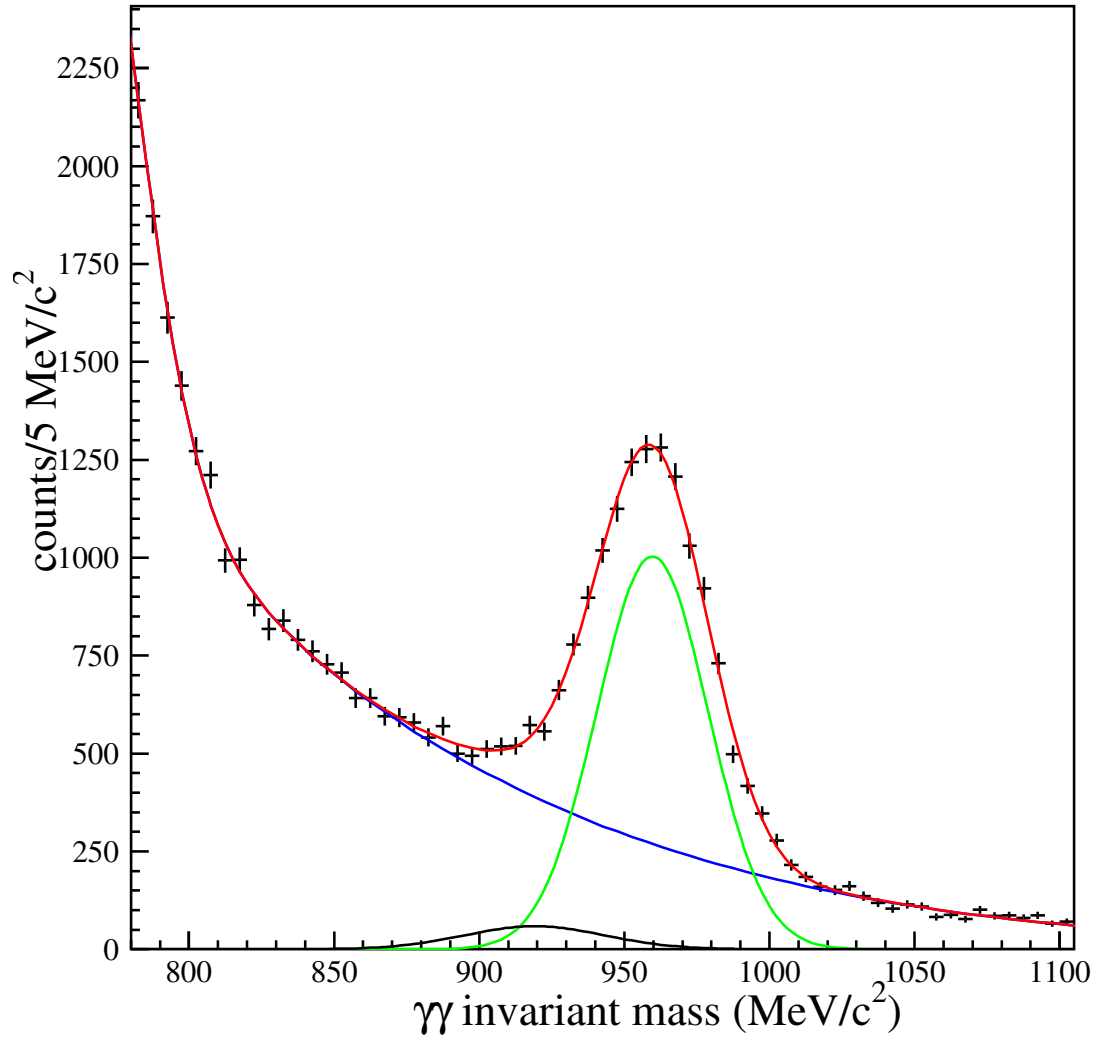


Figure 6.17: The result of the fit including a Gaussian signal function for the low-momentum sample. The green, blue, black, and red lines show the quasi-free η' peak, the sum of smooth backgrounds from multi-meson photoproduction etc. and ω photoproduction, the Gaussian signal function, and the sum of all components, respectively.

6.2.3 Other systematic studies

In order to check the effect by variation of the fitting conditions, spectral fits were performed with different forms of the background functions.

The mass resolution of quasi-free η' peaks, σ_{QF} in Eq. 6.4, was deviated by ± 0.1 MeV/ c^2 , corresponding to $\pm 5\sigma$ variation from the determined values of σ_{QF} . Other conditions are same as described in Sec. 6.1.2. Figures 6.18 and 6.19 show the obtained significance of in-medium signals from the fits for the low-momentum sample with the variation of mass resolutions by $+0.1$ and -0.1 MeV/ c^2 , respectively.

In order to check the validity of fixed σ_{QF} , fitting results without signal functions were compared between the cases that σ_{QF} was fixed and treated as a free parameter. The fitting results of free σ_{QF} were 19.5 ± 0.4 and 22.0 ± 0.5 MeV/ c^2 for the low-momentum sample and the high-momentum sample, respectively. They are consistent with the fixed values of σ_{QF} determined by a MC simulation: $\sigma_{\text{QF}}=19.2$ and 22.5 MeV/ c^2 for the low-momentum sample and the high-momentum sample, respectively.

For another test of systematic variation, a different function form with a polynomial order lower than that of Eq. 5.2 was used as the smooth background function:

$$F_{M(\gamma\gamma)}(x) = \exp(p_0 + p_1x + p_2x^2), \quad (6.7)$$

where p_0 , p_1 , p_2 are fitting parameters. Figure 6.20 show the obtained significance of in-medium signals from the fits for the low-momentum sample by using the above background function. In either case, there is no significant difference from the result in Fig. 6.13. Thus, these variation of fit conditions have little effect on the line shape analysis of $\gamma\gamma$ mass spectrum.

6.3 Further discussions

Since the amount of in-medium decays should increase for lower $\gamma\gamma$ momenta or shorter decay lengths, the momentum dependence of the in-medium signals in the $\gamma\gamma$ spectrum was checked more in detail. The sample was divided into five regions of the $\gamma\gamma$ momentum: 300–700, 700–900, 900–1100, 1100–1300, 1300–1700 MeV/ c . The amount of in-medium signals was determined by fitting the function (6.4) to the

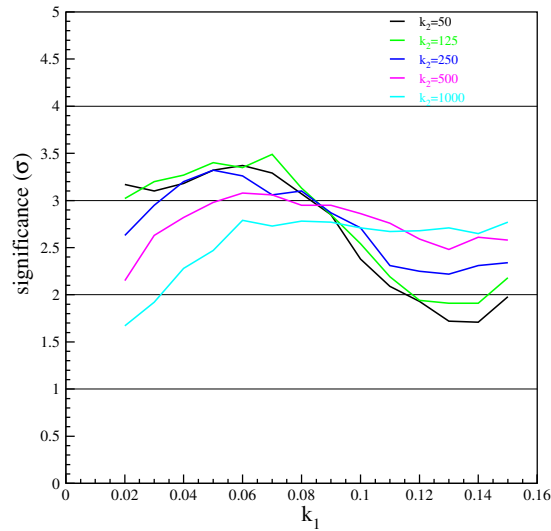


Figure 6.18: The significance of in-medium signals with various k_1 and k_2 parameters for the low-momentum sample. The mass resolution of the quasi-free η' peak was changed by $+0.1 \text{ MeV}/c^2$ from the determined value.

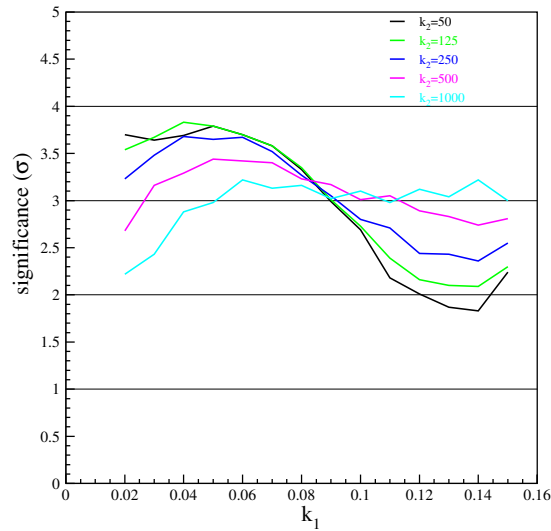


Figure 6.19: The significance of in-medium signals with various k_1 and k_2 parameters for the low-momentum sample. The mass resolution of the quasi-free η' peak was changed by $-0.1 \text{ MeV}/c^2$ from the determined value.

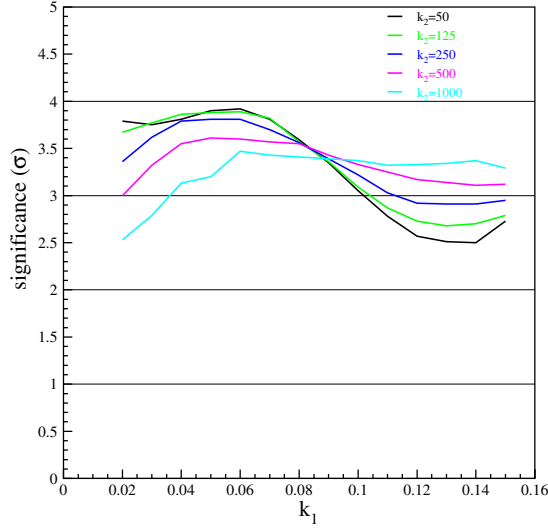


Figure 6.20: The significance of in-medium signals with various k_1 and k_2 parameters for the low-momentum sample by using a different background function in the form of Eq. 6.3.

$\gamma\gamma$ invariant mass spectrum in each momentum region with the signal functions of $k_1 = 0.06$ and $k_2 = 125$, where the maximum significance was obtained. Figures 6.21–6.25 show the $\gamma\gamma$ invariant mass spectra of individual momentum regions with the fit results. Figure 6.26 shows the momentum dependence of the ratio of the in-medium modification signals to the quasi-free η' photoproduction events. As expected, the fraction of in-medium signals decreases as the momentum increases. In this analysis, the amount of in-medium signals evaluated by the fit reaches 6% of quasi-free η' photoproduction events around 1 GeV/c and 13% in the momentum region of $300 \leq P_{\eta'} < 700$ MeV/c. On the other hand, the expected ratio of in-medium decays to overall η' photoproduction events is estimated to be less than 1% even in the momentum region of $300 \leq P_{\eta'} < 700$ MeV/c from the MC simulation based on the assumption of no change of the $\gamma\gamma$ decay widths in nuclear medium and vacuum, as described in Sec. 6.1.1. The unexpected increase of in-medium mass modification signals can be explained by adopting a model where the partial decay width of the $\eta' \rightarrow \gamma\gamma$, $\Gamma^{\gamma\gamma}$, is also modified in the nuclear medium. The partial decay width might possibly be modified by in-medium effects as well as the total decay width [46]. We

assume the simplest modification as follows: :

$$\Gamma^{\gamma\gamma}(\rho) = \Gamma_0^{\gamma\gamma} \left(1 + k_3 \frac{\rho}{\rho(0)} \right), \quad (6.8)$$

where $\Gamma_0^{\gamma\gamma} = 0.0043$ MeV [1] is the partial decay width of $\eta' \rightarrow \gamma\gamma$ in vacuum. The coefficient k_3 is an additional modification parameter. Figure 6.27 shows the k_3 dependence of χ^2 defined by

$$\chi^2 = \sum_{i=1}^5 \left(\frac{r_i^{\text{in}}(\text{real}) - r_i^{\text{in}}(\text{sim})}{\delta r_i^{\text{in}}} \right)^2, \quad (6.9)$$

where $r_i^{\text{in}}(\text{real})$, $r_i^{\text{in}}(\text{sim})$ are the ratio of the in-medium $\eta' \rightarrow \gamma\gamma$ decays to the quasi-free η' photoproduction events in the real data and a MC simulation for i -th momentum bin, respectively. δr_i^{in} is the experimental error of $r_i^{\text{in}}(\text{real})$. The amount of in-medium signals obtained in this analysis is reproduced if we adopt the additional modification parameter $k_3 = 63.2 \pm 15.6$, as shown in Figs. 6.26 and 6.27.

The result of the $\gamma\gamma$ invariant mass spectrum fit for the low-momentum sample of the carbon target data shows the 3.7σ enhancement of an additional component which can be expressed by simulated in-medium decays with mass reduction. This is not explained by any known background sources, discussed in Chapter 5. In addition, the additional component appears only in the low-momentum sample of the carbon target data. In contrast, the mass spectra were well reproduced by the fit only with the background functions for the other samples, namely the high-momentum sample of the carbon target data and the overall-momentum sample of the proton target data. Furthermore, the momentum dependence of the amount of in-medium signals can be reproduced by a MC simulation adopting a model where the partial decay width of $\eta' \rightarrow \gamma\gamma$ is also modified in the nuclear medium, as shown in Fig. 6.26. Although the statistics is not enough, these results indicate the possible existence of η' mass spectrum modification in the nuclear medium. We obtained the parameters corresponding to the mass reduction of $\Delta m_{\eta'} = 38\text{--}67$ MeV/ c^2 , and the width broadening of $\Delta\Gamma_{\text{tot}} < 60$ MeV at the nuclear saturation density.

These results can be compared with some theoretical expectations and other experimental studies. Modification of the η' mesons has been studied with various theoretical models. Nagahiro *et al.* have reported a calculation by using the NJL

model including the axial U(1) breaking [22]. They predicted a large mass reduction of $\Delta m_{\eta'} \sim 150 \text{ MeV}/c^2$ at the normal nuclear density. A prediction from the linear sigma model reported by Sakai *et al.* [25] shows a mass reduction of $\Delta m_{\eta'} \sim 80 \text{ MeV}/c^2$ at the normal nuclear density. Furthermore, a calculation using the quark-meson-coupling (QMC) model given by Bass *et al.* [27] suggested a mass reduction of $\Delta m_{\eta'} \sim 40\text{--}80 \text{ MeV}/c^2$ at the normal nuclear density.

The prediction from the QMC model and the linear sigma model does not largely conflict our results. Mass reduction by a few tens of MeV/c^2 at the normal nuclear density has been suggested by some experimental studies, although they are indirect indications. The η' -nucleus optical potential determined by the CBELSA/TAPS collaboration [30] corresponds a mass reduction of $\Delta m_{\eta'} \sim 40 \text{ MeV}/c^2$. The COSY-11 collaboration also reported that the result of the measurement of an $\eta'p$ scattering length did not contradict with the QMC model [47]. On the other hand, our results disfavor the large mass reduction predicted by the NJL model, i.e., $\Delta m_{\eta'} \sim 150 \text{ MeV}/c^2$, although the observed signal enhancement is statistically limited. Additionally, such a large mass reduction in nuclear media is disfavored by the experimental results in the missing-mass spectroscopy of the $^{12}\text{C}(p, d)$ reaction reported by the η -PRiME/Super-FRS collaboration, while their results relied on the theoretical calculation of formation cross sections for η' bound states [33]. Also, the LEPS2/BGOegg collaboration recently reported the analysis results of search for η' bound nuclei in the missing mass spectroscopy of the $^{12}\text{C}(\gamma, p)$ reaction with the tag of the $\eta'N \rightarrow \eta N$ process in a nucleus [34]. They excluded the deep η' -nucleus potential corresponding to the large mass reduction in order of $100 \text{ MeV}/c^2$ under the large branching fraction of the $\eta'N \rightarrow \eta N$ process. Our results are not inconsistent with the conclusions by these experiments. The experimental results generally disfavor the large mass reduction in order of $100 \text{ MeV}/c^2$. Theoretical models at present predict a wide range of mass reductions from $40\text{--}150 \text{ MeV}/c^2$, depending on their calculation methods or ambiguous parameters. Our results are consistent with relatively small mass reduction in those predictions. In addition, the width broadening of $\Delta\Gamma_{\text{tot}} < 60 \text{ MeV}$ in our analysis supports the experimental results given by the CBELSA/TAPS collaboration, which has suggested $\Delta\Gamma_{\text{tot}} \sim 15\text{--}25 \text{ MeV}$ at the normal nuclear density [48].

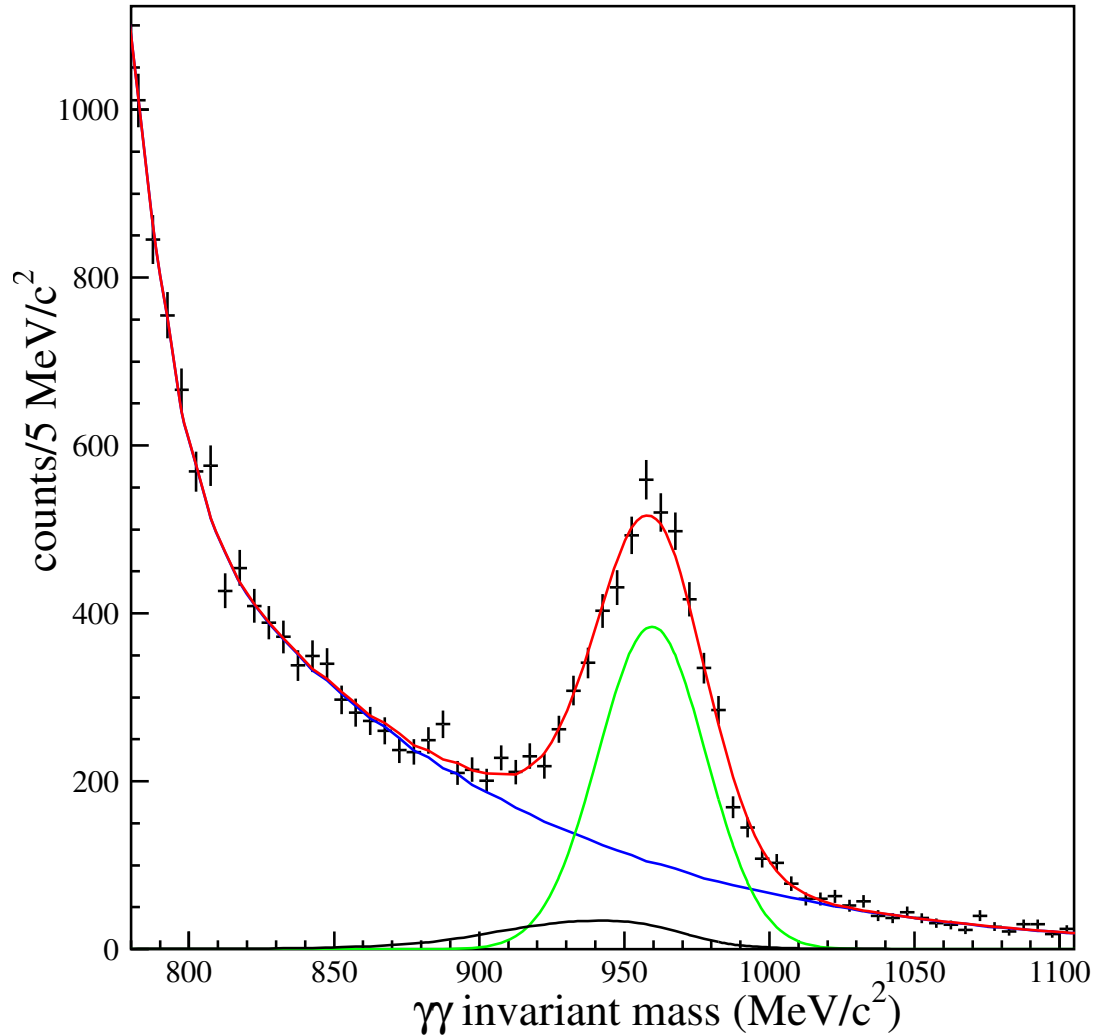


Figure 6.21: The $\gamma\gamma$ invariant mass spectrum in the momentum region of 300–700 MeV/c. The fit results are also overlaid. The green, blue, and black lines show the quasi-free η' peak, the sum of the smooth backgrounds and the ω background, and the signal function, respectively. The red line shows the sum of all components. $k_1 = 0.06$ and $k_2 = 125$ are taken as the modification parameters.

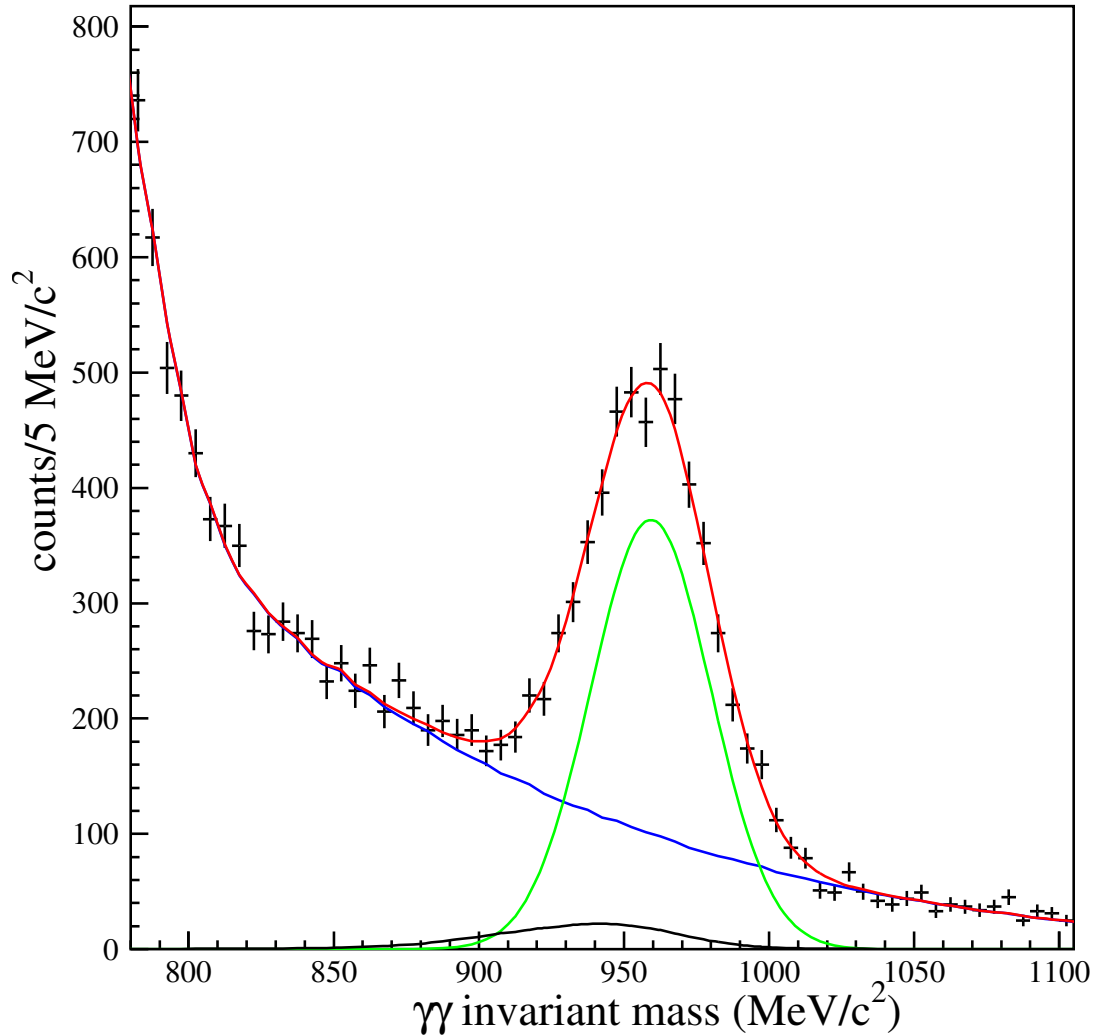


Figure 6.22: The $\gamma\gamma$ invariant mass spectrum in the momentum region of 700–900 MeV/c. The fit results are also overlaid. The green, blue, and black lines show the quasi-free η' peak, the sum of the smooth backgrounds and the ω background, and the signal function, respectively. The red line shows the sum of all components. $k_1 = 0.06$ and $k_2 = 125$ are taken as the modification parameters.

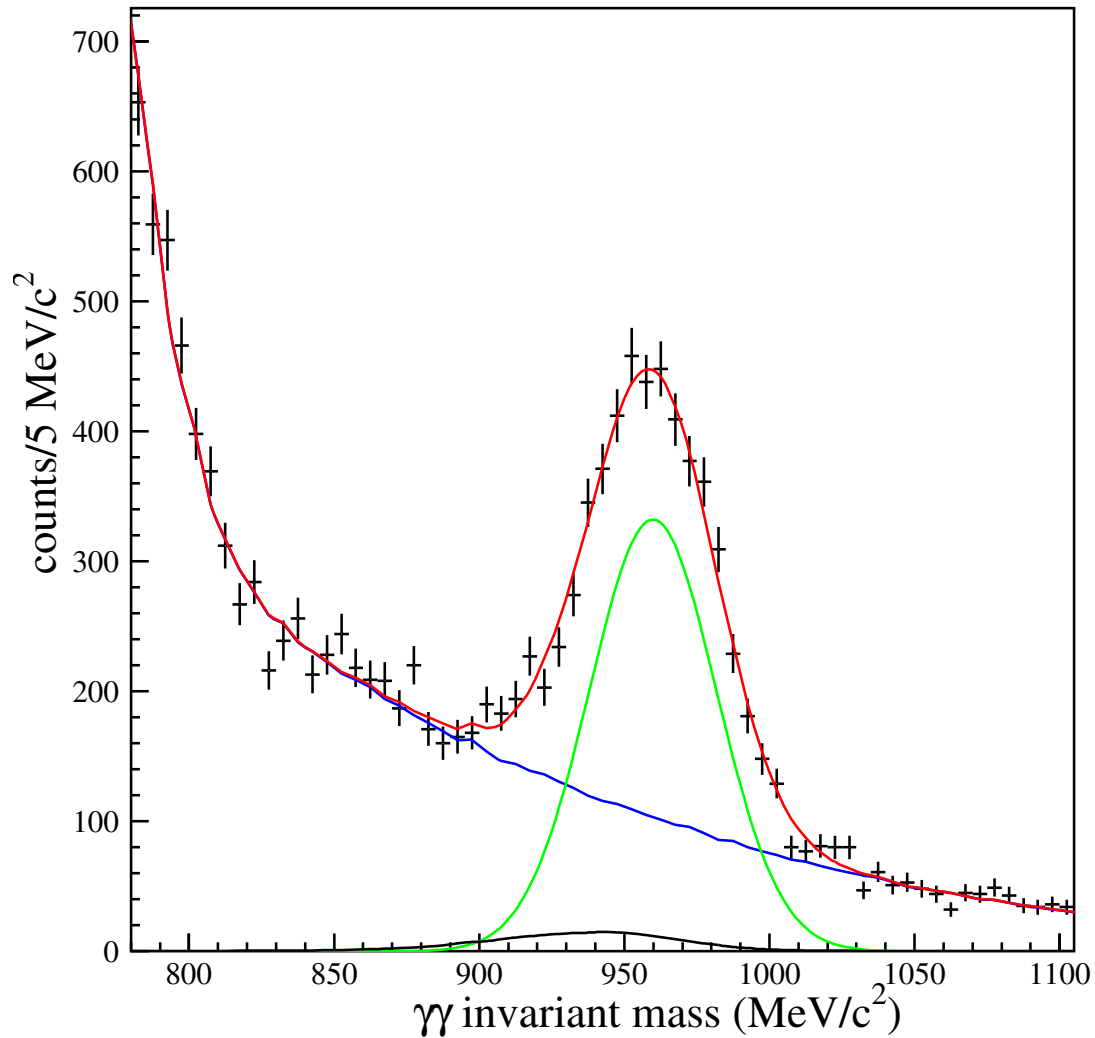


Figure 6.23: The $\gamma\gamma$ invariant mass spectrum in the momentum region of 900–1100 MeV/c. The fit results are also overlaid. The green, blue, and black lines show the quasi-free η' peak, the sum of the smooth backgrounds and the ω background, and the signal function, respectively. The red line shows the sum of all components. $k_1 = 0.06$ and $k_2 = 125$ are taken as the modification parameters.

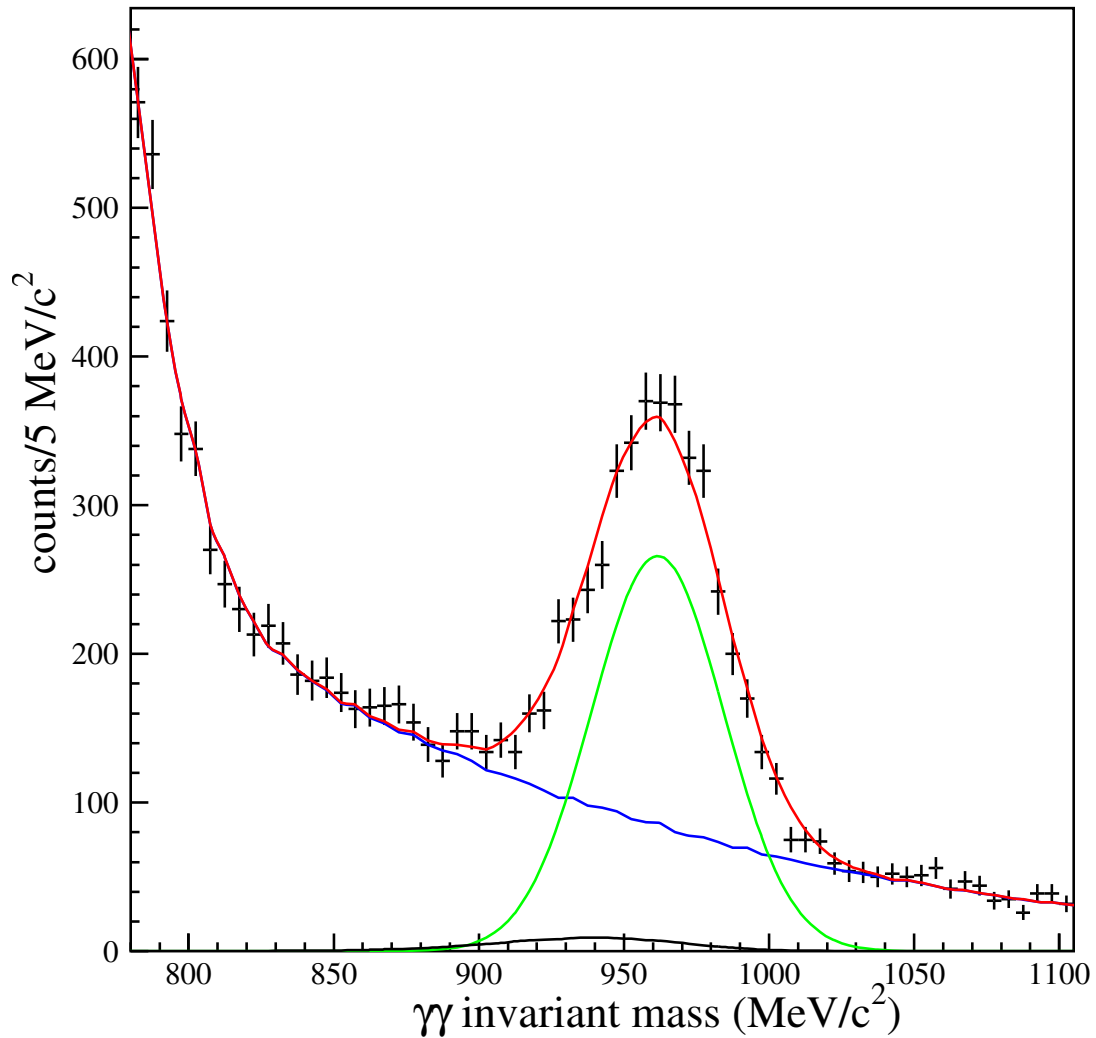


Figure 6.24: The $\gamma\gamma$ invariant mass spectrum in the momentum region of 1100–1300 MeV/c. The fit results are also overlaid. The green, blue, and black lines show the quasi-free η' peak, the sum of the smooth backgrounds and the ω background, and the signal function, respectively. The red line shows the sum of all components. $k_1 = 0.06$ and $k_2 = 125$ are taken as the modification parameters.

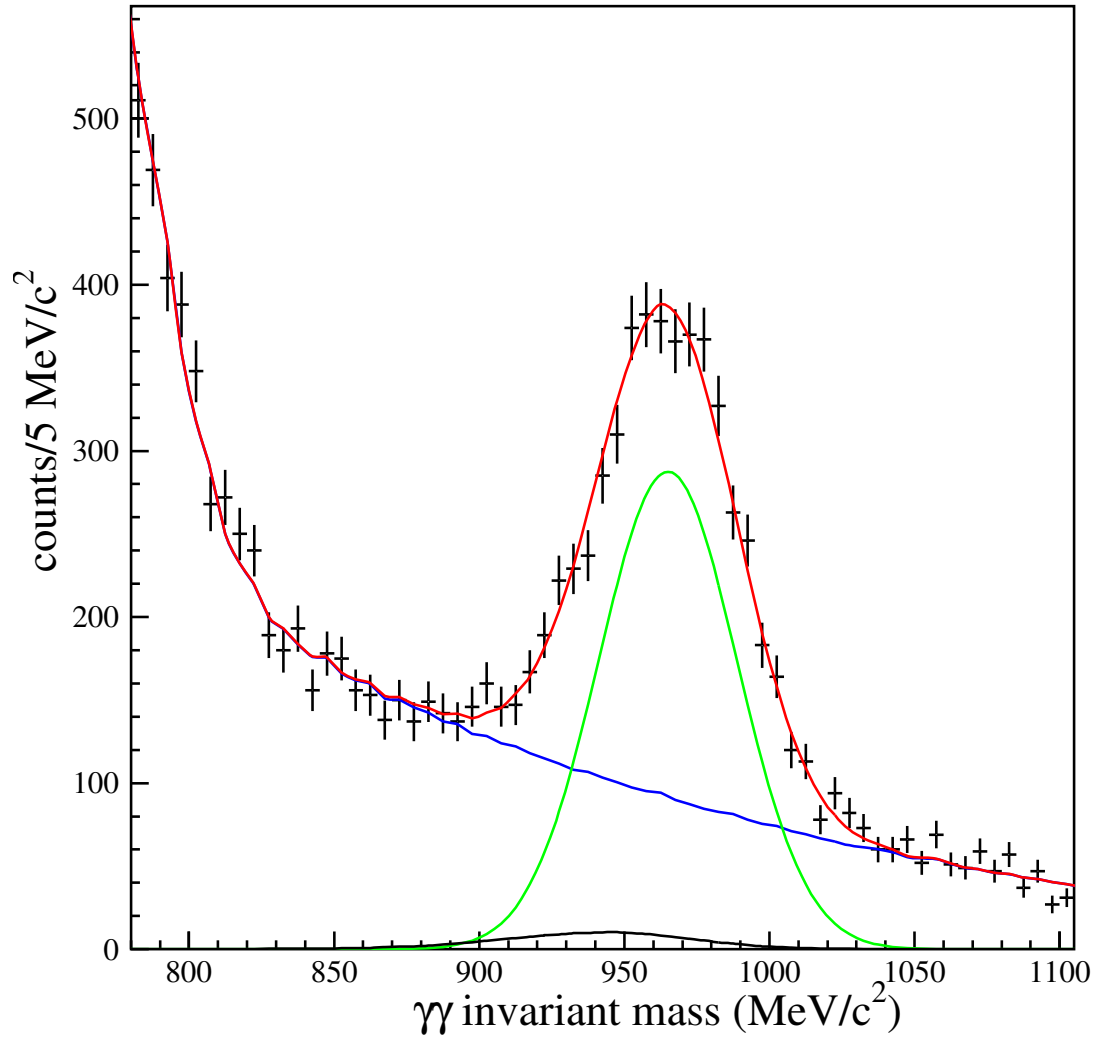


Figure 6.25: The $\gamma\gamma$ invariant mass spectrum in the momentum region of 1300–1700 MeV/c. The fit results are also overlaid. The green, blue, and black lines show the quasi-free η' peak, the sum of the smooth backgrounds and the ω background, and the signal function, respectively. The red line shows the sum of all components. $k_1 = 0.06$ and $k_2 = 125$ are taken as the modification parameters.

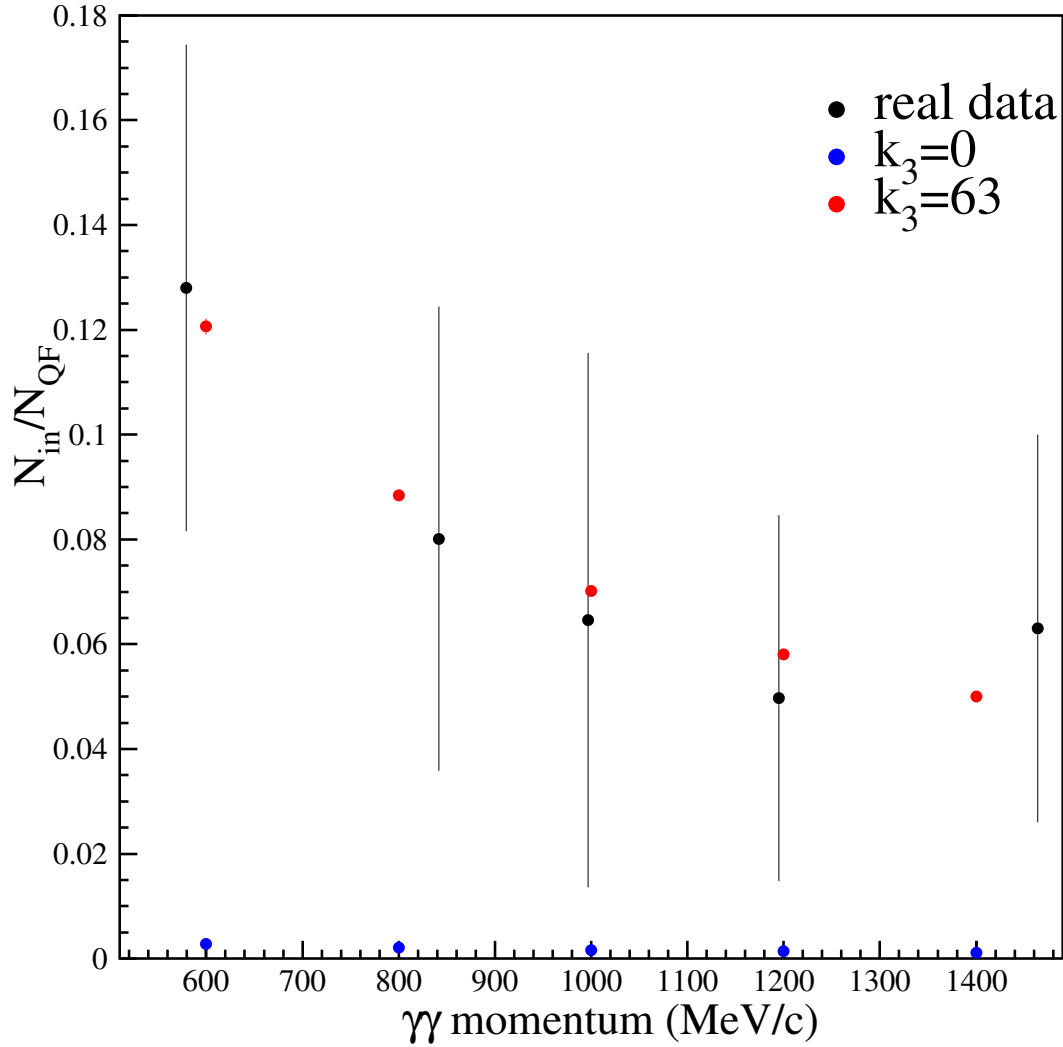


Figure 6.26: The ratios of the in-medium modification signals to the quasi-free η' photoproduction events in five regions of the $\gamma\gamma$ momentum. The black points come from the real data. The blue and red points show the ratios estimated by MC simulations with $k_3 = 0$ and $k_3 = 63$, respectively. $k_1 = 0.06$ and $k_2 = 125$ were used for the MC simulation.

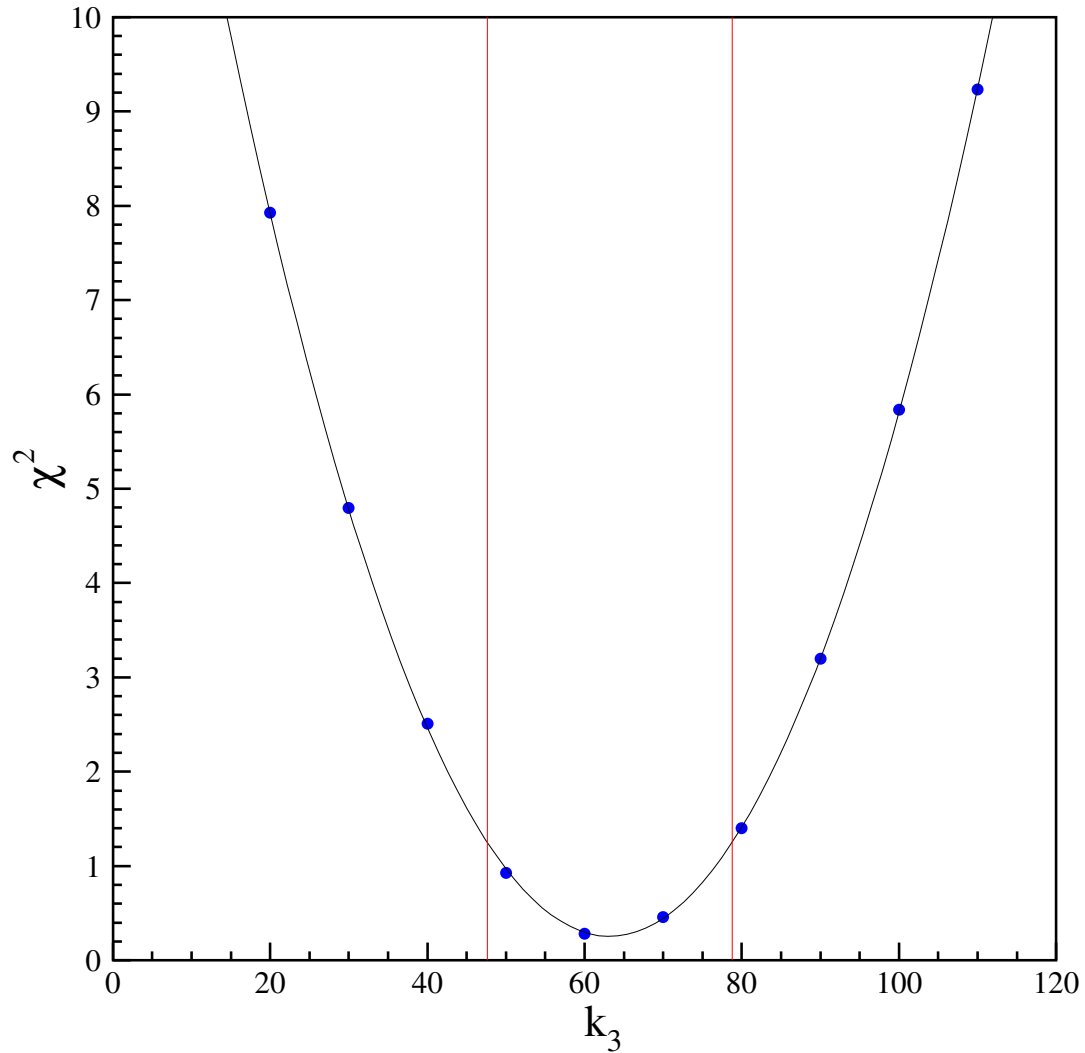


Figure 6.27: The k_3 dependence of χ^2 defined by Eq. 6.8. The dependence was fitted by a 2nd order polynomial function. The fit result is shown by a black line. The region within 1σ , where the χ^2 varies by 1 from the minimum value, is shown between red lines.

Chapter 7

Conclusions

The mass spectrum of η' mesons in nuclear medium was studied in a γ +C reaction via the $\eta' \rightarrow \gamma\gamma$ decay mode with the electro-magnetic calorimeter BGOegg. This is the first direct measurement of in-medium η' mass spectrum. The deviation of the $\gamma\gamma$ invariant mass distribution from the quasi-free η' mass spectrum was investigated by fitting realistic spectral functions to the measured spectra. An enhancement in the low-mass region of the η' mass was obtained with the statistical significance of over 3σ in the low-momentum sample ($P_{\eta'} \leq 1$ GeV/c) of the carbon target data.

The statistical significance of the enhancement was also evaluated from χ^2 differences of fits with and without modeled in-medium signal functions, varying two modification parameters representing the mass reduction and width broadening. The maximum significance of 3.7σ was obtained for the parameter corresponding to the mass reduction of $\Delta m_{\eta'} = 57$ MeV/c² in the low-momentum sample ($P_{\eta'} \leq 1$ GeV/c) of the carbon target data. In contrast, the mass spectra were well reproduced by the fit only with the background functions for reference samples: the high-momentum region ($P_{\eta'} > 1$ GeV/c) of the carbon target data, and the proton target data. In addition, the fraction of in-medium signals to quasi-free η' events increases as the $\gamma\gamma$ momentum decreases. The momentum dependence of the amount of in-medium signals was reproduced by a MC simulation adopting a model where the partial decay width of $\eta' \rightarrow \gamma\gamma$ is also modified in the nuclear medium. These results indicate the possible existence of η' mass spectrum modification in the nuclear medium. We ob-

tained the most favored area within 1σ for the parameters corresponding to the mass reduction of $\Delta m_{\eta'} = 38\text{--}67 \text{ MeV}/c^2$, and the width broadening of $\Delta\Gamma_{\text{tot}} < 60 \text{ MeV}$ at the nuclear saturation density.

These results were compared with some theoretical predictions and other experimental studies. Although some theoretical models predict a large mass reduction, our results disfavor the large mass reduction in order of $100 \text{ MeV}/c^2$, and limit the framework of theoretical models. Our results suggest a relatively small mass reduction which does not contradict the predictions from the QMC model [27] or the linear sigma model [25]. Also, our results does not conflict with the existing indirect measurements such as those by the CBELSA/TAPS collaboration [30] indicating a mass reduction by a few tens of MeV/c^2 .

Since the present analysis is statistically limited, we cannot exclude the possibility that the obtained enhancement is a statistical fluctuation. The analysis of additional data collected in another experimental period with the same experimental condition is on-going, and we will be able to double the statistics.

For the near future prospects, we are planning the experiments with additional detectors and the measurement with a heavier nuclear target, namely the copper target [53]. A new calorimeter consists of 252 PWO crystals and covers forward acceptance where BGOegg does not cover. This will reduce multi-meson background events due to escaping photons in the forward direction. The background in the $\gamma\gamma$ invariant mass distribution is expected to decrease by more than an order of magnitude in the η' mass region. The measurement with a heavier target provides more sensitivity because the fraction of η' decays inside a nucleus is expected to increase by its larger radius. We aim to achieve the sensitivity of in-medium signals even in the case of $k_3 = 1$ by the new experimental design.

Acknowledgements

I would like to express my sincere gratitude to my supervisor Prof. Hiroaki Ohnishi. He gave me a lot of advice and constructive suggestions for my work.

I would like to show my deepest appreciation to Prof. Hajime Shimizu. He led me to the field of hadron physics and has guided me diligently since I was a master course student. His ideas and suggestions have always helped me in my research.

I would like to express my great thanks to Prof. Norihito Muramatsu. He has taken care of me in the experiment and data analysis for a long time. He also proofread my doctoral thesis carefully. I could not complete my thesis without his extensive support.

I am grateful to Prof. Takatsugu Ishikawa, Prof. Manabu Miyabe, Prof. Atsushi Tokiyasu, Dr. Yusuke Tsuchikawa, and Dr. Yuki Honda for giving a lot of helpful advice and meaningful discussions. They have been a great help to me throughout my research life in Research Center for Electron Photon Science (ELPH), Tohoku University.

I would like to acknowledge to the members of LEPS2/BGOegg collaboration. We could successfully carry out the experiment thanks to the collaborators. I especially thank to Dr. Natsuki Tomida, Dr. Keigo Mizutani, Mr. Hirotomo Hamano, Mr. Toshikazu Hashimoto, Mr. Ryuji Yamazaki, Dr. Tran Hai Nam, and Mr. Takuya Shibukawa. They performed calibrations of detectors or some fundamental analysis in the LEPS2/BGOegg experiment. They also made the time I spent in SPring-8 more enjoyable.

I would like to express my special thanks to Mr. Ken'ichiro Shiraishi, Mr. Satoshi Kido, and Mr. Rintaro Shirai. I got a lot of inspiration from the discussions and collaborative work with them.

In the course of my research, I have been helped and supported by so many people that I can not mention here. I appreciate all of them.

Finally, I would like to express my deep gratitude to my parents and my beloved brother Kazuya for their supports and encouragements.

Appendix A

Examination of $\gamma\gamma$ spectra in other conditions

Some extra studies have been performed in order to check the robustness of our results. The results of the line shape analysis for $\eta' \rightarrow \gamma\gamma$ mass spectra in several specific conditions are described here. The function (6.4) were used for the fit. $k_1 = 0.06$ and $k_2 = 125$ were used for the signal function. The analysis conditions were the same as described in Chapter 4 except for the examined conditions described below.

First, samples with no charged cluster were examined. The condition that only two neutral clusters and no charged cluster were found at BGOegg were applied. Note that one or less charged cluster corresponding to a proton detection was allowed in the normal condition. In this condition, events with low recoil momenta of protons are enhanced though the statistics becomes lower. Figure A.1 shows the fitting results. The significance of the signals was unchanged from that in the normal condition.

Secondly, the mass spectra depending on the positions of clusters were checked. The samples were divided by following conditions:

- (i) Both two neutral clusters belong to the 4–21th layers.
- (ii) Either of two neutral clusters belongs to the 2–3th layers.

This conditions are applied in order to check that there is no difference in the mass

spectra between the events finding clusters at outer layers and inner layers. Figure A.2 and A.3 show the fitting results for the condition (i) and (ii), respectively.

Thirdly, the run dependence of the spectra was checked. The samples were divided into two parts: the first half of the period and the second half of the period. Figure A.4 and A.5 show the fitting results for the first half and the second half of the period, respectively.

Fourthly, the results of χ^2 difference test after applying the cut to exclude clusters with high leaked energies, described in Sec. 5.4.3, were checked. Figure A.6 shows the fitting results for the samples after applying the cut.

The χ^2 differences between the fits with and without a signal function and corresponding significance of in-medium signals are summarized in Table. A.1. The results of the normal condition, the case with no charged clusters, condition (i) and (ii) of the cluster position study, the individual part of the run dependence study, and the cut for the leaked energy are shown. For all the cases, significant χ^2 differences were obtained only for the low-momentum sample and the results are consistent with that with the normal condition. Note that the significance should apparently decrease as the statistics becomes low; namely, when the statistics becomes half, the significance should be reduced by $1/\sqrt{2}$.

Table A.1: χ^2 differences between the fits with and without a signal function and corresponding significance of in-medium signals obtained by analysis in individual conditions.

condition	low-momentum sample	high-momentum sample
normal condition	$\Delta\chi^2 = 14.1 (3.7\sigma)$	$\Delta\chi^2 = 1.0 (1.0\sigma)$
no charged cluster	$\Delta\chi^2 = 13.8 (3.7\sigma)$	$\Delta\chi^2 = 0.3 (0.6\sigma)$
condition (i)	$\Delta\chi^2 = 10.7 (3.3\sigma)$	$\Delta\chi^2 = 0.3 (0.5\sigma)$
condition (ii)	$\Delta\chi^2 = 7.8 (2.8\sigma)$	$\Delta\chi^2 = 0.8 (0.9\sigma)$
first half of the period	$\Delta\chi^2 = 7.9 (2.8\sigma)$	$\Delta\chi^2 = 0.5 (0.7\sigma)$
second half of the period	$\Delta\chi^2 = 6.9 (2.6\sigma)$	$\Delta\chi^2 = 0.8 (0.9\sigma)$
cut for leaked energy	$\Delta\chi^2 = 9.3 (3.1\sigma)$	$\Delta\chi^2 = 0.7 (0.8\sigma)$

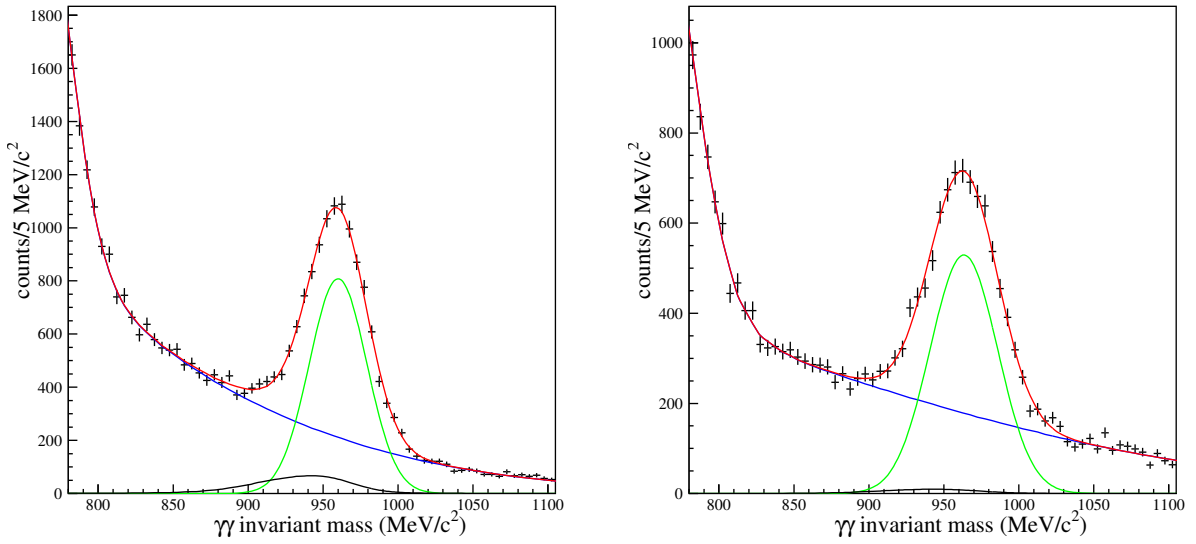


Figure A.1: The $\gamma\gamma$ invariant mass spectra for the events with no charged cluster. The left and right panels show the low-momentum and high-momentum samples, respectively. The green, blue, black, and red lines show the quasi-free η' peak, the sum of smooth backgrounds from multi-meson photoproduction etc. and ω photoproduction, the signal function, and the sum of all components, respectively. $k_1 = 0.06$ and $k_2 = 125$ were used for the signal function.

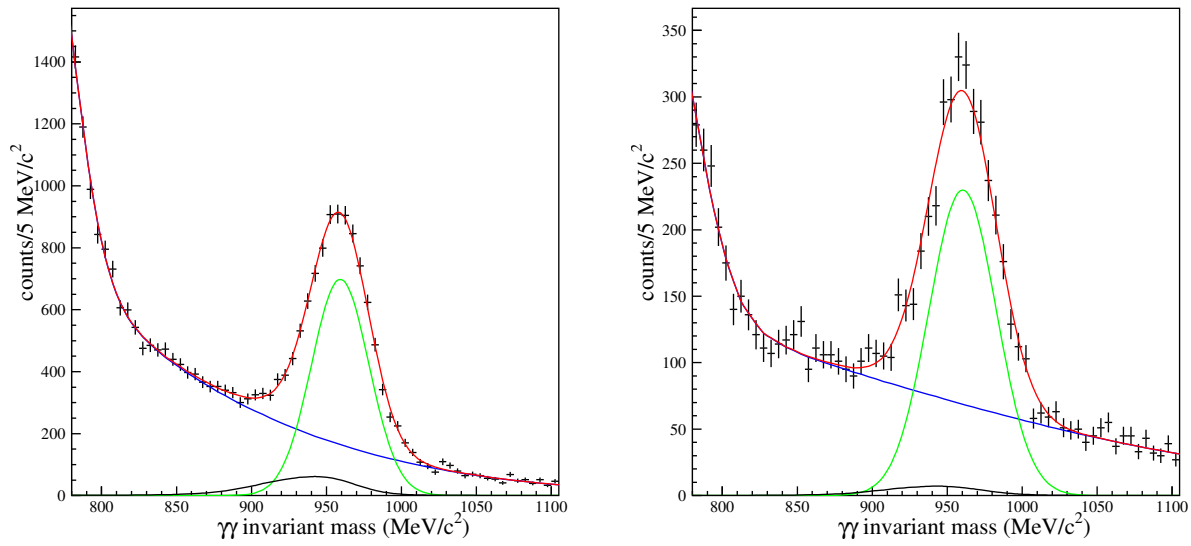


Figure A.2: The $\gamma\gamma$ invariant mass spectra for the samples of condition (i). The left and right panels show the low-momentum and high-momentum samples, respectively. The green, blue, black, and red lines show the quasi-free η' peak, the sum of smooth backgrounds from multi-meson photoproduction etc. and ω photoproduction, the signal function, and the sum of all components, respectively. $k_1 = 0.06$ and $k_2 = 125$ were used for the signal function.

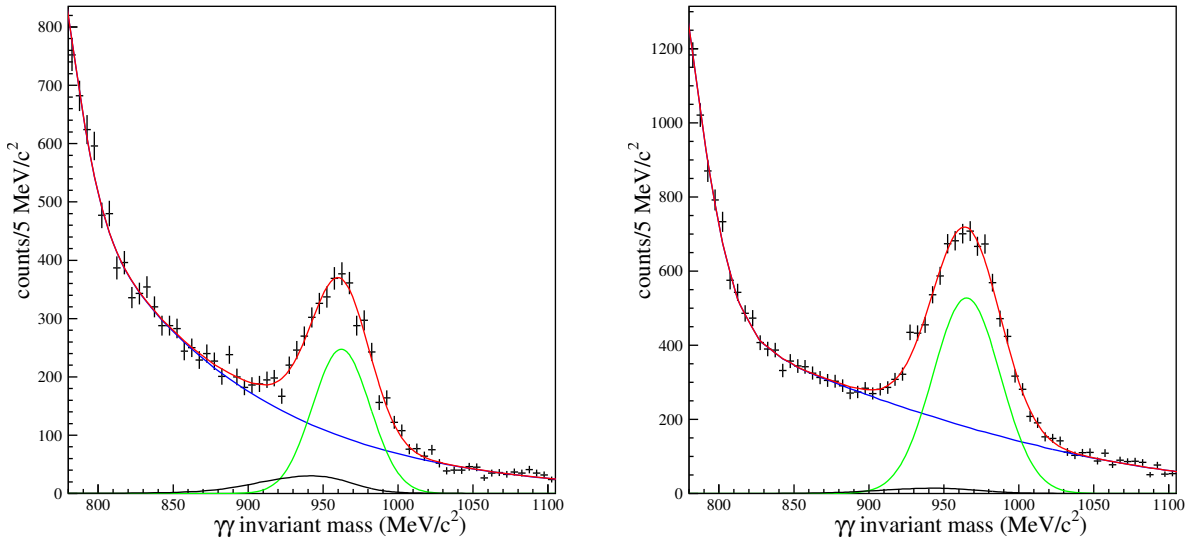


Figure A.3: The $\gamma\gamma$ invariant mass spectra for the samples of condition (ii). The left and right panels show the low-momentum and high-momentum samples, respectively. The green, blue, black, and red lines show the quasi-free η' peak, the sum of smooth backgrounds from multi-meson photoproduction etc. and ω photoproduction, the signal function, and the sum of all components, respectively. $k_1 = 0.06$ and $k_2 = 125$ were used for the signal function.

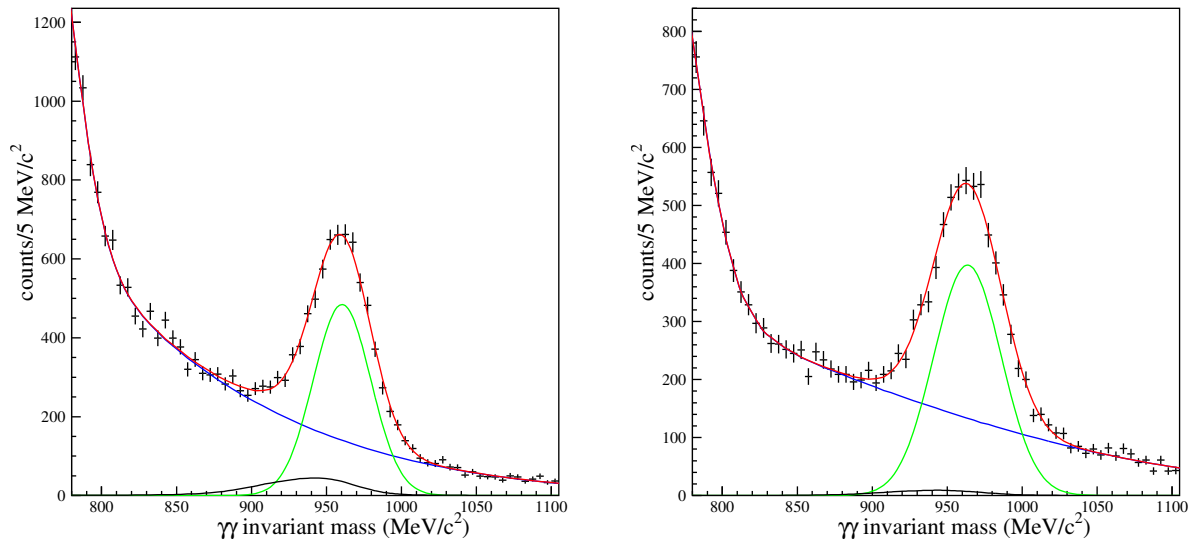


Figure A.4: The $\gamma\gamma$ invariant mass spectra for the samples of the first half of the period. The left and right panels show the low-momentum and high-momentum samples, respectively. The green, blue, black, and red lines show the quasi-free η' peak, the sum of smooth backgrounds from multi-meson photoproduction etc. and ω photoproduction, the signal function, and the sum of all components, respectively. $k_1 = 0.06$ and $k_2 = 125$ were used for the signal function.

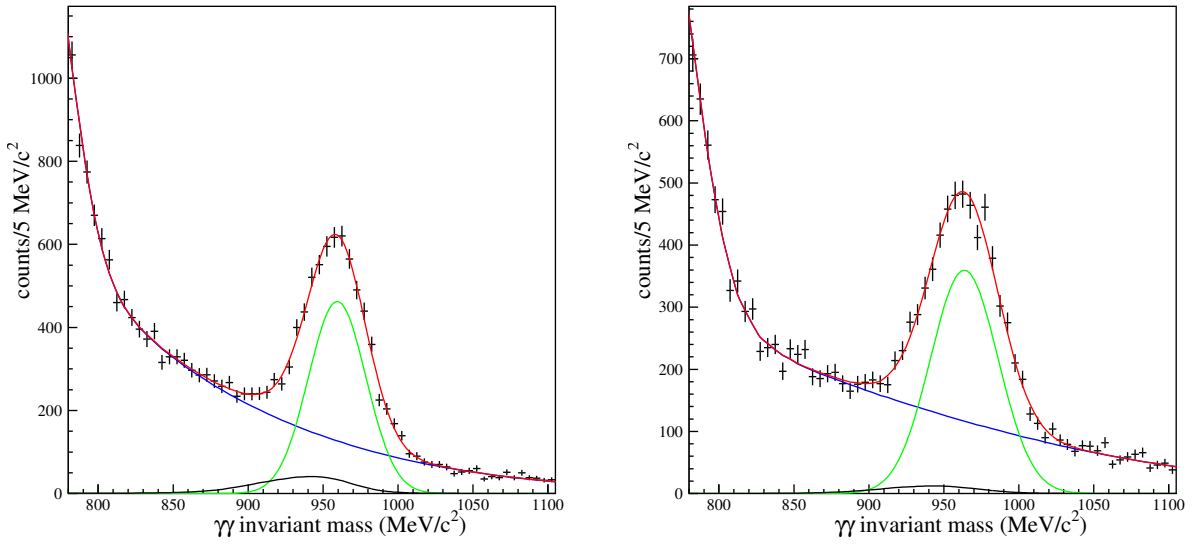


Figure A.5: The $\gamma\gamma$ invariant mass spectra for the samples of the second half of the period. The left and right panels show the low-momentum and high-momentum samples, respectively. The green, blue, black, and red lines show the quasi-free η' peak, the sum of smooth backgrounds from multi-meson photoproduction etc. and ω photoproduction, the signal function, and the sum of all components, respectively. $k_1 = 0.06$ and $k_2 = 125$ were used for the signal function.

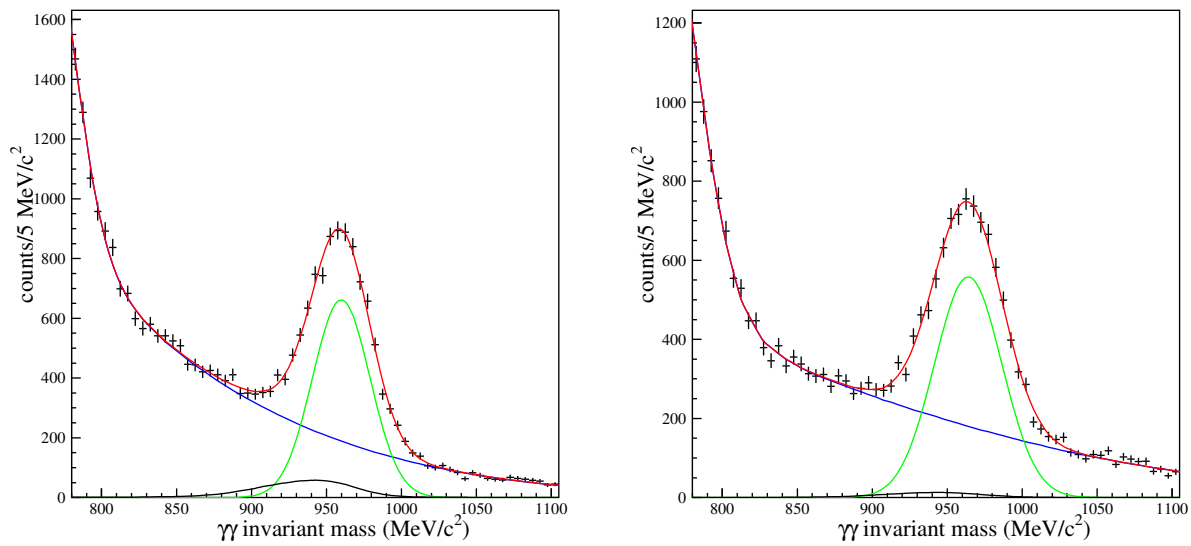


Figure A.6: The $\gamma\gamma$ invariant mass spectra for the samples after applying the cut excluding the high E_{leak} component. The left and right panels show the low-momentum and high-momentum samples, respectively. The green, blue, black, and red lines show the quasi-free η' peak, the sum of smooth backgrounds from multi-meson photoproduction etc. and ω photoproduction, the signal function, and the sum of all components, respectively. $k_1 = 0.06$ and $k_2 = 125$ were used for the signal function.

Appendix B

Mass resolution of π^0 and η

Figure B.1 shows the overall $\gamma\gamma$ invariant mass spectrum. In this figure, the number of clusters are not limited, and the distribution for all combination of two neutral clusters is shown. The mass resolution of $\pi^0 \rightarrow \gamma\gamma$ and $\eta \rightarrow \gamma\gamma$ events were evaluated by fitting a Gaussian and a 2nd-order polynomial function to the spectrum. The obtained values are $\sigma_\pi = 6.7 \text{ MeV}/c^2$ and $\sigma_\eta = 14.4 \text{ MeV}/c^2$ for $\pi^0 \rightarrow \gamma\gamma$ and $\eta \rightarrow \gamma\gamma$, respectively. Table B.1 shows the performance of several electro-magnetic calorimeters in the world used in the energy region of GeV [39, 49–52]. BGOegg achieves the world highest resolution of the π^0 and η mass comparing among these electro-magnetic calorimeters.

Table B.1: Performance of electro-magnetic calorimeters used in the energy of GeV [39, 49–52].

	BGOegg	Crystal Barrel	Crystal Ball	BGO-OD
scintillator	BGO	CsI(Tl)	NaI(Tl)	BGO
Energy resolution (1 GeV)	1.4%	2.5%	1.7%	3%
π^0 mass resolution (MeV/c^2)	6.7	9.9	10	14
η mass resolution (MeV/c^2)	14.4	16.6	22	24

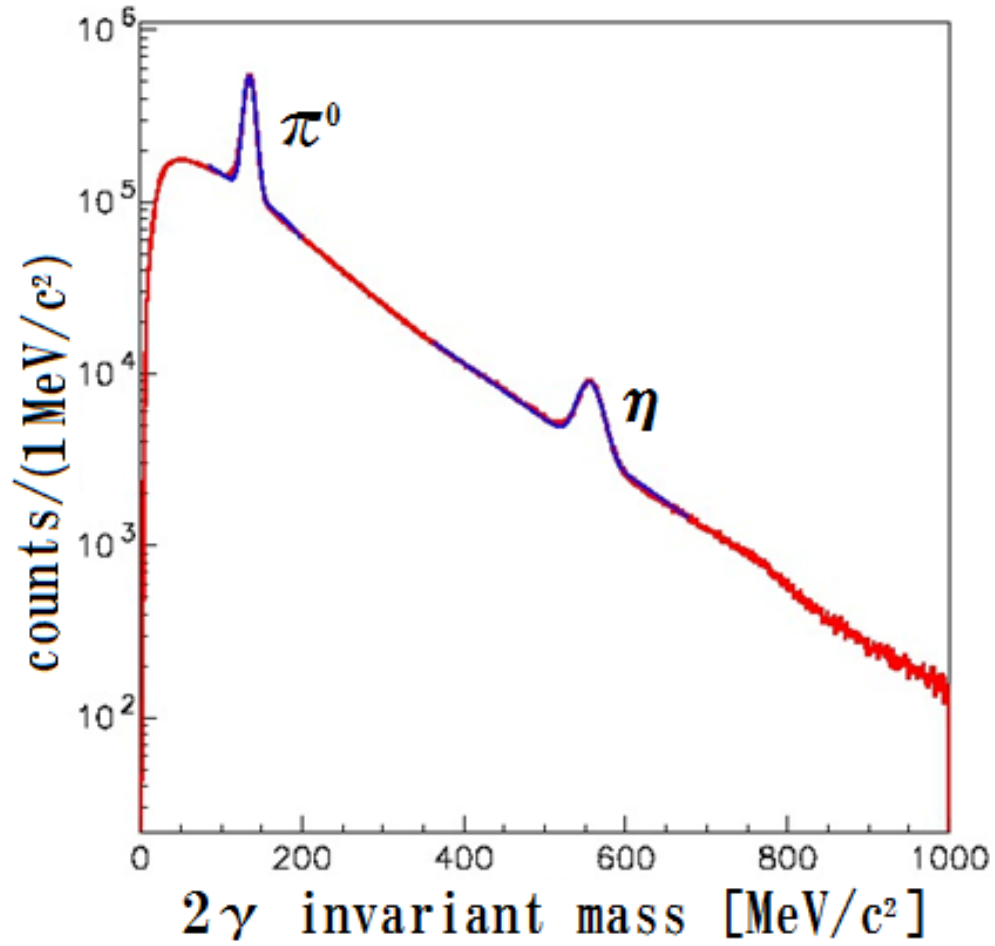


Figure B.1: Overall $\gamma\gamma$ invariant mass distribution. Fit results are shown by blue lines.

Bibliography

- [1] M. Tanabashi *et al.* (Particle Data Group), Phys. Rev. D **98**, 030001 (2018).
- [2] F. J. Gilman *et al.*, Phys. Rev. D **36**, 2761 (1987).
- [3] F. Ambrosino *et al.*, Phys. Lett. B **648**, 267 (2007).
- [4] H. Sazdjian, EPJ Web Conf **137**, 02001 (2017).
- [5] Y. Nambu, Phys. Rev. Lett. **4**, 380 (1960).
- [6] R. S. Hayano and T. Hatsuda, Rev. Mod. Phys. **82**, 2949 (2010).
- [7] Y. Nambu and G. Jona-Lasinio, Phys. Rev. **122**, 345 (1961).
- [8] M. Cheng *et al.*, Phys. Rev. D **77**, 014511 (2008).
- [9] T. Hatsuda and S. H. Lee, Phys. Rev. C **46**, R34 (1992).
- [10] D. Jido *et al.*, Phys. Lett. B **670**, 109 (2008).
- [11] K. Ozawa *et al.*, Phys. Rev. Lett. **86**, 5019 (2001).
- [12] G. M. Huber *et al.*, Phys. Rev. C **68**, 065202 (2003).
- [13] D. Trnka *et al.*, Phys. Rev. Lett. **94**, 192303 (2005).
- [14] M. Naruki *et al.*, Phys. Rev. Lett. **96**, 092301 (2006).
- [15] R. Muto *et al.*, Phys. Rev. Lett. **98**, 042501 (2007).
- [16] M. H. Wood *et al.*, Phys. Rev. C **78**, 015201 (2008).

- [17] M. Nanova *et al.*, Phys. Rev. C **82**, 035209 (2010).
- [18] M. Thiel *et al.*, Eur. Phys. J. A **49**, 132 (2013).
- [19] S. Weinberg, Phys. Rev. D **11**, 3583 (1975).
- [20] D. Jido *et al.*, Phys. Rev. C **85**, 032201 (2012).
- [21] Y. Nambu and G. Jona-Lasinio, Phys. Rev. **124**, 246 (1961).
- [22] H. Nagahiro *et al.*, Phys. Rev. C **74**, 045203 (2006).
- [23] M. Kobayashi and T. Maskawa, Prog. Theor. Phys. **44**, 1422 (1970).
- [24] M. Kobayashi *et al.*, Prog. Theor. Phys. **45**, 1955 (1971).
- [25] S. Sakai and D. Jido, Phys. Rev. C **88**, 064906 (2013).
- [26] J. Schechter and Y. Ueda, Phys. Rev. D **3**, 168 (1971).
- [27] S. Bass and A. Thomas, Phys. Lett. B **634**, 368 (2006).
- [28] K. Tsushima *et al.*, Phys. Lett. B **443**, 26 (1998).
- [29] H. Nagahiro *et al.*, Phys. Rev. Lett. **94**, 232503 (2005).
- [30] M. Nanova *et al.*, Phys. Lett. B **727**, 417 (2013).
- [31] H. Nagahiro *et al.*, Phys. Lett. B **709**, 87 (2012).
- [32] H. Nagahiro *et al.*, Phys. Rev. C **87**, 045201 (2013).
- [33] Y. K. Tanaka *et al.*, Phys. Rev. C **97**, 015202 (2018).
- [34] N. Tomida *et al.*, Phys. Rev. Lett. **124**, 202501 (2020).
- [35] G. E. Brown and M. Rho, Phys. Rev. Lett. **66**, 2720 (1991).
- [36] SPring-8 web site (<http://www.spring8.or.jp/>).
- [37] N. Muramatsu *et al.*, Nucl. Inst. Meth. in Phys. Res. A **737**, 184 (2014).
- [38] A. D'Angelo *et al.*, Nucl. Inst. Meth. in Phys. Res. A **455**, 1 (2000).

- [39] T. Ishikawa *et al.*, Nucl. Inst. Meth. in Phys. Res. A **837**, 109 (2016).
- [40] T. Ishikawa *et al.*, ELPH Annual Report 2011–2013, 175 (2014).
- [41] N. Muramatsu *et al.*, Phys. Rev. C **100**, 055202 (2019).
- [42] J. Allison *et al.*, IEEE Trans. Nucl. Sci., **53**, no. 1, 270 (2006).
- [43] S. Agostinelli *et al.*, Nuclear Instruments and Methods A, **506**, 250 (2003).
- [44] M. Williams *et al.*, Phys. Rev. C **80**, 045213 (2009).
- [45] M. Williams *et al.*, Phys. Rev. C **80**, 065208 (2009).
- [46] S. Goda *et al.*, Prog. Theor. Exp. Phys. **2014**, 033D03 (2014).
- [47] E. Czerwiński *et al.*, Phys. Rev. Lett. **113**, 062004 (2014).
- [48] M. Nanova *et al.*, Phys. Lett. B **710**, 600 (2012).
- [49] E. Aker *et al.*, Nucl. Inst. Meth. in Phys. Res. A **321**, 69 (1992).
- [50] D. Watts, 11th International Conference On Calorimetry In High Energy Physics (2004).
- [51] A. Thomas, HEPD Seminar (2010).
- [52] B. Bantes *et al.*, J. Phys.: Conf. Ser. **587**, 012042 (2015).
- [53] M. Miyabe, ELPH workshop C023 (2018).